

REPORT DOCUMENTATION PAGE		READ INSTRUCTIONS BEFORE COMPLETING FORM
1. REPORT NUMBER SIO REFERENCE 86-1	2. GOVT ACCESSION NO.	3. RECIPIENT'S CATALOG NUMBER
4. TITLE (and Subtitle) THE INTERNAL TIDE OFF SOUTHERN CALIFORNIA		5. TYPE OF REPORT & PERIOD COVERED Summary
		6. PERFORMING ORG. REPORT NUMBER MPL-U-34/85
7. AUTHOR(s) Robin George Williams		8. CONTRACT OR GRANT NUMBER(s) N00014-79-C-0472
9. PERFORMING ORGANIZATION NAME AND ADDRESS University of California, San Diego, Marine Physical Laboratory, Scripps Institution of Oceanography, San Diego, CA 92152		10. PROGRAM ELEMENT, PROJECT, TASK AREA & WORK UNIT NUMBERS
11. CONTROLLING OFFICE NAME AND ADDRESS Office of Naval Research, Department of the Navy 800 North Quincy Street, Arlington Virginia 22217		12. REPORT DATE January 1986
		13. NUMBER OF PAGES 162 pages
14. MONITORING AGENCY NAME & ADDRESS (if different from Controlling Office)		15. SECURITY CLASS. (of this report) UNCLASSIFIED
		15a. DECLASSIFICATION/DOWNGRADING SCHEDULE
16. DISTRIBUTION STATEMENT (of this Report) Document cleared for public release; distribution unlimited.		
17. DISTRIBUTION STATEMENT (of the abstract entered in Block 20, if different from Report)		
18. SUPPLEMENTARY NOTES		
19. KEY WORDS (Continue on reverse side if necessary and identify by block number) internal tide, semi-diurnal tidal harmonics, R/P FLIP.		
20. ABSTRACT (Continue on reverse side if necessary and identify by block number) The internal tide may well form an important link in the chain of events between the forcing of the surface tide and the eventual dissipation of internal waves by viscous forces. Two issues related to this chain of events are addressed. One is the directionality of the internal tide off the coast of California and the other is the widespread occurrence of semi-diurnal tidal harmonics in internal wave spectra. It is commonly accepted that the internal tide derives its energy from the forcing of isopycnal surfaces over topographic features by the		

surface tide. Accordingly, steep continental slopes like the Patton escarpment should be important generation regions. The directionality of the internal tide off California and hence the importance of the Patton escarpment as a source are assessed by analyzing data collected by the R/P FLIP. The results indicate that the direction of propagation of the internal tide is variable and that the majority of its energy does not appear to originate at the escarpment.

Strong peaks at the harmonics of the semi-diurnal frequency have been observed in many internal wave spectra. At issue is whether these harmonics are A) artifacts of the measurement technique, B) the signature of free waves present at those frequencies, or C) the manifestation of local non-linearity of the internal tide. Evidence suggests that A) is not an important effect. In an attempt to differentiate between B) and C) is bispectral analysis of a set of isopycnals was performed. The resulting incoherence (normalized bispectrum) values indicate that there is a significant degree of quadratic coupling between the internal tide and its harmonics. The observations of wave shape are consistent with Thorpe's theoretical model for the shape of finite amplitude internal waves in a continuously stratified fluid. However, the biphase values indicate that the shape of the internal tide is vertically asymmetric, unlike the symmetric shapes predicted by the model. The observed strong non-linearity of the internal tide indicates that it is possibly an important source for the internal wave continuum, contradicting a recent claim which is based on weak non-linear resonant interaction theory.



LIBRARY
RESEARCH REPORTS DIVISION
NAVAL POSTGRADUATE SCHOOL
MONTEREY, CALIFORNIA 93940

THE INTERNAL TIDE OFF SOUTHERN CALIFORNIA

Robin George Williams

Sponsored by the
Office of Naval Research
Contract N00014-79-C-0472

de SIO REFERENCE 86-1

January 1986

*Reproduction in whole or in part is permitted
for any purpose of the U.S. Government.*

Document cleared for public release;
distribution unlimited.

MPL-U-34/85

11
MARINE PHYSICAL LABORATORY
of the Scripps Institution of Oceanography.
de San Diego, California 92152

UNIVERSITY OF CALIFORNIA, SAN DIEGO
MARINE PHYSICAL LABORATORY OF THE
SCRIPPS INSTITUTION OF OCEANOGRAPHY
SAN DIEGO, CA 92152

THE INTERNAL TIDE OFF SOUTHERN CALIFORNIA

Robin George Williams

Sponsored by the
Office of Naval Resedarch
Department of the Navy
N00014-79-C-0472

SIO REFERENCE 86-1

January 1986

K. M. Watson, Director
Marine Physical Laboratory

MPL-U-34/85

TABLE OF CONTENTS

	Page
List of Figures and Tables.....	vii
Acknowledgements.....	x
Vita, Publication, Fields of Study.....	xi
Abstract.....	xii
1. Introduction.....	1
2. Description of Experiments, methods and data	
2.1 1980 Experiment.....	4
2.2 1983 Experiment.....	7
3. Directionality of the internal tide	
3.1 Introduction.....	14
3.2 Background.....	15
3.3 Model Predictions.....	19
3.4 Comparison with barotropic tide	26
3.5 Analysis of the Doppler data	33
3.6 Discussion.....	46
4. Internal Wave Spectral Harmonics:	
A comparison of measurement techniques	
4.1 Introduction.....	48
4.2 Observations of harmonics.....	48
4.3 Finestructure contamination	53
4.4 Spectral Analysis.....	62
4.5 Discussion.....	67
5. Free versus Forced Waves	
5.1 Introduction.....	68
5.2 Mechanisms.....	68
5.3 Bispectral Analysis.....	76
5.4 Data Analysis.....	82
5.5 Discussion.....	107
6. Summary.....	110
References.....	113

Appendices

A.	Calibration of 1980 CTD sensors	117
A.1	Vibroton Pressure Sensor (S/N 4173)	117
A.2	Temperature Sensors	120
A.3	Conductivity Sensors	120
B.	The SBE CTD system	125
C.	Digital correction methods for SBE conductivity and temperature data.....	136
D.	Bispectral analysis computational procedures.....	159
E.	FLIP's Doppler sonar system.....	162
F.	Principal axes of a vector field.....	165

LIST OF FIGURES AND TABLES

Figure		Page
Chapter 2		
2-1.	Cruise tracks for FLIP	5
2-2.	Schematic of FLIP (1980).....	6
2-3.	Sequence of temperature profiles	8
2-4.	Cruise tracks for MILDEX.....	9
2-5.	Schematic of FLIP (1983).....	11
2-6.	Sequence of σ_θ profiles	12
2-7.	Sequence of velocity profiles	13
Chapter 3		
3-1.	Internal tide beam of energy	16
3-2.	M_2 cotidal chart.....	18
3-3.	Co-tidal lines of the semi-diurnal tide	20
3-4.	Average Vaisala frequency profile.....	21
3-5.	Deep Vaisala frequency profile	22
3-6.	Internal tide characteristics	23
3-7.	Section of beam.....	25
3-8.	Barotropic tide and isopycnals.....	30
3-9.	Coherence and phase between barotropic tide and isopycnals	32
3-10.	Horizontal velocity components relative to FLIP	35
3-11.	FLIP's drift velocities.....	36
3-12.	Horizontal velocity components relative to Earth	38
3-13.	Horizontal velocity components at the tidal frequency.....	40
3-14.	R, P, and θ at 404 m	42
3-15.	Range average horizontal velocities	43
3-16.	R, P, and θ for the range average velocities	45
Table		
3-1.	Tidal constants for station 12.....	28
3-2.	Information about tidal constituents.....	29
Chapter 4		
4-1.	Spectrum of temperature fluctuations.....	49
4-2.	Spectra for MILE data.....	50
4-3.	Spectra for JASIN data	51
4-4.	Spectra for POLYMODE data	52
4-5.	Vertical velocity spectra.....	54
4-6.	Slant acceleration spectra	55
4-7.	Isotherms from 1980	59
4-8.	Time series of temperature at fixed depths in 1980	61
4-9.	Power spectra of vertical velocity (140-170 m).....	64
4-10.	Power spectra of vertical velocity (200-230 m).....	65
4-11.	Power spectra of vertical velocity (260-290 m).....	66

Chapter 5

5-1. Shapes of internal waves.....	69
5-2. Shapes of waves of the first mode in a tanh density profile.....	71
5-3. Shapes of waves of the first mode in a linear density profile.....	73
5-4. First mode vertical displacements in a shear flow.....	74
5-5a. Bicoherence for coupled waves.....	79
5-5b. Bicoherence for uncoupled waves.....	80
5-6. Average σ_θ profile for MILDEX.....	83
5-7. Isopycnal surfaces.....	84
5-8. Vertical displacement spectrum.....	85
5-9. Low pass filtered isopycnals.....	87
5-10. Amplitude of internal tide and ratios of the harmonics vs. depth.....	88
5-11. Vertical gradient of N^2	89
5-12. Shear profiles for MILDEX.....	90
5-13. Skewness for 1983 isopycnals.....	92
5-14. Skewness for 1980 isotherms.....	94
5-15. Low pass filtered 1980 isotherms.....	95
5-16. Color contoured band-pass filtered 1983 isopycnals.....	97
5-17. Spectrum, bispectrum and bicoherence at 80 m.....	99
5-18. Spectrum, bispectrum and bicoherence at 250 m.....	100
5-19. Bicoherence and biphase at (f_T, f_T) vs. depth.....	102
5-20. Bicoherence and biphase at $(2f_T, f_T)$ vs. depth.....	103
5-21. Isopycnal at 270 m.....	105
5-22. Average spectrum, bispectrum and bicoherence over 200-280 m.....	106

Appendix A

Figure

A-1. Calibration curve for pressure sensor.....	119
A-2. Calibration curve for upper temperature sensor.....	121
A-3. Calibration curve for lower temperature sensor.....	122
A-4. Calibration curve for upper conductivity cell.....	123

Table

A-1. Calibration constants for temperature and conductivity sensors.....	118
--	-----

Appendix B

B-1. CTD fish.....	126
B-2. Deck unit.....	127
B-3. SBE thermometer.....	128
B-4. SBE conductivity meter.....	129
B-5. Fall rate in May 1983.....	134
B-6. Fall rate during MILDEX.....	135

Table

B-1. Calibration constants for pressure transducer.....	130
B-2. Calibration constants for SBE thermometer.....	131
B-3. Calibration constants for SBE conductivity meter.....	132

Appendix C

Figure

C-1. A salinity profile from MILDEX showing spiking.....	137
C-2. Corrected salinity profile	138
C-3. Phase between downcast and upcast conductivity.....	140
C-4. Phase between downcast and upcast conductivity.....	141
C-5. Phase out to 0.32 cpm.....	142
C-6. Cubic fit to phase	143
C-7. Corrected phase	144
C-8. Spectrum of $\partial T/\partial z$	147
C-9. Spectrum of $\partial C/\partial z$	148
C-10. Phase between $\partial C/\partial z$ and $\partial T/\partial z$	149
C-11. Coherence between $\partial C/\partial z$ and $\partial T/\partial z$	150
C-12. Phase out to 1.35 cpm.....	151
C-13. Cubic fit to phase	152
C-14. Corrected phase	153
C-15. Ratio of amplitude responses.....	154
C-16. Normalized reciprocals of the ratio of amplitude responses	155
C-17. Cubic fit to Figure C-16.	156
C-18. Spectrum of $\partial T/\partial z$	157
C-19. Spectrum of $\partial C/\partial z$	158

Appendix D

D-1. Domain for bispectrum.....	160
---------------------------------	-----

Appendix E

E-1. Schematic of FLIP's Doppler sonar system hardware.....	163
---	-----

Appendix F

F-1. Principal axes of a vector field.....	169
--	-----

Table

F-1. Subroutine PRINA.....	168
----------------------------	-----

ACKNOWLEDGEMENTS

I wish to thank all the members of my committee. In particular, I wish to express gratitude to my adviser, Robert Pinkel, for all the guidance, encouragement and support he has given me.

I am indebted to the engineers of the Scripps internal waves group whose patience and dedication made possible the collection of such high quality data sets. They are Steve Beck, Mike Goldin, Lloyd Green, Larry Occhiello, Eric Slater, Lee Tamooka and Deena Voloshin. I should also like to thank FLIP's crew headed by Dewitt Efrd for their assistance during the cruises.

Special thanks go to Al Pluddemann, my fellow graduate student, for many stimulating discussions and ideas. In particular, I wish to acknowledge all the months of work he has put into pre-processing the sonar data.

Many thanks to Lloyd Regier for his suggestion to use principal axis analysis and to Steve Elgar, Robert Guza, and Ken Helland for their help with bispectral analysis.

Thanks also to Dimitri Alexandrou, Cimarron Boozer, Christian de Moustier, Frank Phelan, Jeff Sherman, Jerry Smith, Libe Washburn and Marco Weydert.

The task of typing this thesis was patiently performed by Eleanor Ford, Georgia Greaves and Lisa Stockinger. The figures were prepared by Jo Griffith.

Financial support was provided by the Office of Naval Research in the form of a research assistantship.

VITA

March 15, 1951 — Born — Ismailya, Egypt

1974 — B.A., University of York, York, England
1977 — M.A., University of California, San Diego
1979 — M.Sc., University College of North Wales, Bangor, Wales
1985 — Ph.D., Scripps Institution of Oceanography, University of California, San Diego

PUBLICATION

R. G. Williams, J. Darbyshire and P. Holmes. "Wave refraction and diffraction in a caustic region: a numerical solution and experimental validation." Proc. Instn. Civ. Engrs., Vol. 69, Part 2, pp. 635-649, 1980.

FIELDS OF STUDY

Major Field: Oceanography

Studies in Wave Dynamics

Professors Myrl C. Hendershott, Russ E. Davis, Walter H. Munk,
and Robert Pinkel

Studies in Physical Oceanography

Professors Joseph L. Reid, Myrl C. Hendershott, and Walter H. Munk

Studies in Fluid Mechanics

Professors Clinton D. Winant, David Miller, and Carl H. Gibson

Studies in Digital Signal Processing

Professor William S. Hodgkiss, Jr.

ABSTRACT OF THE DISSERTATION

The Internal Tide off Southern California

by

Robin George Williams

Doctor of Philosophy in Oceanography

University of California, San Diego, 1985

Professor Robert Pinkel, Chairman

The internal tide may well form an important link in the chain of events between the forcing of the surface tide and the eventual dissipation of internal waves by viscous forces. Two issues related to this chain of events are addressed. One is the directionality of the internal tide off the coast of California and the other is the widespread occurrence of semi-diurnal tidal harmonics in internal wave spectra.

It is commonly accepted that the internal tide derives its energy from the forcing of isopycnal surfaces over topographic features by the surface tide. Accordingly, steep continental slopes like the Patton escarpment should be important generation regions. The directionality of the internal tide off California and hence the importance of the Patton escarpment as a source are assessed by analyzing data collected by the R/P FLIP. The results indicate that the direction of propagation of the internal tide is variable and that the majority of its energy does not appear to originate at the escarpment.

Strong peaks at the harmonics of the semi-diurnal frequency have been

observed in many internal wave spectra. At issue is whether these harmonics are A) artifacts of the measurement technique, B) the signature of free waves present at those frequencies, or C) the manifestation of *local* non-linearity of the internal tide. Evidence suggests that A) is not an important effect. In an attempt to differentiate between B) and C) a bispectral analysis of a set of isopycnals was performed. The resulting bicoherence (normalized bispectrum) values indicate that there is a significant degree of quadratic coupling between the internal tide and its harmonics. The observations of wave shape are consistent with Thorpe's theoretical model for the shape of finite amplitude internal waves in a continuously stratified fluid. However, the biphase values indicate that the shape of the internal tide is vertically asymmetric, unlike the symmetric shapes predicted by the model. The observed strong non-linearity of the internal tide indicates that it is possibly an important source for the internal wave continuum, contradicting a recent claim which is based on weak non-linear resonant interaction theory.

CHAPTER 1

INTRODUCTION

The majority of the energy present in the oceanic internal wave-field has been shown to reside in bands centered at the near-inertial and tidal frequencies, but the problem of how this energy is re-distributed to different space and time scales in the ocean is still largely unknown. The internal tide is thought to play an important role in this complicated dynamical balance. It can act both as a source of energy (for the smaller scale motions) and as a sink of energy (for the surface tide). The work described in this thesis addresses issues related to the chain of events between production and dissipation of the internal tide in the deep ocean off the coast of California. In particular the directionality and non-linearity of the internal tide are estimated using data collected by R/P FLIP.

The observations were made during two cruises, which took place in April-May 1980 and October-November 1983. The second experiment was part of a larger venture called MILDEX (Mixed Layer Dynamics Experiment), which involved two other research vessels, the R/V ACANIA and the R/V WECOMA. During both experiments thousands of CTD and Doppler sonar velocity profiles were recorded. In 1980 CTD information was collected from the surface down to 400 m and in 1983 from the surface down to 310 m. In both experiments Doppler sonar current velocity profiles were obtained. For 1980 the depth range for these profiles was 100-700 m and, for 1983, 100-1100 m. Time series of vertical displacement, vertical velocity and horizontal velocity were constructed from these data. These profiles and time series form the basic data set upon which this thesis is based.

Chapter 2 describes the experiments, the instrumentation and methods used to collect the data. Appendices A, B, and C expand on topics mentioned in Chapter 2.

Appendix A gives an account of the calibration of the "homemade" CTD sensors used in the 1980 experiment. Appendix B gives a brief description of the Sea Bird Electronics (SBE) CTD system used during MILDEX. Appendix C describes the digital correction methods used to improve the quality of the temperature and conductivity data collected by the SBE system.

In Chapter 3 the issue of the directionality of the internal tide is addressed. A substantial amount of work has been published by investigators who have studied this problem off the east coast of the U.S.A. In that area, the Blake escarpment has been observed to be an important generator with the internal tide propagating away from the escarpment to the east (Hendry, 1977). These observations are consistent with theoretical models (e.g. Rattray, 1960) which show how continental slopes can be major source regions for the internal tide. These linear models predict that the internal tide should propagate away from the slope into the ocean interior as a beam of energy bounded by characteristics. Some observations of the internal tide in deep waters close to continental slopes show evidence for this beamlike behavior (Regal and Wunsch, 1973, Dewitt et al, 1985).

Very little descriptive work of the internal tide off California has been reported in the literature. However, two notable exceptions are Summers and Emery (1963) and Krauss (1966) which both describe observations in this region. In these papers evidence is presented which shows that the internal tide is propagating to the north-east toward the continental shelf, the opposite of what one expects. Since FLIP's downward looking sonars measure orthogonal components of slant velocity, I was able to estimate parameters relevant to the directionality of the internal tide. FLIP's observations of the internal tide are also compared to predictions of the surface tide at a station close to the Patton escarpment. From these two sets of information, the importance of the escarpment as a source region for the internal tide is

assessed.

In chapter 4 an account is given of the widespread occurrence of semi-diurnal tidal harmonics in internal wave spectra. Spectral harmonics are of interest because they might be the manifestation of non-linearity in the wave-field. Alternatively, they could be an artifact of the measurement technique. In the case of fixed depth measurements, finestructure contamination is known to cause spurious non-linearities and hence spectral harmonics. FLIP's repeated profiling information can be analyzed in a variety of ways each of which responds differently to potential sources of non-linearity. This type of analysis was performed on the 1980 temperature profiles and the results are presented.

In chapter 5 work is described which attempts to determine whether the harmonics observed in spectra of FLIP data are due to free or *locally* forced waves. These data consist of the 1980 isotherms and the 1983 isopycnals. These do not suffer from the finestructure contamination effects discussed in chapter 4. Of the two types of time series, isopycnals are preferred because they are a more faithful representation of the internal wave-field: they do not suffer from the spurious effects of lateral intrusions. Accordingly, the 1983 isopycnals were chosen for a bispectral analysis, a technique which can differentiate between free and forced waves. The results are presented and interpreted in the light of theoretical models for nonlinear progressive internal waves.

In Chapter 6 the conclusions of the thesis are summarized.

Appendix D describes the technique of bispectral analysis and the related computational procedures. Appendix E contains a brief description of FLIP's Doppler sonar system. Appendix F describes the method to determine the principal axes of a vector field which is used in the analysis described in Chapter 3.

CHAPTER 2

DESCRIPTION OF EXPERIMENTS, INSTRUMENTS, METHODS AND DATA

2.1 1980 Experiment

On 25 April 1980 R/P FLIP departed San Diego for a station at 31°N , 124°W , approximately 400 km offshore. From this position, FLIP drifted slowly south for thirty days along the track shown in Figure 2-1. The onboard instrumentation (Fig. 2-2) included a profiling array of current meters developed by R. Weller of Woods Hole Oceanographic Institution (Weller, 1981), which profiled from 5 to 150 m every hour and a profiling CTD system (Pinkel, 1975). In addition, four Doppler sonars mounted on FLIP's hull profiled 1100 m horizontally and 700 m vertically. Two large (1.6 m diameter) sonars, operating at 80 and 85 kHz, were mounted at a depth of 85 m, at right angles azimuthally. Two smaller (1.5×0.75 m) sonars were mounted at a depth of 38 m, angled 45° downward, and operated at 70 and 75 kHz.

Data were collected with the CTD sensors during the period 5-22 May 1980. The CTD system used was constructed at Scripps Institution of Oceanography expressly for the purpose of rapid profiling (Occhiello and Pinkel, 1976). It consisted of two sensor packages. A conductivity and a temperature sensor were suspended just below the sea surface, when the profiler was at the top of its cycle, with a second package containing conductivity, temperature and pressure sensors suspended 183 m below. The sensors were cycled approximately 220 m vertically every 130 seconds. A continuous profile down to 400 m was produced, with a region between 183 and 200 m where the upper and lower sensors overlapped. This enabled the cross calibration of the conductivity and temperature instruments. The fall speed of the system was approximately 4 m/sec. Data were recorded at a 5 Hz sample rate on the descent

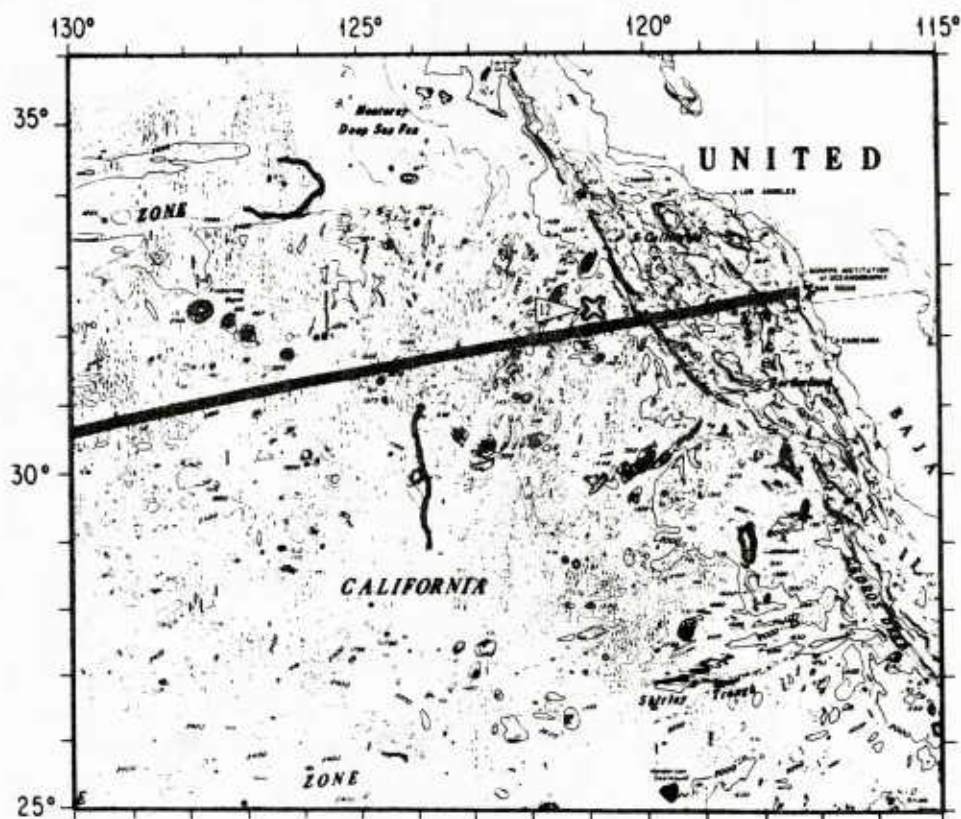


figure 2-1 Cruise tracks for R/P FLIP during the 1980 and 1983 experiments. The strong dark line indicates a cross-section which has been surveyed in detail. Station 12 is marked with a cross.

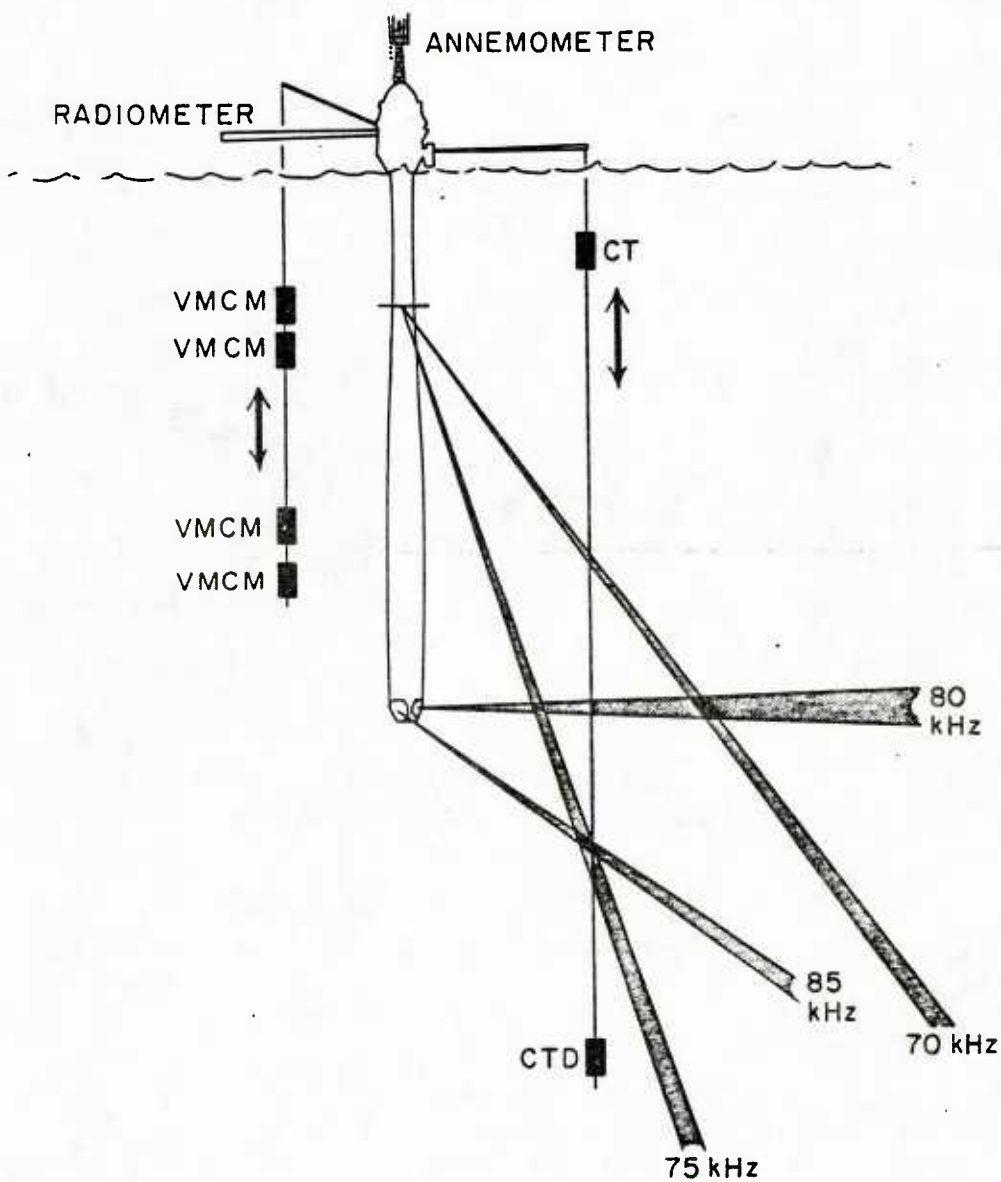


figure 2-2 Schematic diagram of 1980 FLIP experiment. Sonar and profiling CTD location are indicated. Temperature profiles are obtained to a depth of 400 m every 130 sec. The profiling current meter (VMCM) array was developed and operated by R. Weller of WHOI.

portion of the profile.

A description of the calibration of the CTD sensors is given in appendix A. Due to problems experienced with the conductivity sensors (described in appendix A), only temperature and depth information were processed further. A total of 11,483 temperature profiles were recorded. Fig. 2-3 shows 200 of these profiles covering a period of 24 hours. The slightly darker tint around 200 m is due to the overlapping of the two sensor packages. The most energetic motion is the internal tide which is clearly discernible from the advection of the fine structure.

A full description of the sonar data and analysis can be found in Pinkel (1983).

2.2 1983 Experiment

FLIP arrived on station at 34° N, 127° W on 22 October. From this position FLIP drifted for the next 24 days along the track shown in Fig. 2-1.

The experiments conducted from onboard FLIP during this time were part of a larger venture called MILDEX (Mixed Layer Dynamics Experiment) in which both the R/V WECOMA from Oregon State University and the R/V ACANIA from the Naval Postgraduate School, took part. In addition, a drifting thermister chain attached to a surface buoy was deployed by Oregon State University (OSU). For a more complete description of MILDEX, see the MILDEX second planning document (1983). Fig. 2-4 shows the tracks of FLIP, the WECOMA and the drifting buoy. During the period October 24 - November 5 the ACANIA steamed continuously in 5 km sided squares around FLIP collecting CTD and current profiles.

The onboard instrumentation consisted of: a Sea-Bird Electronics (SBE) CTD system, two horizontal looking sonars, four downward looking sonars in the JANUS configuration, four sets of VMCM's, two wave staffs, meteorological instruments and

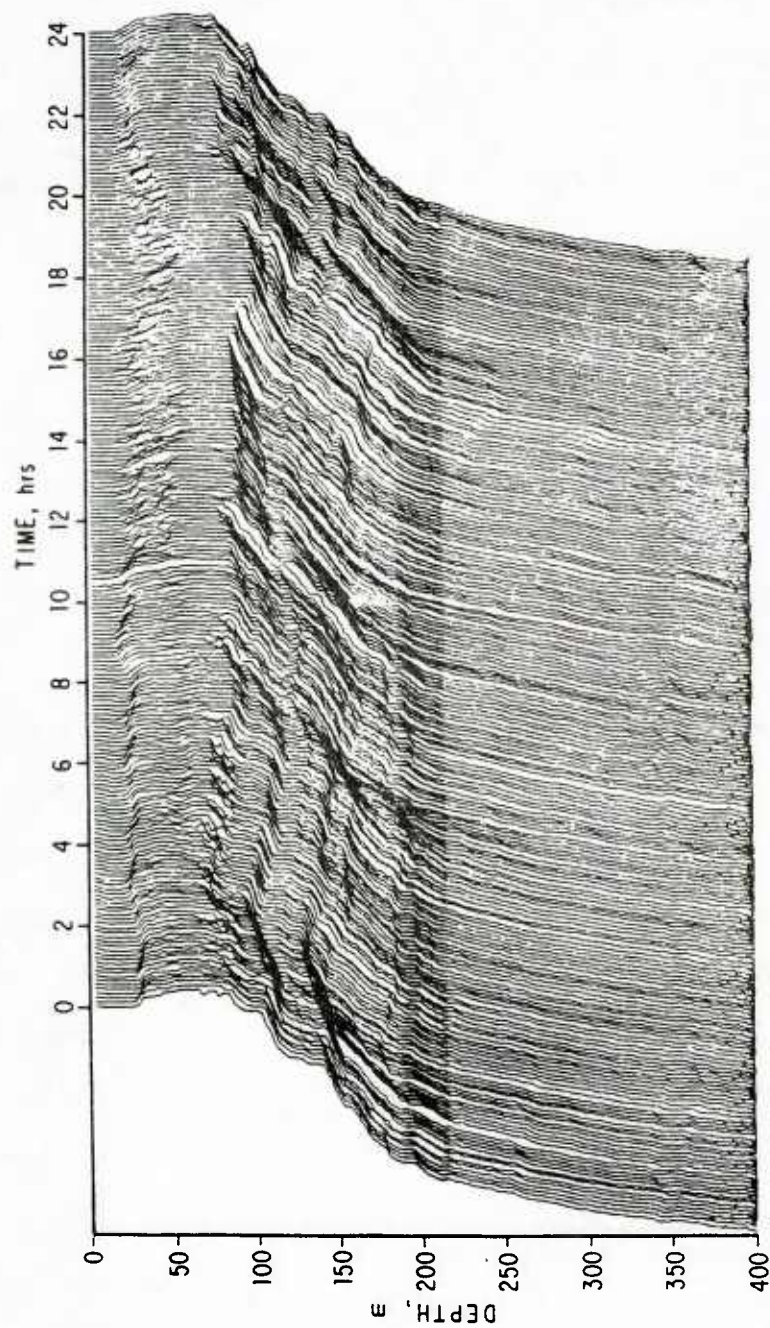


figure 2-3 A sequence of 220 temperature profiles taken during the period noon 19 May 1980 to noon 20 May 1980. Note the cool, fresh surface layer overlying a deeper warmer isothermal region.

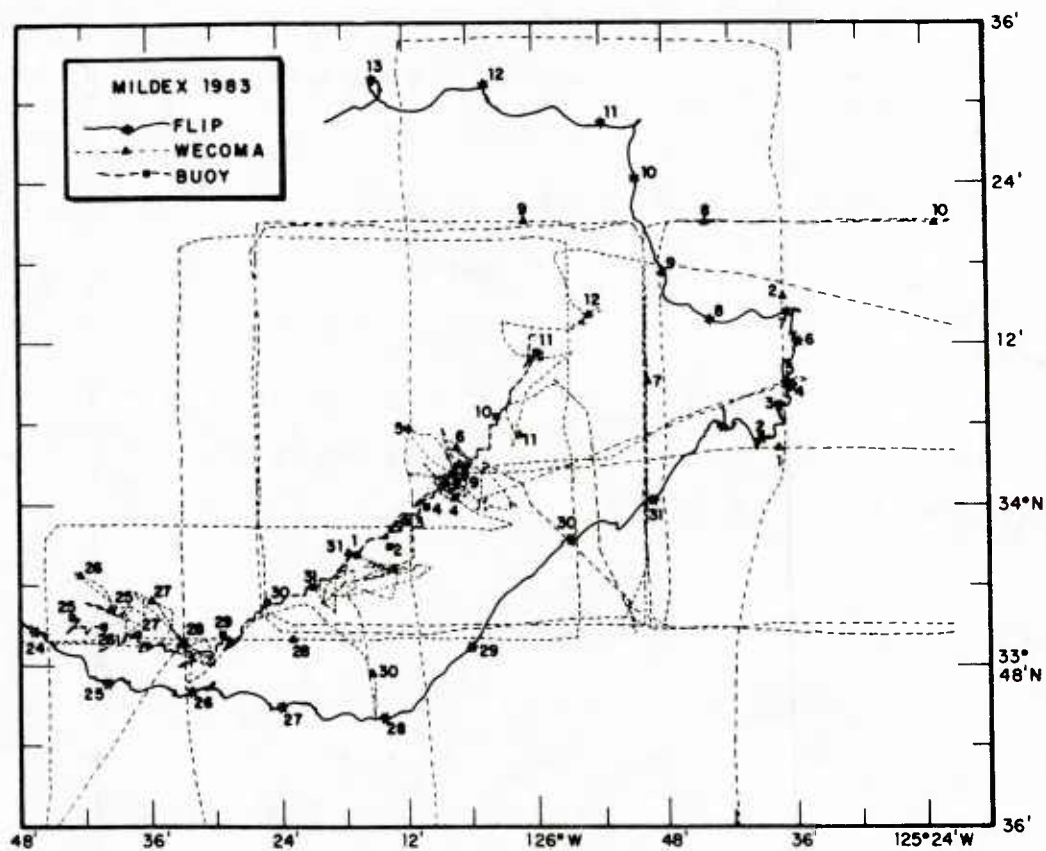


figure 2-4 The tracks of the R/V WECOMA, R/P FLIP and the drifting thermistor chain during MILDEX, 1983. This plot is adapted from the original supplied by R. Weller of WHOI.

radiometers (see Fig. 2-5).

CTD data were collected from 29 October until 13 November. The mode of operation was similar to that used for the 1980 experiment, with four differences. First, there was one instrument package which contained all three of the CTD sensors. Second, the package was cycled down to approximately 310 m not 400 m. Third, the cycling period was 3 minutes not 2 minutes 10 seconds, and fourth, the sampling rate was 12 Hz not 5 Hz. For a more complete description of the SBE CTD system see Appendix B. A total of 6710 CTD profiles were recorded from which profiles of σ_θ were calculated. A subset of these profiles corresponding to a 24 hour time period is shown in Fig. 2-6.

Sonar data were collected from 27 October - 15 November. The panels were operated in 67-80 kHz range, with the downward looking sonars smaller ($0.4 \text{ m} \times 1.2 \text{ m}$) than the horizontal looking sonars ($1.6 \text{ m} \times 0.8 \text{ m}$). All the panels were mounted at the same depth, 38 m, with the smaller sonars angled 52.5° downward from the horizontal. These had a range of approximately 1400 m. For further details of the system see Appendix E. A typical set of velocity profiles obtained from a downward looking sonar is shown in Fig. 2-7. These profiles are three minute averages and have a range resolution of 11 m. The noisier velocity values apparent beyond 1000 m are due to decreased signal to noise ratios at these far ranges.

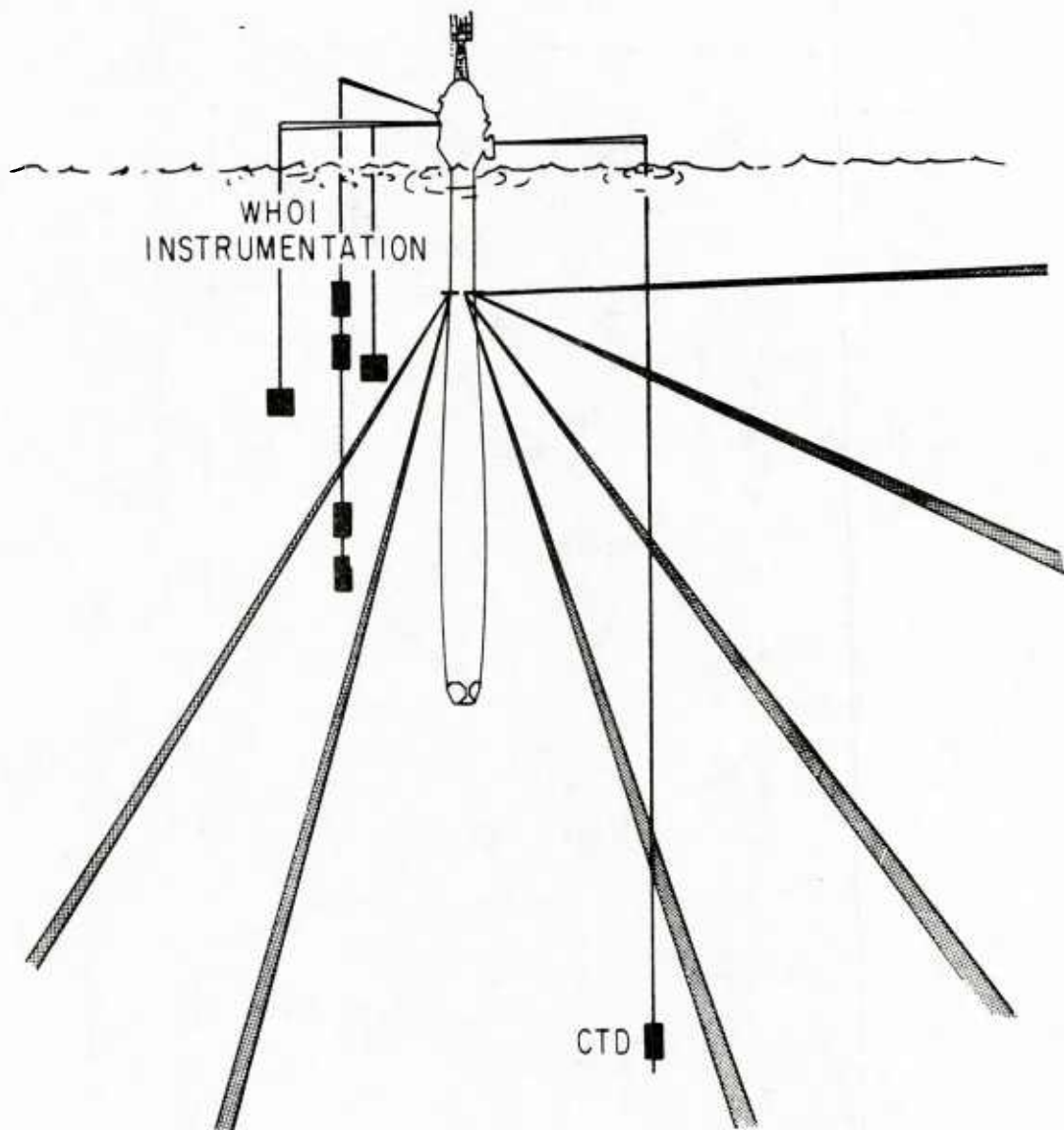


figure 2-5 Schematic diagram of 1983 FLP experiment. Sonar and profiling CTD location are indicated. CTD profiles are obtained to a depth of 310 m every three minutes. The profiling current meter (VMCM) array were developed and operated by R. Weller of WHOI.

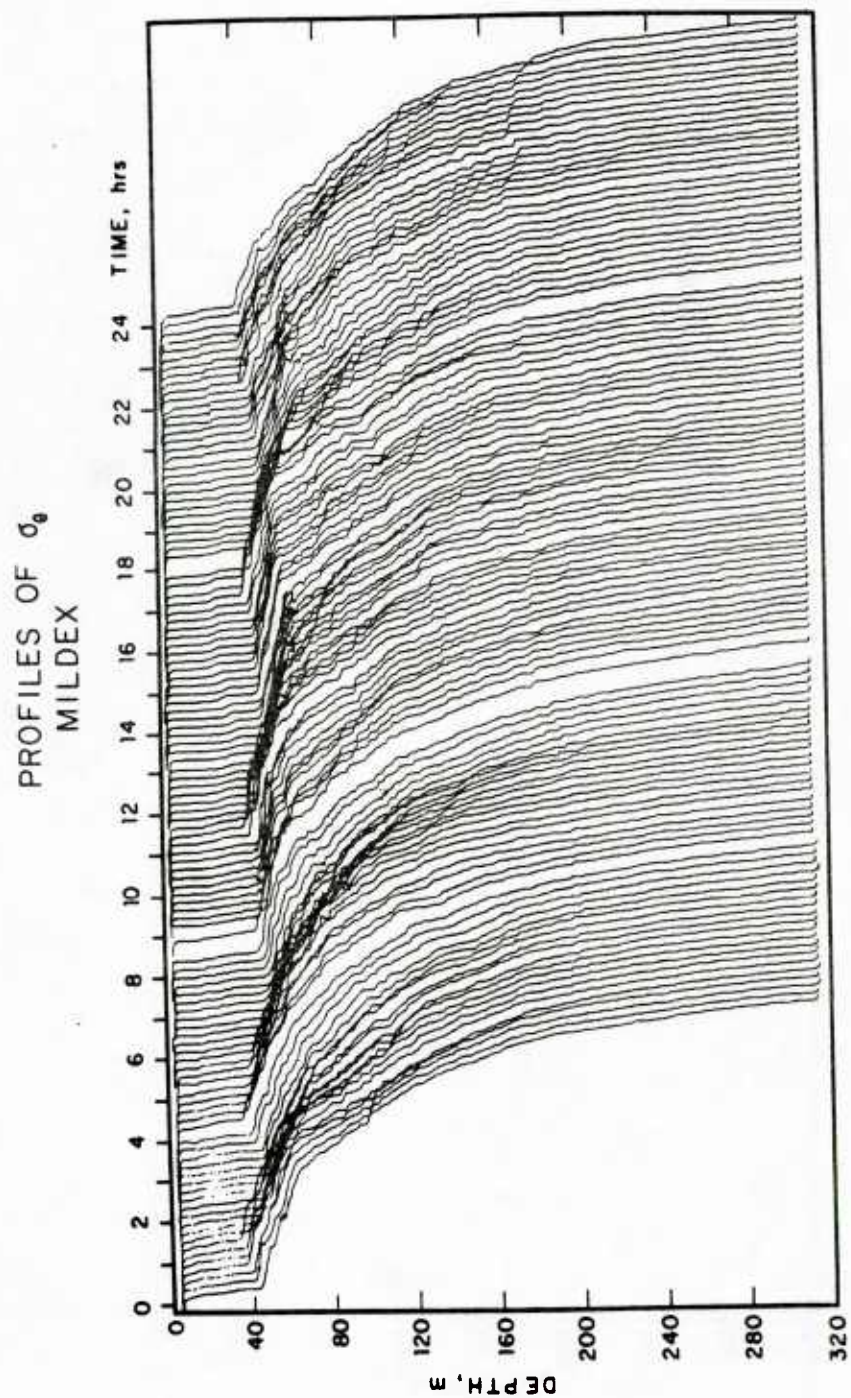


figure 2-6 A sequence of σ_θ profiles covering a 24 hour period during MILDEX.

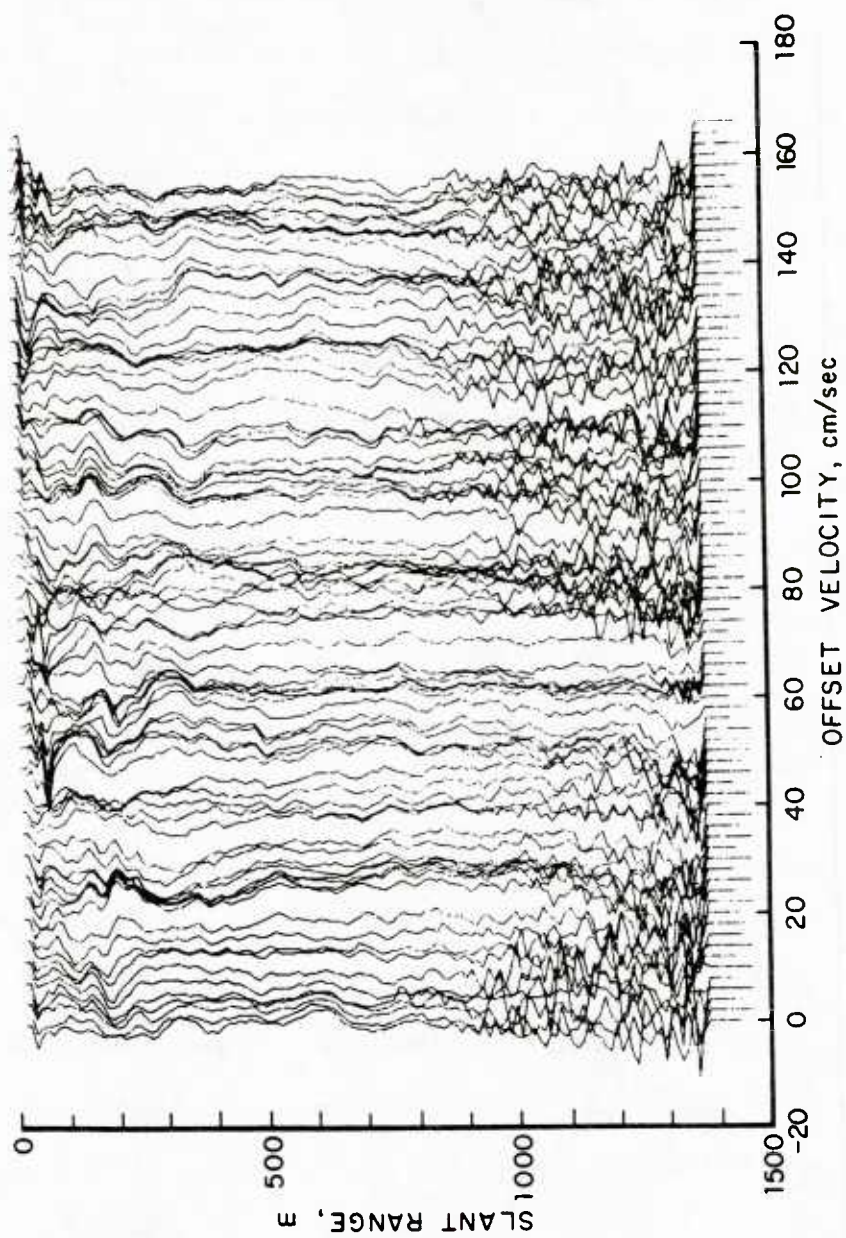


figure 2-7 A sequence of three minute average Doppler sonar velocity profiles recorded during MILDEX (courtesy A. J. Plueddemann).

CHAPTER 3

THE DIRECTIONALITY OF THE INTERNAL TIDE

3.1 Introduction

The words "internal tide" are commonly used to describe internal waves whose frequencies are at or close to that of the M_2 or S_2 barotropic tides. The description in some senses is a misnomer since these barotropic and baroclinic motions exhibit very different behavior. For example, in the deep ocean the barotropic tide has vertical displacements at the surface which are of $O(10\text{ cm})$ and horizontal wavelengths of $O(1000\text{ km})$. The internal tide, on the other hand, has vertical displacements in the ocean interior which are typically much larger, $O(10\text{ m})$, and horizontal wavelengths which are much smaller, $O(100\text{ km})$.

The internal tides, unlike the barotropic tide, do not result from direct astronomical forcing. Instead, the accepted explanation for their existence is that they represent the response to forcing of isopycnal surfaces over topographic features by the barotropic tide. Accordingly, continental slopes, since they are prominent topographic features, should be favored areas of generation. Rattray (1960) and others have developed a linear model which describes the generation of the internal tide at a continental slope. The model predicts that a beam of energy of tidal frequency will propagate into the ocean interior away from the slope. Off the coast of California, the continental slope is a very steep feature called the Patton escarpment which should serve, to a first approximation, as a line source for the internal tide. In an attempt to assess the importance of the escarpment, data collected during MILDEX were analyzed.

3.2 Background

In Wunsch (1975), work describing the topographic generation of the internal tide is reviewed. He notes that three separate but clearly related topographic features, have been identified: steplike finite amplitude changes in depth, small-scale linearizable roughness and finite sloping topography. Steep continental slopes like the Patton escarpment fall into the first category. Rattray (1960) proposes a model to deal with the generation of the internal tide at such step-like features. The model, which is linear, has been improved considerably over the years (e.g. Rattray et al., 1969 and Prinsenberget al.,1974) to include refinements such as non-constant Vaisala frequency, dissipation and finite sloping topography. Typically the model consists of two domains: the ocean over the continental shelf and the ocean over the deeper abyssal plain. Matching boundary conditions for vertical displacement and horizontal velocity are imposed at the shelf break. Many normal modes (~ 100) are required to satisfy these conditions, which results in a beam of energy that propagates away from the slope into the ocean interior (see Fig. 3-1). The beam is bounded by characteristics whose slopes are given by:

$$\frac{dz}{dx} = \pm \left\{ \frac{\omega^2 - f^2}{N^2 - \omega^2} \right\}^{\frac{1}{2}} \quad (3-1)$$

where x and z are the horizontal and vertical co-ordinates and ω , f and N are the semi-diurnal, inertial and Vaisala frequencies.

Several attempts have been made to verify the validity of the model with oceanic data, most of which have proved inconclusive (e.g. Barbee et al., 1975). Perhaps the most encouraging results are due to Regal and Wunsch (1973) who report an intensification, as predicted by theory, of the internal tide at Site D off the east coast of the U.S.A. The most recent example of the model's application can be found in DeWitt et al., (1985) where qualitative agreement is found between theory and

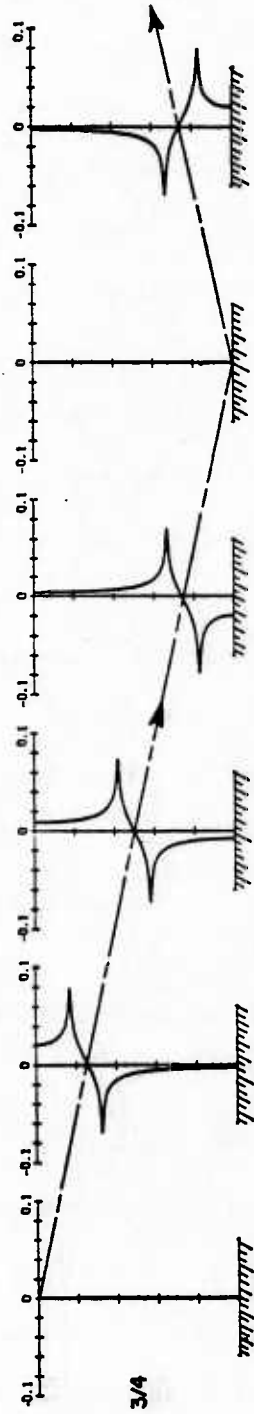


figure 3-1 The generation of a narrow beam of energy at the edge of a step continental shelf (from Rattray et al., 1969). The beam is shown at a series of horizontal locations at a particular instant in time (phase corresponding to three-fourths period).

observation for the JASIN experimental area. Here the Rockall Bank is regarded as the generation region.

If the effects of dissipation are ignored, the beam will remain coherent as it is reflected off the ocean surface and bottom. When these effects are included (Prinsen-berg et al., 1974) the sharp gradients of phase and amplitude, found in the inviscid case at the edges of the beam, disappear and the beam is widened. This behavior results from the fact that the higher modes, which are necessary to "sharpen" the beam, are dissipated more rapidly than the lower modes. Hendershott (1981) offers this explanation as the reason why deep ocean observations of the internal tide show it to be low mode in character.

A limitation of the Rattray model is that it considers only normal incidence of the barotropic to the shelf. The case of oblique incidence, which is more typical, has been considered by Weigand et al (1969) who show that internal waves propagate normal to bathymetric contours regardless of the angle of incidence of the barotropic tide. Oblique incidence of the barotropic tide is indeed the case both off the east and west coasts of the U.S.A. Off California, the barotropic tide is a Kelvin wave propagating anti-clockwise up the coast with its amphidrome located approximately half-way between Hawaii and California. Figure 3-2 describes the situation and is taken from Irish et al. (1971).

The most comprehensive descriptive work on the internal tide reported to date is by Hendry (1977). He describes results from MODE, the site for which was located ~ 700 km east of the Blake escarpment. He finds the first mode to be dominant and presents evidence that the internal tide is propagating towards the MODE area from the Blake escarpment. This picture is consistent with the model described above if the effects of dissipation on higher modes is included.

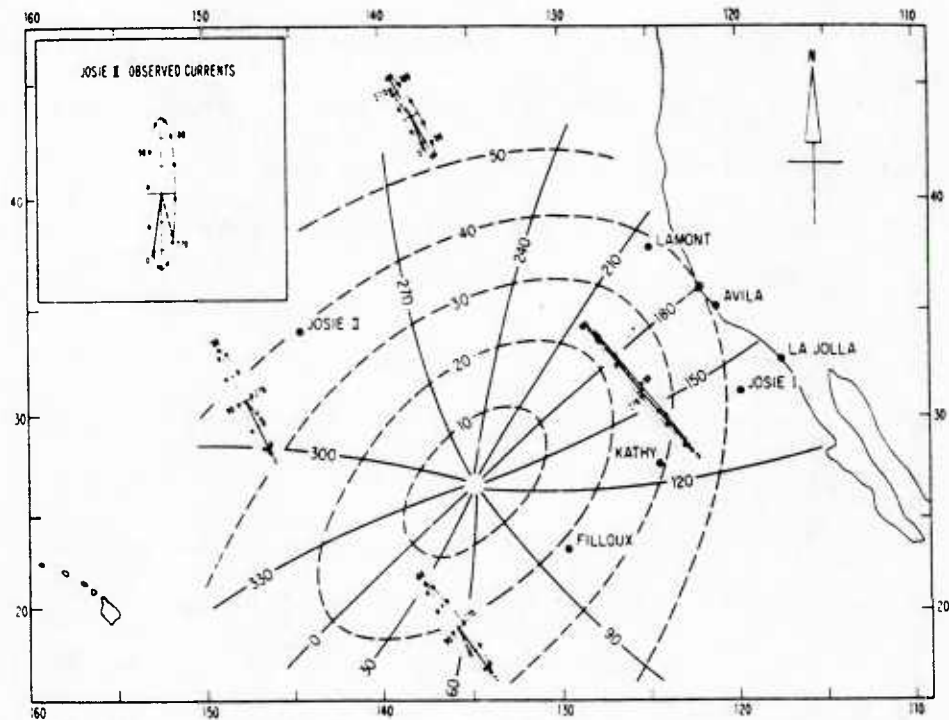


figure 3-2 M_2 cotidal chart from Munk, Snodgrass and Wimbush (1970). Lines of equal amplitude H cm and of equal Greenwich epoch G° are shown by the dashed and solid curves. The heavy arrow toward $G = 0$ is the tidal current when the Moon is over the Greenwich meridian. The dots indicated for 30° , 60° , ... give the end point of the current vector for other Greenwich epochs. The dashed arrow is the current vector at the time of *local* high tide. The inset shows the observed currents at JOSIE II. Tick marks on the major axis of the ellipses correspond to current speeds at intervals of 1 cm/sec.

Very little descriptive work of the internal tide off California has been reported in the literature. However, two notable exceptions are Summers and Emery (1963) and Krauss (1966) which both describe observations in this region. The picture which emerges is of an internal tide which is progressive in character traveling towards the coast both in deep water and in the shallower water over the shelf (see Figure 3-3). These observations are puzzling when one considers the Rattray model and its predictions. With such a prominent feature as the Patton escarpment in the path of the barotropic tide, one expects to observe an internal tide propagating normally away from the escarpment.

3.3 Model Predictions

It is instructive at this point to investigate, at least qualitatively, the predictions of the Rattray model for the area west of California. These will be used later for intercomparison with observations.

The two-dimensional cross-section chosen for analysis is to the east of the MILDEX experimental site (Fig. 2-1). To calculate the characteristics for this region, we must first know the Vaisala profile down to $\sim 4000\text{m}$ (see eqn. 3-1). Since we only have CTD information for the upper ocean, this profile was calculated in two sections, above and below 292.5m. Above 292.5 m, the average profile calculated from the MILDEX CTD casts was used (Fig 3-4). Below 292.5 m, a cubic fit to a composite of 3 deep ocean profiles was used (Fig. 3-5). These were recorded in the MILDEX area on different occasions and obtained from Professor Joseph Reid's archives at Scripps.

The characteristics for the two dimensional section east of the MILDEX experimental area were calculated using this composite Vaisala profile (see Fig. 3-6). The beam of internal tide energy, shaded in the figure, bounces off the ocean floor and surface twice before arriving at the experimental site. During the MILDEX experi-

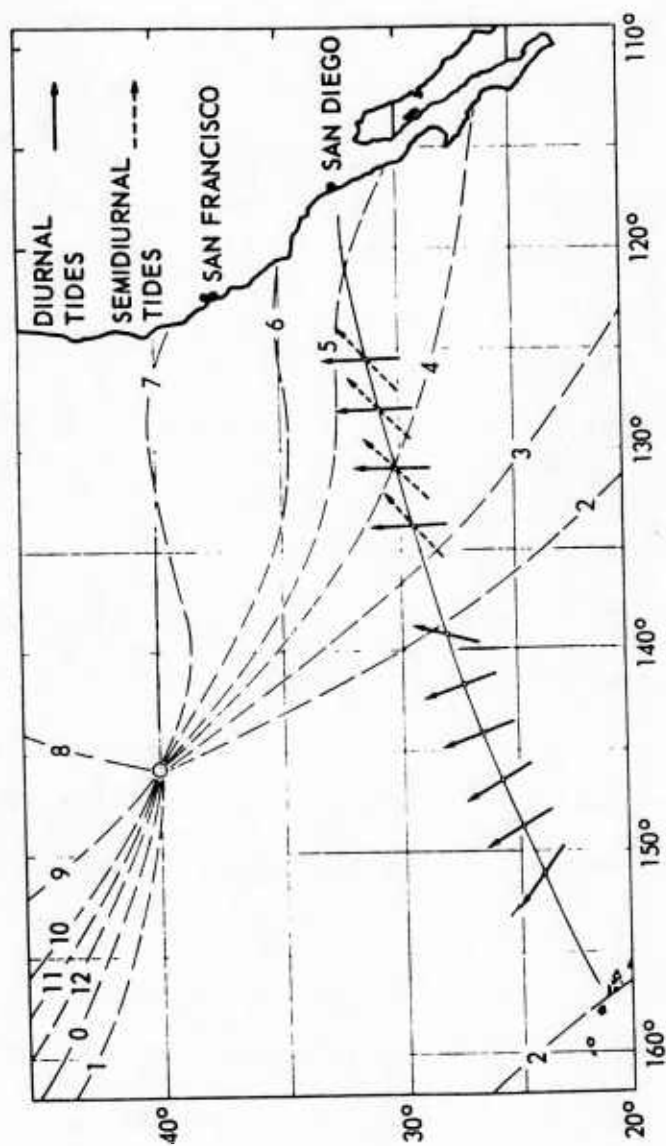


figure 3-3 Cotidal lines of the semi-diurnal tide (from Dietrich, 1944) and the direction of progress of the internal semidiurnal and diurnal tidal waves (from Krauss, 1966).

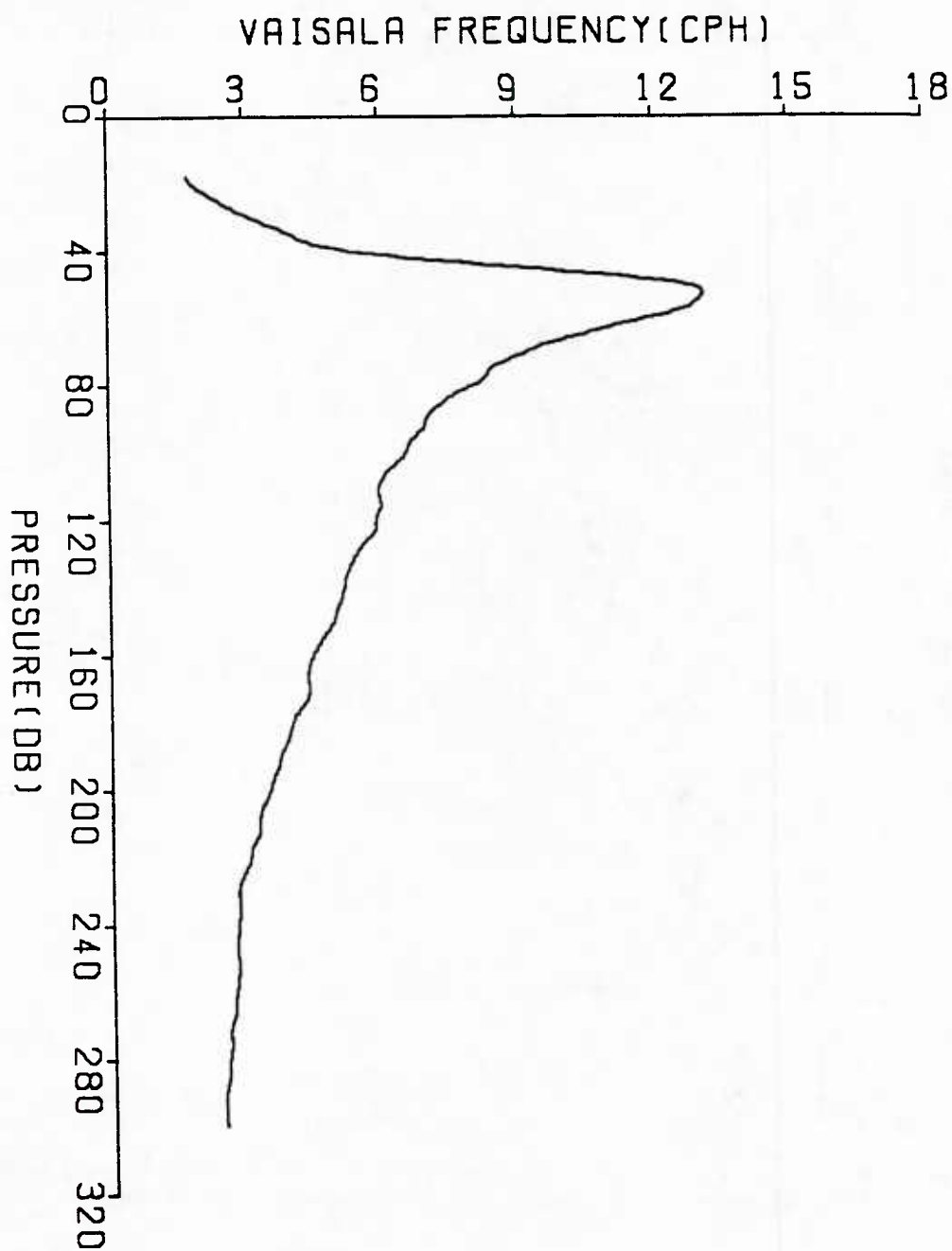


figure 3-4 Average Vaisala frequency profile calculated from 3979 CTD casts taken from October 30 - November 8, 1983 during MILDEX.

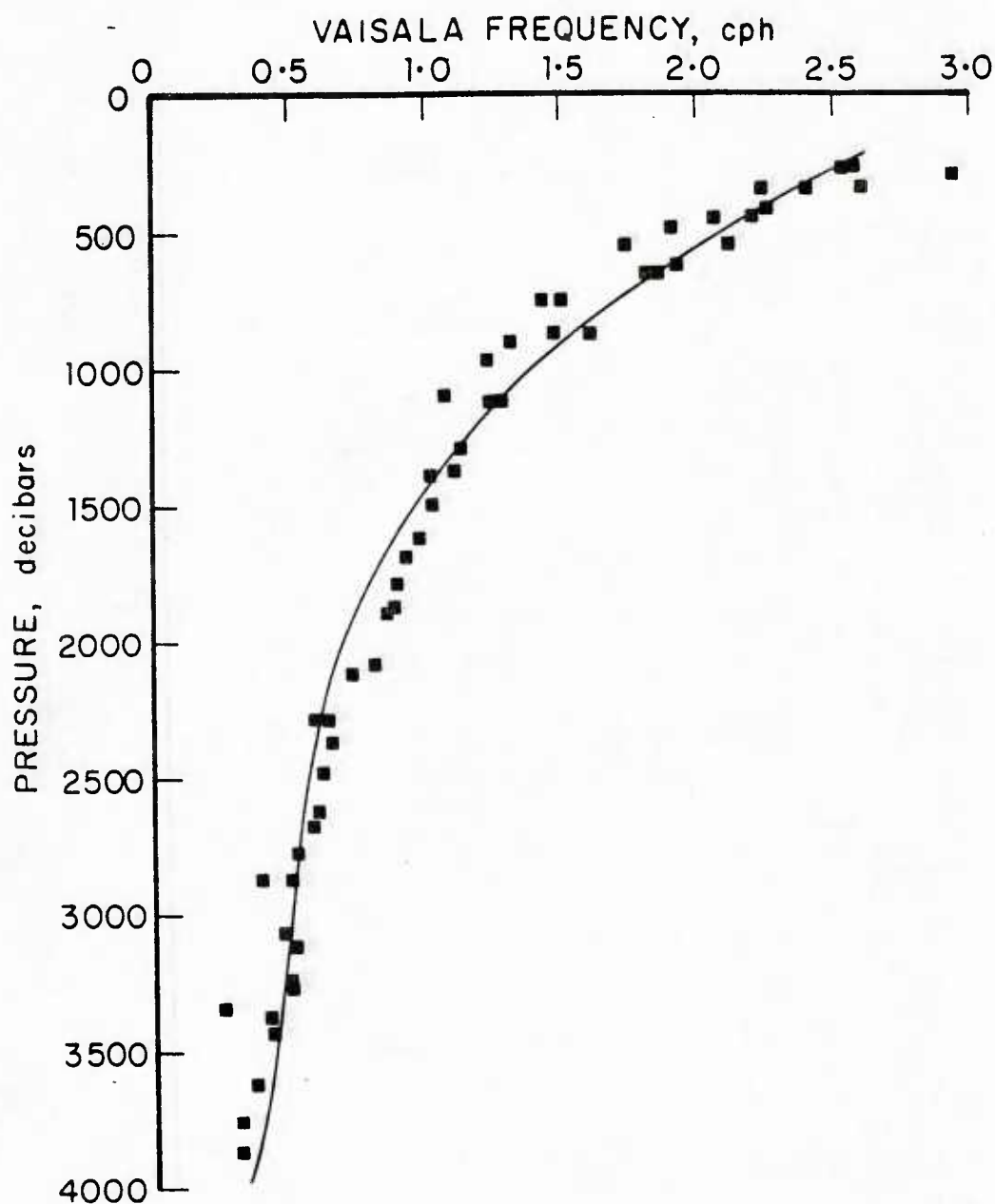


figure 3-5 Deep (> 292.5m) Vaisala frequency profile for the MILDEX area. Data points obtained from the archives of Professor J. Reid at Scripps. The cubic fit obeys the following equation:

$$N(p) = A + Bp + Cp^2 + Dp^3$$

where p is pressure in decibars and

$$\begin{aligned} A &= .3089032 \times 10^1 \\ B &= -.23542899 \times 10^{-2} \\ C &= .7372996 \times 10^{-6} \\ D &= -.80569676 \times 10^{-10} \end{aligned}$$

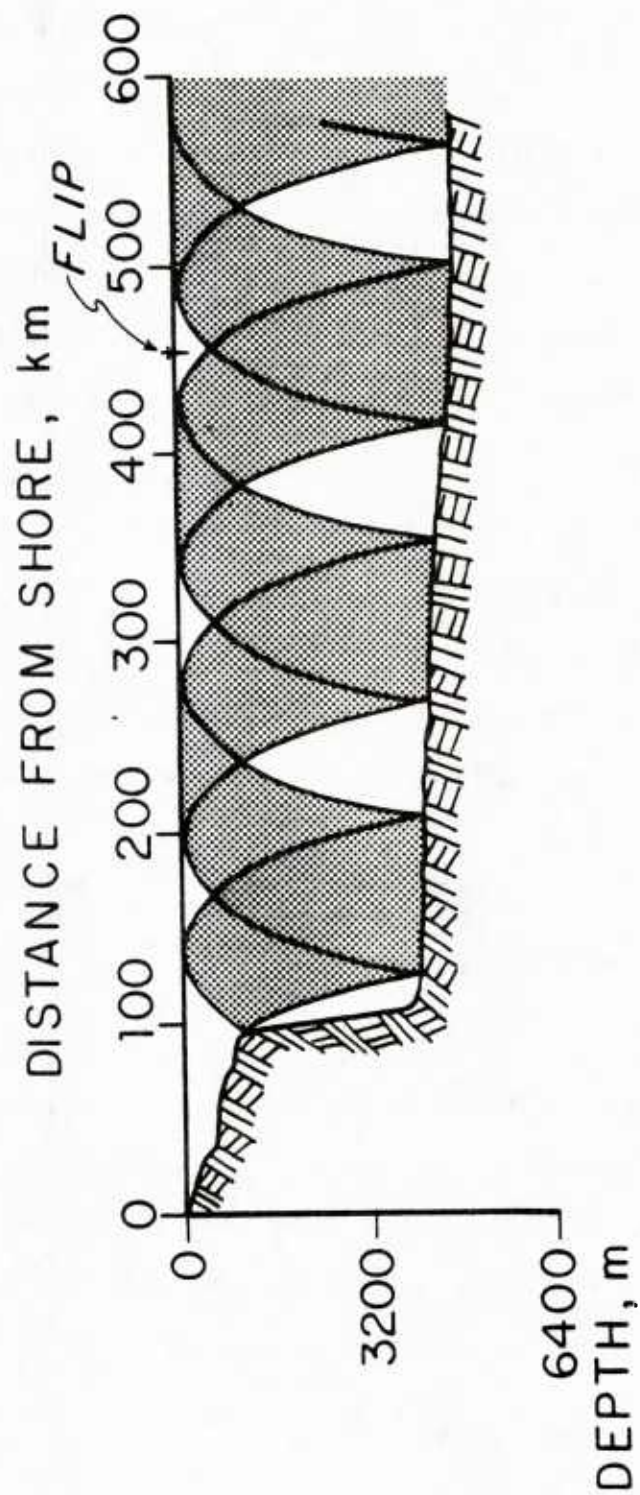


figure 3-6 Internal tide characteristics for a cross-section east of the MILDEX site. Area between characteristics is shaded.

ment FLIP drifted between 400 and 500 km from shore, and in so doing, passed over different sections of the beam. Fig. 3-7 shows the section between 0 and 1200 m in depth over which FLIP drifted. The darkened area is illuminated with tidally energetic motions.

An obvious limitation of the model is its two dimensionality. However, cross-sections normal to the Patton escarpment at other points long its length display similar structure to that shown in Fig. 3-6. With this structure in mind and the fact that the effects of the barotropic tide are felt almost simultaneously* along the escarpment, one can model this topographic feature as a line source for the internal tide in this region.

As the internal tide propagates away from the escarpment, we expect the higher modes to be more rapidly dissipated than the lower modes. This effect will lead to blurring of the edges of the beam. The surviving modes will now be examined in more detail. Define the x -direction as normal to the escarpment and positive in the direction of propagation. The isopycnal displacement, η , and horizontal components of velocity, U and V , are given by:

$$\begin{aligned}\eta &= A\phi(z)\cos(\omega t - kx), \\ U &= \left(\frac{A\omega}{k}\right)\phi'(z)\cos(\omega t - kx), \\ V &= \left(\frac{Af}{k}\right)\phi'(z)\cos\left(\omega t - kx + \frac{\pi}{2}\right)\end{aligned}\tag{3-2}$$

where A is amplitude and $\phi(z)$ is vertical displacement. These equations represent a plane wave whose current vector, (U, V) , will rotate in a clockwise sense in the area under consideration since it lies in the northern hemisphere. The locus of the end points of (U, V) will form an ellipse with its major axis lying along the direction of propagation of the plane wave. For the first baroclinic mode, $\phi'(z) < 0$, in the upper

* The phase speed of the barotropic tide in this region is ~ 700 km/hr.

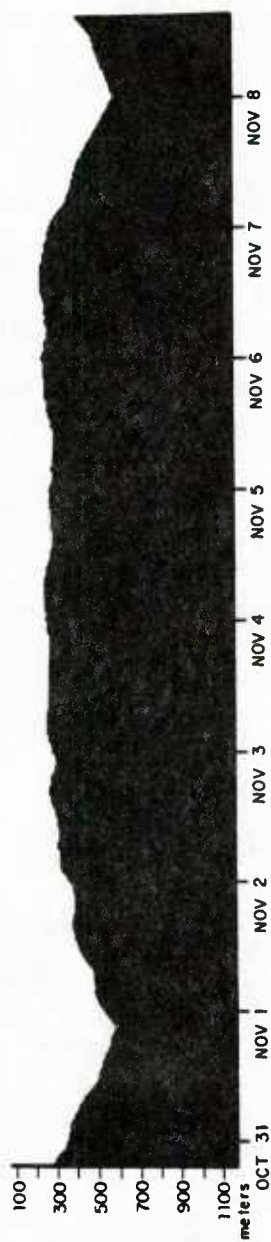


figure 3-7 Section of the beam, shown in figure 3-6, over which FLIP drifted, as a function of time. Dark region is illuminated with tidally energetic motions.

part of the water column so η and U will be 180° out of phase.

In the above I attempt to outline a simple model for the generation and propagation of the internal tide. If it does indeed have some relevance to the situation west of the Patton escarpment, the qualitative features of the predictions should be readily observable. Accordingly, in the MILDEX area we expect to observe the internal tide to be a plane wave propagating away from the escarpment. It will be low mode in character and have current ellipses which have their major axes oriented toward the Patton escarpment. We anticipate a high degree of coherence between the observed internal tide and the barotropic tide at the escarpment, with a corresponding phase lag which is consistent with the travel time from the escarpment to the MILDEX area.

3.4 Comparison with barotropic tide

The barotropic tide in the region west of California takes the form of a Kelvin wave rotating counter-clockwise with its amphidrome approximately midway between California and Hawaii (Irish et al., 1971). From Fig. 3-2 we can infer that the phase speed of this wave is approximately 700 km/hr. According to the model presented in an earlier section, this Kelvin wave interacts with the continental slope to produce an internal tide which propagates normally away from it. If this is the case, the internal tide observed by FLIP should be related deterministically to the barotropic tide at the escarpment, provided it all comes from one point on the escarpment.

In an attempt to resolve this issue, isopycnals obtained from CTD profiles collected during MILDEX were compared to the predicted barotropic tide at station 12 (see Fig. 2-1). In the past bottom pressure records for this deep ocean site have been analyzed for their barotropic tide content. The tidal constants for the station,

calculated by the response method, can be found in Cartwright et al., (1979). The page in Cartwright et al. which refers to this station is reproduced on page 28. In addition, Table 3-2 contains useful information about the tidal constituents. From these constants, the predicted barotropic tide can be generated. Fig. 3-8(A) shows the prediction for the duration of MILDEX.

Isopycnals (surfaces of equal σ_θ values) were calculated from the CTD data. These were low pass filtered below 1 cph and decimated by ten to produce time series 721 points long with a sampling period of 30 minutes. Three of the 155 filtered isopycnals are shown in Fig. 3-8 for depths separated by ~ 100 m. Note that the mean depth of the isopycnals increases towards the end of the experiment indicative, perhaps, of a geostrophically balanced current. Unfortunately, cloud cover prevented the collection of good sea surface temperature satellite images which could have resolved the larger scale motions

The coherence and phase were calculated between each isopycnal and the predicted barotropic tide at station 12. The results for the frequency band 0.075 - 0.085 cph are shown in Fig. 3-9. We see that the level of coherence below the mixed layer is very low (~ 0.2). At greater depths the coherence is higher with an average value of ~ 0.7 . One interpretation of this value is that the barotropic and baroclinic motions are perfectly coherent for approximately half (0.7×0.7) the time over which the analysis was performed. The phase of $\sim 210^\circ$ can be interpreted in two different ways: the internal tide in the MILDEX are can either lead or lag the barotropic tide at station 12 by $\sim 210^\circ$ or $\sim 150^\circ$ respectively. If we assume the horizontal wavelength of the mode 1 internal tide in this region is 100 km, the corresponding phase speed will be 8 km/hr. A crest traveling at this speed will take ~ 44 hours to cover the distance (~ 350 km) between the MILDEX site and the escarpment. The

NORTHEAST PACIFIC OCEAN

2.1.11	31° 02'N	119° 48'W	3640m						
1968	214 - 251			37d					
	G_1 G_2 P_1 K_1				N_2 M_2 S_2 K_2				
Hmb	3.2 20.4 10.6 33.1				10.0 43.2 17.9 5.1				
G^0	180 195 209 209				120 142 135 129				
Recorded variances	967.41 mb ²				1195.84 mb ²				
Residual variances	1.56				0.58				

IGPP Station 'JOSIE-175 SW' bottom pressure, using a 'vibrotion' pressure transducer corrected for temperature from a quartz crystal thermometer. 'Response' analysis with reference to the gravitational potential. Constants are taken from ref. 29; the analysis of this station is also discussed in ref. 30 but using an incorrect normalisation coefficient for the potential. (Ref. 29, 30)

2.1.12	32° 14'N	120° 51'W	3700m						
1968	97 - 105			8d					
Hmb	2.6 22.3 11.1 33.3				9.1 43.1 16.6 4.6				
G^0	170 197 217 217				125 150 145 138				
Recorded variances	349.48 mb ²				1524.29 mb ²				
Residual variances	0.49				0.17				

IGPP Station 'FLICKI-190W' bottom pressure recorded and analysed similarly to 2.1.11. (Ref. 29)

Table 3-1 Tidal constants for station 12.

SOLAR	DOODSON	SYMBOL	FREQ(CPD)
1-4	1 2 0 0	ZQ1	0.85695241
1-4	3 0 0 0	SIGM	0.86180932
1-3	1 1 0 0	Q1	0.89324406
1-3	3-1 0 0	R01	0.89810097
1-2	1 0 0 0	O1	0.92953571
1-1	1 1 0 0	M1	0.96644626
1 0	-2 0 0 1	P1T	0.99452431
1 0	-1 0 0 0	P1	0.99776209
1 0	1 0 0 0	K1	1.00273791
1 1	1-1 0 0	J1	1.03902955
1 2	1 0 0 0	001	1.07594011
2-4	2 2 0 0	2N2	1.85969032
2-4	4 0 0 0	MU2	1.86454723
2-3	2 1 0 0	N2	1.89592197
2-3	4-1 0 0	NU2	1.90083887
2-2	2 0 0 0	M2	1.93227361
2-1	2-1 0 0	L2	1.96856526
2 0	-1 0 0 1	T2	1.99776222
2 0	0 0 0 0	S2	2.00000000
2 0	2 0 0 0	K2	2.00547582

Table 3-2 Information about tidal constituents.

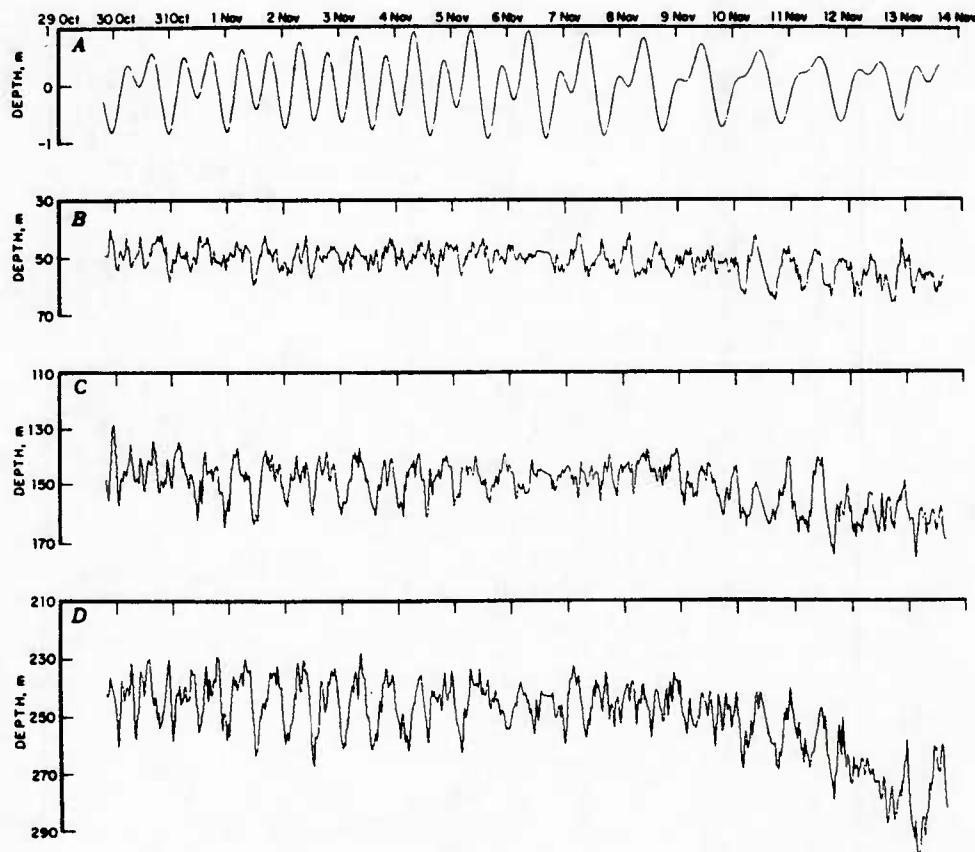


figure 3-8 A) The predicted barotropic tide at station 12 B), C) and D) show isopycnals at different depths.

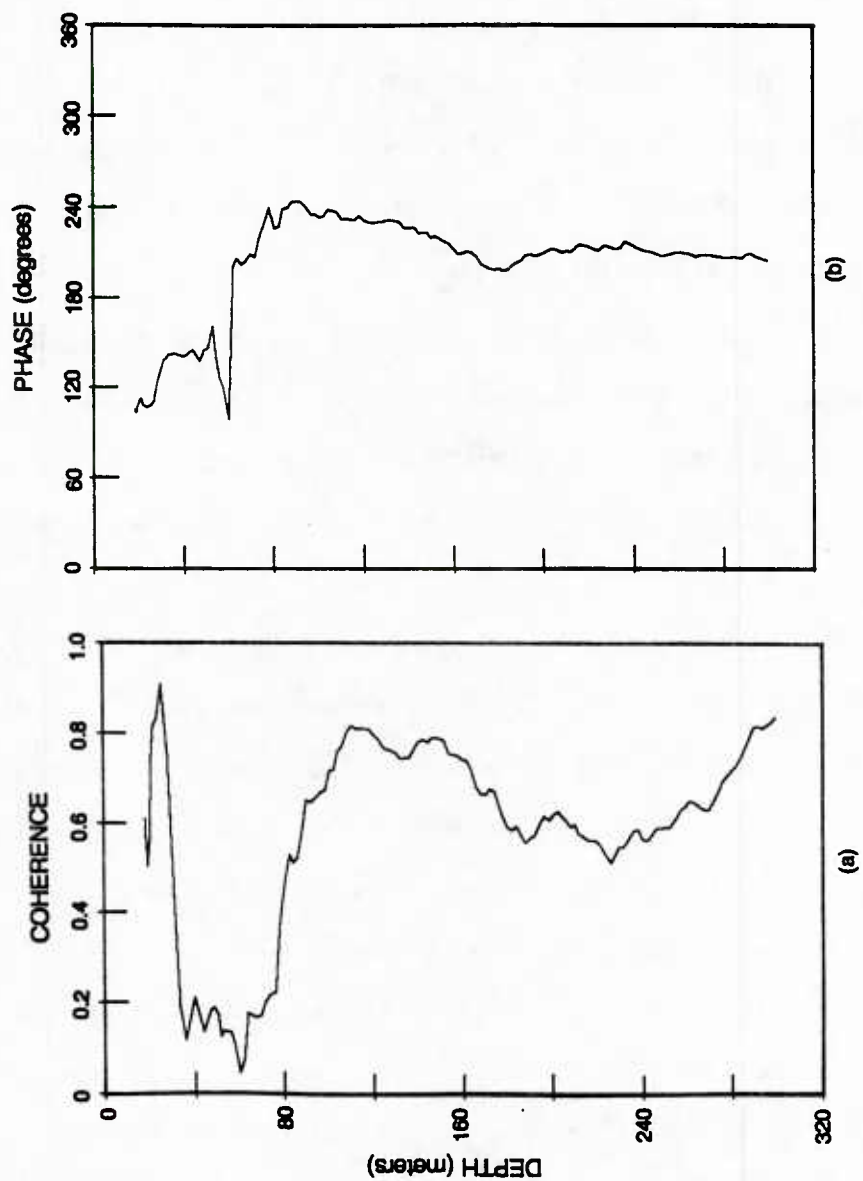


figure 3-9 A) The coherence between the barotropic tide and the isopycnals over the frequency range 0.075 - 0.085 cph (5 frequency bins).

figure 3-9 B) The phase between the barotropic tide and the isopycnals over the frequency range 0.075 - 0.085 cph (5 frequency bins)

corresponding phase lag is 187° , a value which is fairly consistent with either interpretation.

3.5 Analysis of the Doppler data

FLIP recorded Doppler sonar data from 27 October - 15 November. Except for the period at the end of the experiment (after 10 November), when the weather was bad, FLIP's headings were held constant at all times with the aid of the hull mounted thruster. These headings were chosen such that the downward looking beams always pointed towards the north, south, east and west.

The section between 27 October and 13 November was chosen for analysis. The slant velocity from a single sonar beam is composed of both vertical and horizontal currents projected onto the beam axis. By combining information from east-west and north-south beam pairs, the vertical component of velocity is eliminated and time series of horizontal velocity composed of east-west and north-south components are produced. Complete details of the Doppler sonar data analysis are given in Plueddemann (1985). Fig. 3-10 shows subsets of these time series equally spaced in depth. Data points are separated in time by 12 minutes and each time series consists of 2014 (16.8 days) points. These time series represent velocity measurements in cm/sec relative to FLIP. Velocity measurements in Earth co-ordinates were obtained by adding FLIP's drift velocities (Fig. 3-11) to these measurements (Fig. 3-12). These corrected time series were filtered with a Finite Impulse Response (FIR) filter in the time domain between 0.06 and 0.1 cph which is a frequency band centered at the semi-diurnal tidal frequency ($1/12.5$ hours = 0.08 cph). The 129 point filter used was designed with the McLellan and Parks algorithm (Programs for Digital Signal Processing, 1979). These filtered time series were decimated by 5 to obtain records 402 points long with a sampling period of 1 hour (Fig. 3-13). Note that, for the most part, the

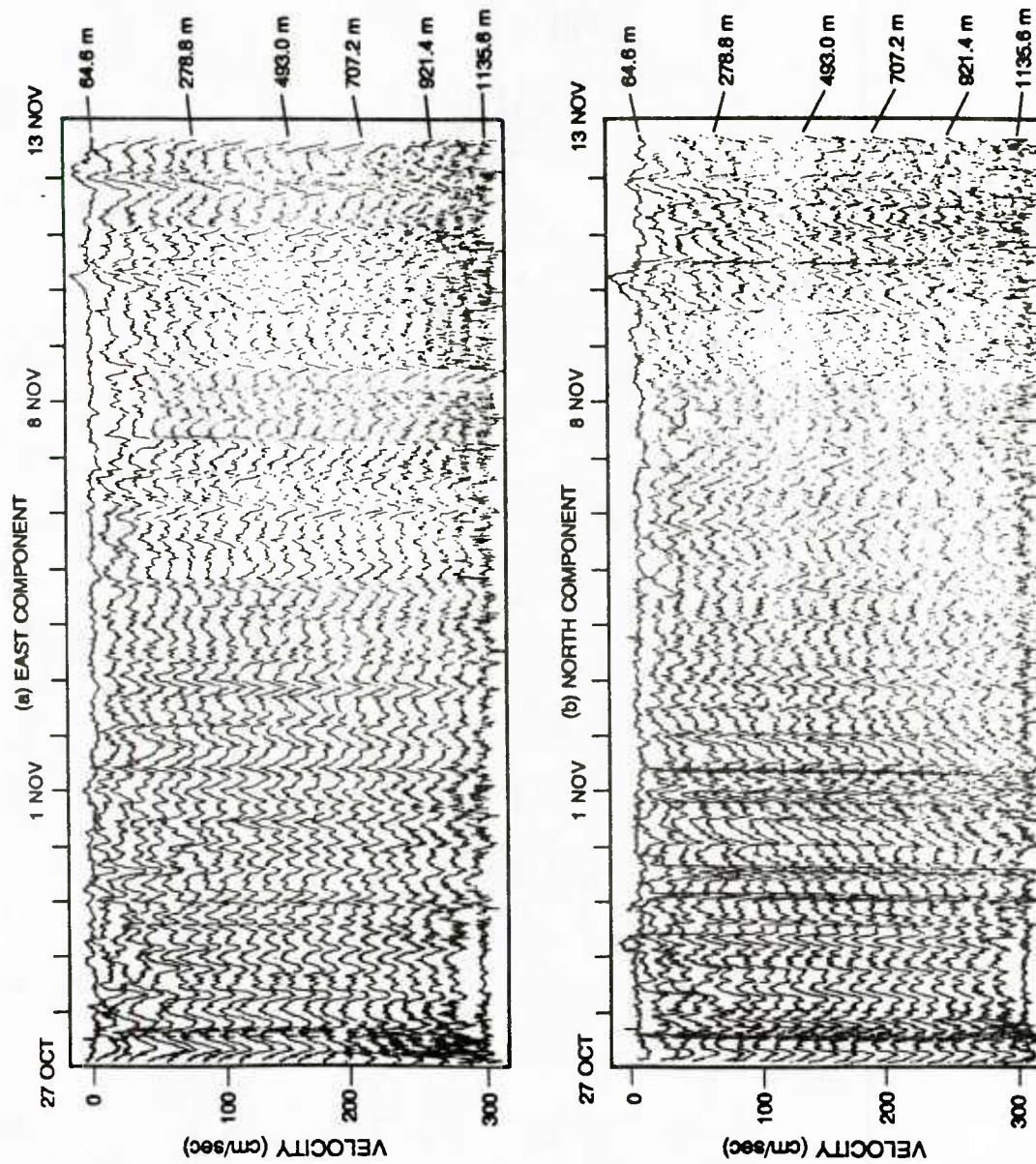


figure 3-10 East (A) and north (B) components of horizontal velocity relative to FLIP. Time series are offset by 15 cm/sec. Scaling is correct for topmost time series.

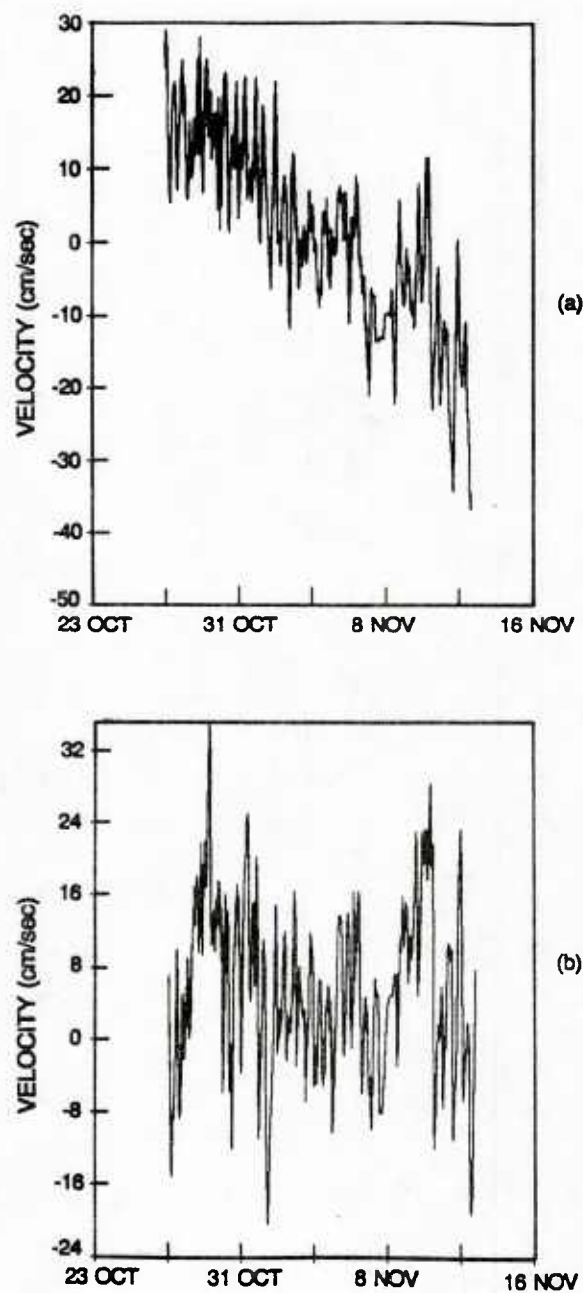


figure 3-11 East (A) and north (B) components of FLIP's drift velocity. Data courtesy of Robert Weller, WHOI.

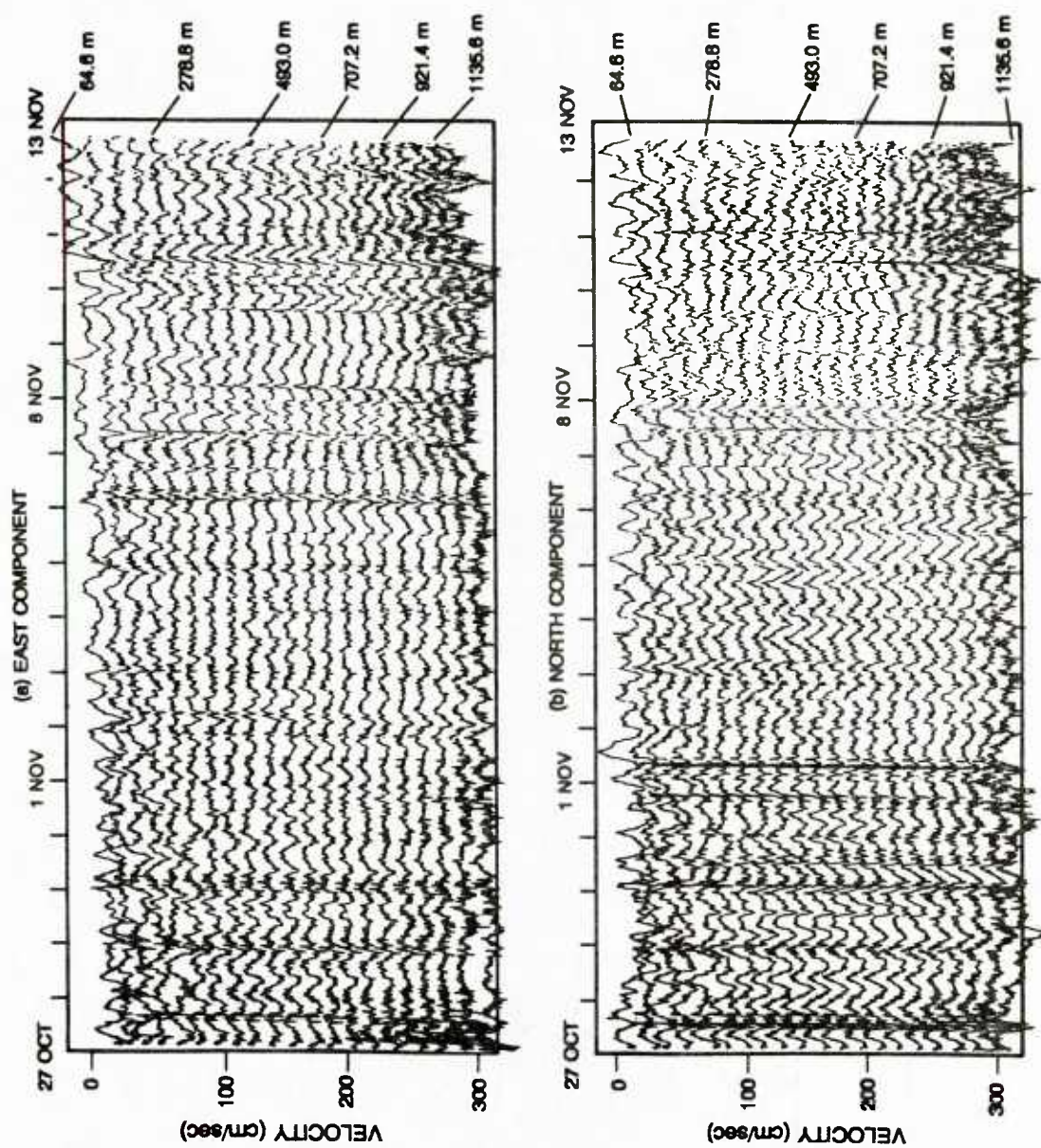


figure 3-12 East (A) and north (B) components of horizontal velocity relative to Earth. Time series are offset by 15 cm/sec. Scaling is correct for topmost time series.

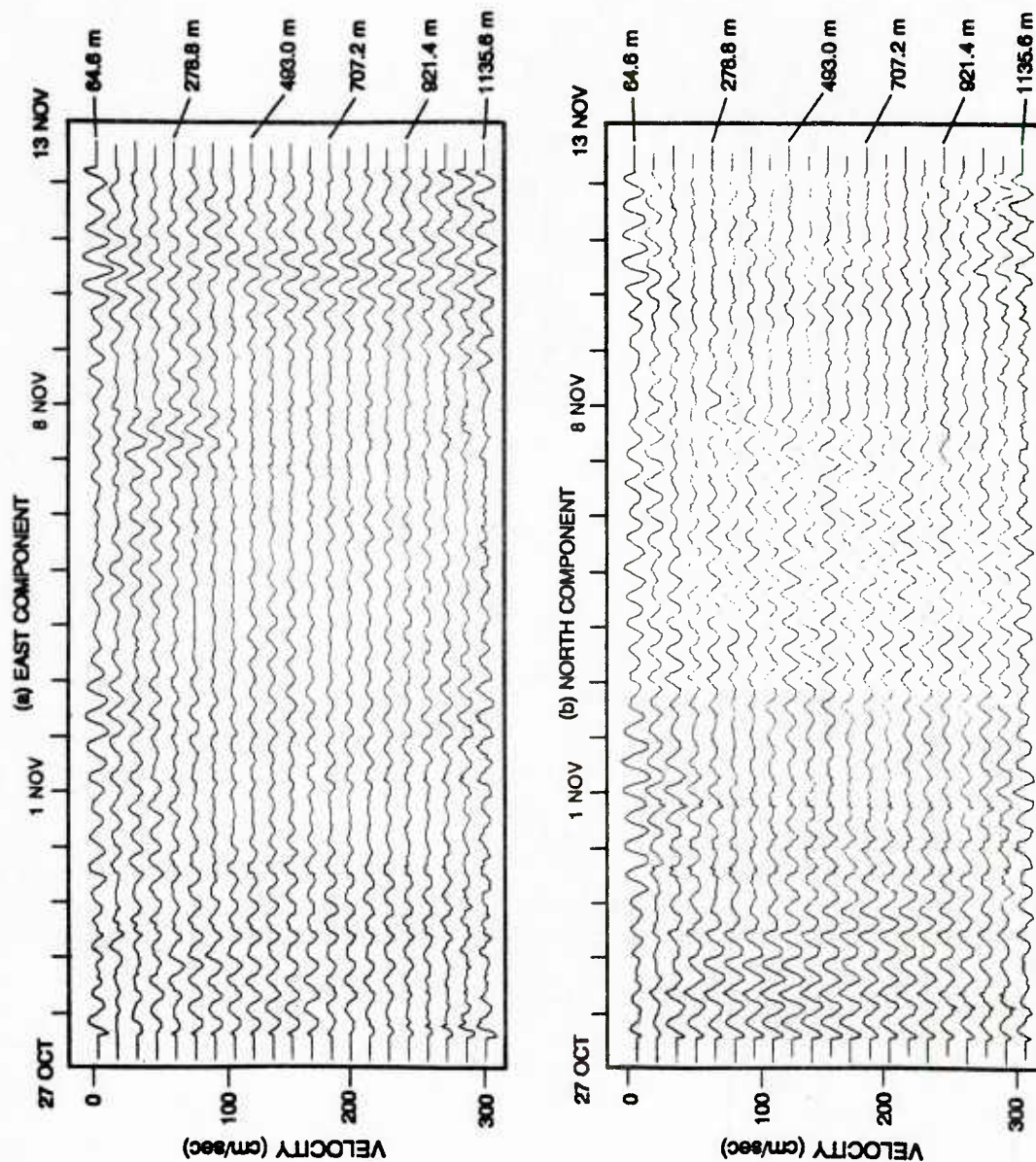


figure 3-13 East (A) and north (B) components of horizontal velocity in the semi-diurnal tidal frequency band. Time series are offset by 15 cm/sec. Scaling is correct for topmost time series.

tidal motions are coherent with depth indicating that they are low mode. This observation is consistent with the isopycnal data (Fig. 5-16) and other observations of the internal tide in the deep ocean (Hendershott, 1981). A cursory inspection of Fig. 3-13 reveals that the direction of propagation certainly does not favor an east-west orientation which would be the case if the Patton escarpment were the predominant source for the internal tide in this region.

In an effort to quantify the direction of propagation and magnitude of the internal tide, a technique can be used which involves finding the principal axes of a vector field (see Appendix F). In general, the locus of the end-points of the current velocity vectors for the internal tide over one tidal cycle form, to a first approximation, an ellipse. Three parameters describe this ellipse. They are: R , the root mean square magnitude of the ellipse; P , the polarization index; and θ the angle the major axis makes in a clockwise sense with north. R , P and θ can be calculated with the subroutine PRINA a copy of which can be found in Appendix F. R (in cm/sec) is a measure of the size of the ellipse. P is a measure of its degree of polarization, with 0 indicating an isotropic field and 1 a linearly polarized field. Values of θ are only meaningful when the corresponding values of P are high.

A 13 point (13 hour long) moving window was applied to each pair of north-south and east-west velocity time series and corresponding time series of R , P and θ calculated. Fig 3-14 shows the results for the depth ~ 404 m. The patterns exhibited by these three parameters are very coherent with depth, an observation which is consistent with the low mode behavior remarked upon previously. Because of this depth independent behavior, it was decided that the majority of the useful information about directionality could be obtained by just analyzing the range average velocity time series. These are displayed in Fig 3-15. We see that, for the most part, the strongest velocity signal is contained in the north-south component. However, there is

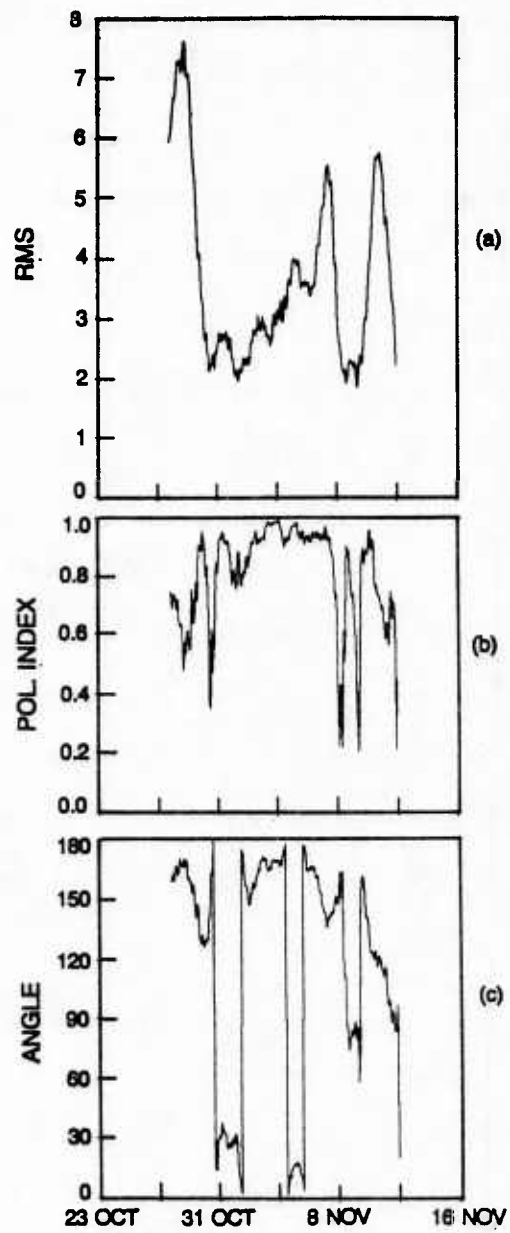


figure 3-14 A) rms B) polarization index and C) angle clockwise from north of the major axis for the depth 404 m.

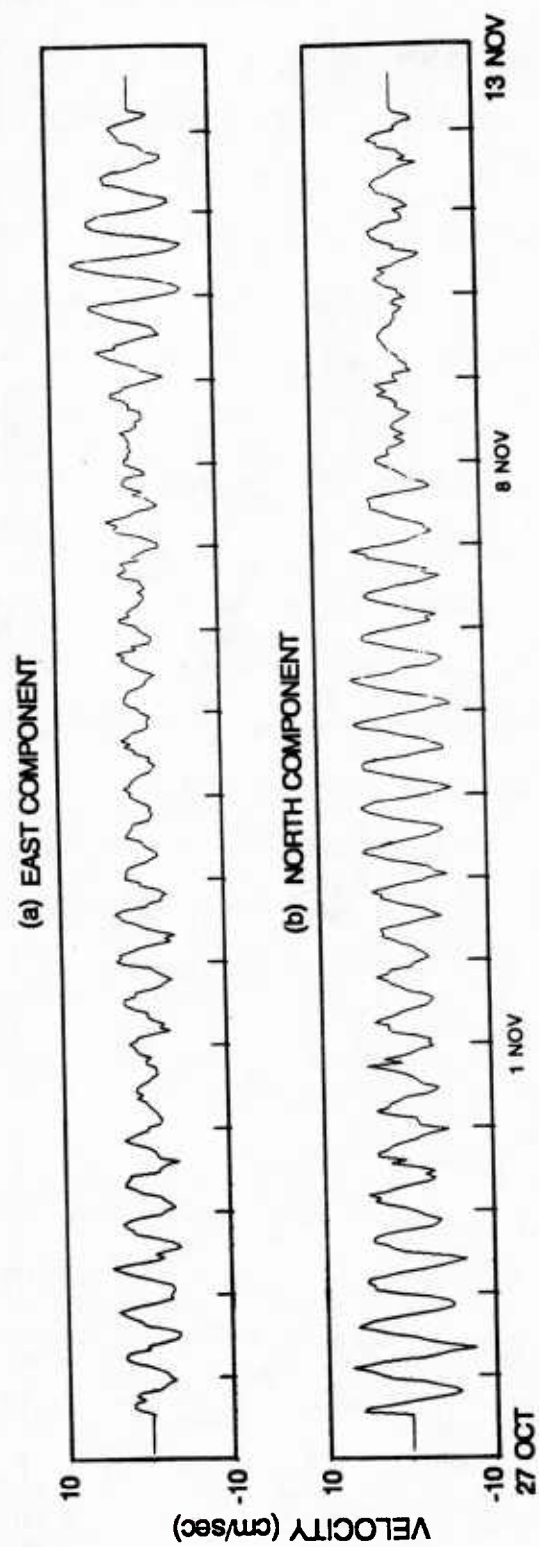


figure 3-15 East (A) and north (B) components of range average horizontal velocity in the semi-diurnal tidal frequency band.

a period from 9-12 November when this behavior is reversed and the strongest signal appears in the east-west component. The magnitude of the velocities can be as high as 8 cm/sec which is higher than the predicted values for the barotropic tidal velocities in this region (~ 2 cm/sec). Accordingly, we conclude that, at least during periods of more energetic motions, the observed signal is mostly the result of low mode baroclinic motion. R , P and θ were calculated from these two range average time series and are displayed in Fig. 3-16. From Fig 3-16(A) we see that the most intense motions occur at the beginning (~ 27 October), in the middle (~ 4 November) and at the end of the experiment (~ 10 November). For the most part, the ellipses are strongly polarized with P values exceeding 0.8. During these periods, the directionality can be inferred from the corresponding value of θ which, for most of the experiment, has a value centered at 150° . The discontinuity that occurs about 8 November is an artifact of the ambiguous definition of θ : values which jump between 0° and 180° indicate the major axis of the ellipse has an approximate north-south orientation. Except for the period after 8 November, the orientation of the major axis is approximately 150° - 330° . This certainly is the case between 1 November and 6 November when the polarization index is very high (~ 0.9). During this period we can conclude that the internal tide is coming from $\sim 150^\circ$ or $\sim 330^\circ$. To resolve this directional ambiguity, a technique can be applied which is described in Hendry (1977). We know that, for a low mode progressive internal wave, the vertical displacement and the horizontal velocity must be 180° out of phase in the direction of phase propagation above the node for horizontal velocity. Let us assume, for the purposes of this discussion, that the internal tide is low mode and comes from either the north or the south during the period 1 - 6 November. From Figs. 3-15, 3-8 and 5-16 we see that, during this period, the vertical displacement of the isopycnals and the north-south velocity component are approximately in phase implying that the internal tide is com-

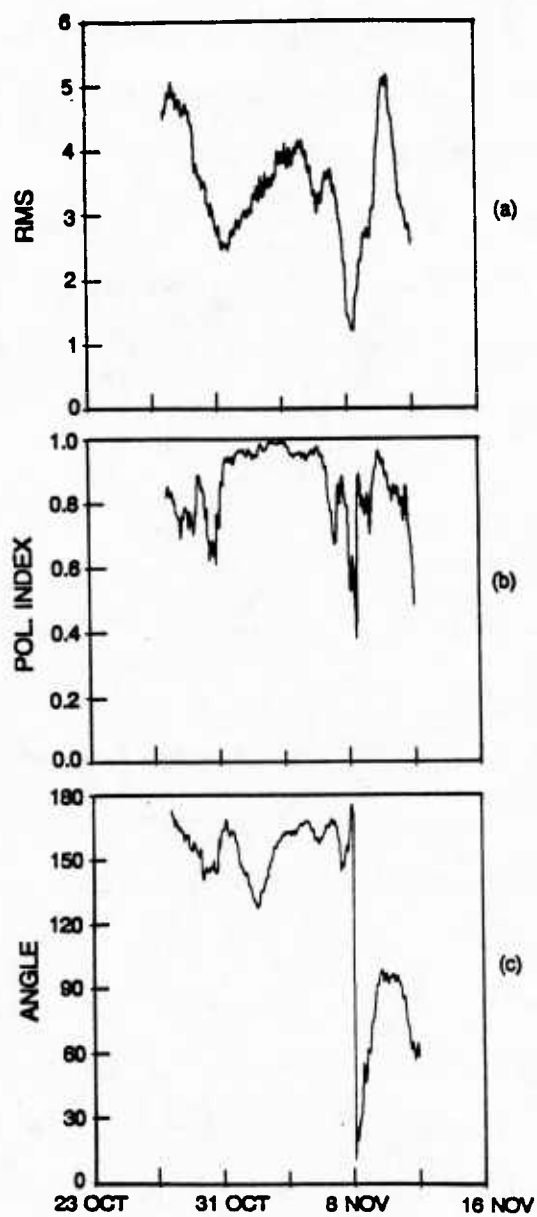


figure 3-16 A) and B) polarization index and C) angle clockwise from north of the major axis for time series shown in Figure 3-15.

ing from the north. This observation resolves the ambiguity and leads us to conclude that the direction of propagation is from the NNW to SSE. This finding is consistent with those of Murray Levine (OSU) whose studies of data, collected by current meters and thermistors attached to the drifting buoy, show that the internal tide is coming from the north during the period 27 - 28 October.

The same method described above can be used to resolve the directional ambiguity for the period at the end of the experiment when θ takes on a value of $\sim 90^\circ$ or $\sim 270^\circ$. The conclusion is that the internal tide comes from the east during this period.

3.6 Discussion

The work described in this chapter is an attempt to determine the directionality of the internal tide in the deep ocean west of California. In particular, the study was motivated by a desire to assess whether the Patton escarpment is the major source for the internal tide in this region. This latter view is not supported by the data.

For the duration of MILDEX, an analysis of Doppler sonar and CTD data indicates that the internal tide is low mode in character and has a direction of propagation which is variable. However, for the majority of the experiment, there appears to be a favored directionality which is approximately from the NNW to SSE. This conclusion is consistent with values of phase and coherence between the vertical displacements of the barotropic tide at station 12 and the internal tide in the MILDEX area if the phase is interpreted as a phase lead. These findings are in approximate agreement with those of Murray Levine (OSU) who finds that the internal tide is coming from the north.

The situation which the data depict is not at all consistent with a "Rattray-

type" model such as the one described in this chapter: the Patton escarpment does not appear to be the major source of the internal tide in this region and no beamlike behavior is observed. Other mechanisms must be considered if the observations are to be more fully understood. These may include generation of the internal tide by the barotropic tide passing over seamounts and the backscattering of the internal tide by topographic features.

CHAPTER 4

INTERNAL WAVE SPECTRAL HARMONICS: A COMPARISON OF MEASUREMENT TECHNIQUES

4.1 Introduction

Discrete harmonic frequencies of the semi-diurnal tide and/or inertial frequencies are being found in the oceanic internal wave spectrum. At issue is whether these harmonics appear because the wavefield is inherently nonlinear, or because the sensors which provide the measurements are contaminated by fine structure in the background gradients of the measured fields. In an effort to resolve this issue, the temperature profiles collected in 1980 were analyzed. Repeated profiling information, like these data, is of interest because it can be analyzed in a variety of ways, each of which responds differently to potential sources of nonlinearity in the measurements. Spectra from fixed depth fine structure contaminated time series, fixed depth uncontaminated series, and isotherm following series are compared in an effort to determine the nature of the observed spectral harmonics.

4.2 Observations of Harmonics

Strong peaks at the harmonics of the semi-diurnal tidal frequency have been observed in many internal wave spectra. Sabinin and Shulepov (1981) present a spectrum of temperature fluctuations which exhibit strong harmonic structure (Fig. 4-1). Davis et al (1981) report harmonics in temperature spectra (Fig. 4-2) calculated from data collected near Ocean Station Papa during MILE. Levine et al (1983) report harmonics in vertical displacement and horizontal kinetic energy spectra (Fig. 4-3) for data collected during JASIN in the N.E. Atlantic. Fu (1981) reports harmonics in horizontal kinetic energy spectra (Fig. 4-4) for Polymode data and Müller et al (1978)

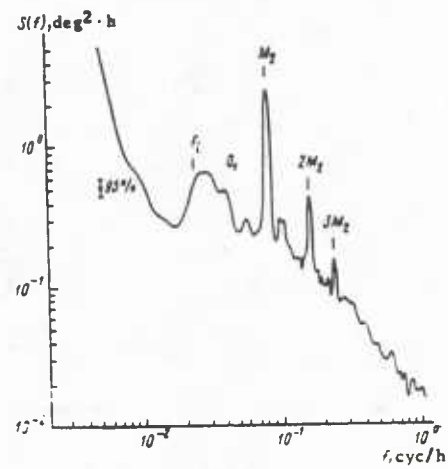


figure 4-1 Spectrum of temperature fluctuations in 1970 Hydrophysical Test Range (from Sabinin and Shulepov, 1981). f_i is the inertial frequency, O_1 is the solar diurnal period, M_2 is the lunar semidiurnal period, $2M_2$ and $3M_2$ are harmonics of the lunar period.

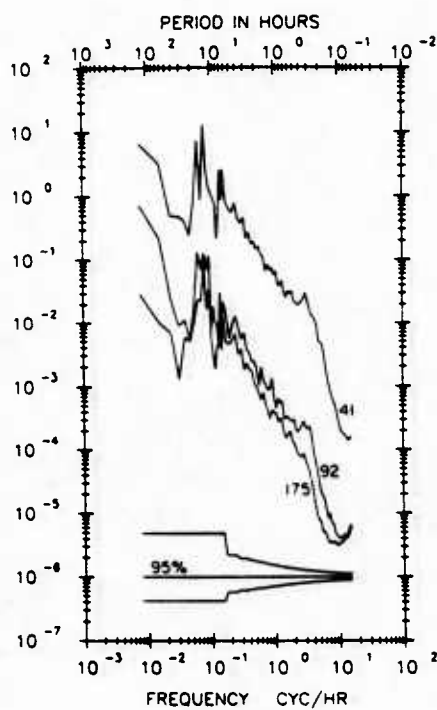


figure 4-2 Spectra for MILE data (from Davis et al., 1981). Temperature spectra of T1.41, T1.92, and T1.175. Each curve is labeled with the depth. The 95% confidence interval for variable bandwidth averaging is shown at bottom. Temperature variance is the integral of the spectrum over positive frequencies.

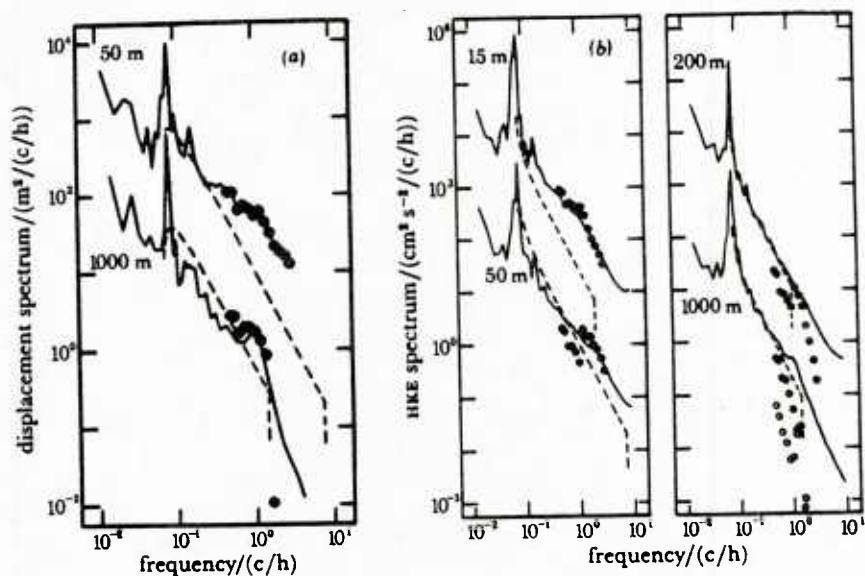


figure 4-3 Spectra for JASIN data (from Levine et al., 1983). Observed average spectra (solid line) are shown along with the GM model (dashed line) and the three-mode model (solid symbols). (a) Frequency spectra of vertical displacement from B1 at 50 m (offset by 10^2) and from W1 at 1000m. (b) Frequency spectra of HKE from W2 at 15 m (offset by 10^2) and 50 m and W1 at 200 m (offset by 10^2) and 1000m. At 1000 m the two-mode model is indicated by open symbols.

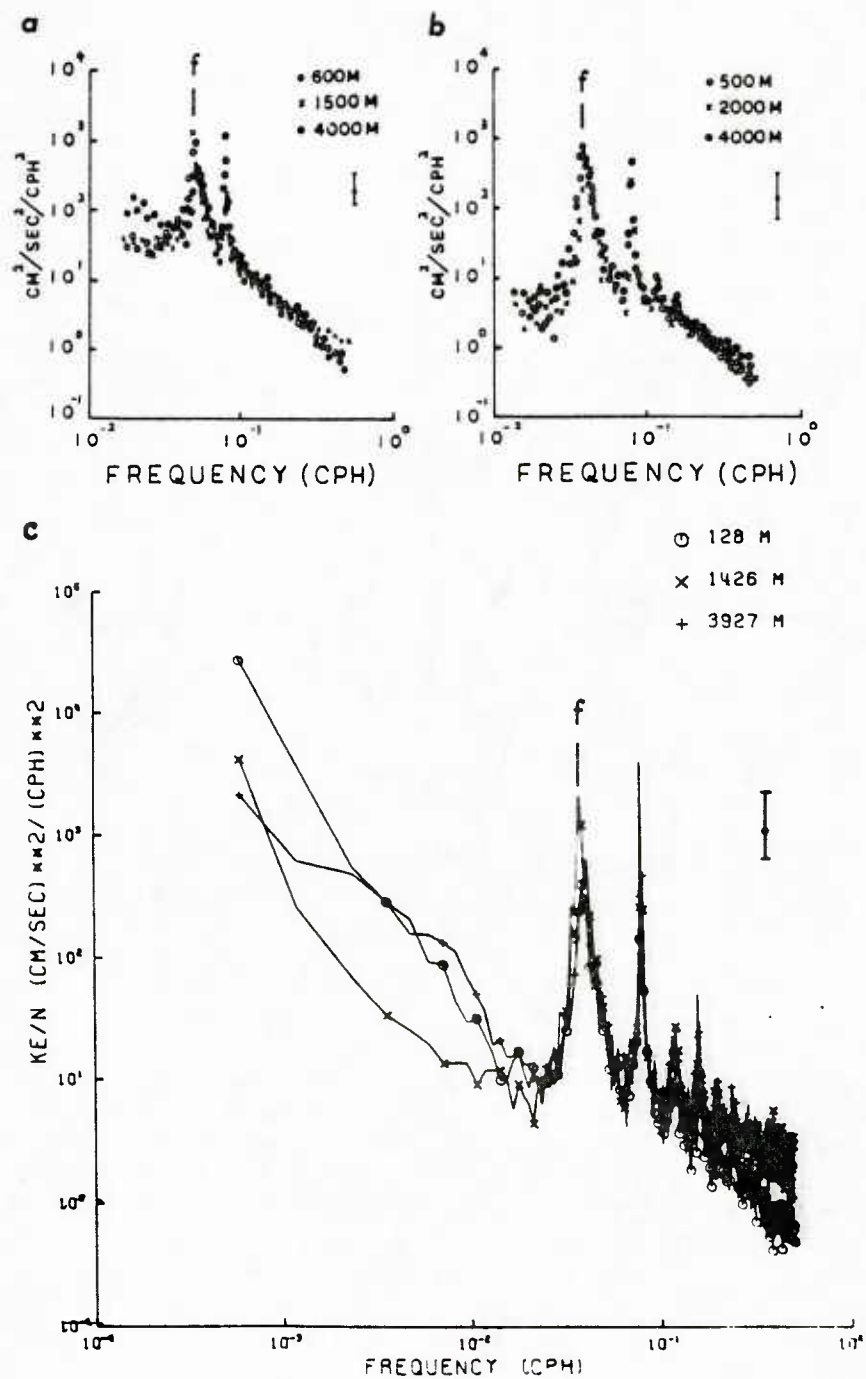


figure 4-4 Spectra for POLYMODE data (from Fu, 1981). Normalized horizontal kinetic energy spectra at (a) station 3 of the PMII (smooth topography), (b) station 546 of the PMI (rough topography), and (c) station 623 of the PMIII cluster B (near the Mid-Atlantic Ridge, very rough topography). Error bar is 95% confidence limit.

report harmonics for the IWEX data.

Pinkel (1981) reports spectra of vertical velocity which show levels of spectral density at the tidal harmonics greater at some depths than at the tidal frequency itself (Fig. 4-5). Peaks at the sum of the tidal and near inertial frequencies are also observed. The relative magnitude of these harmonics appears to be greater at the shallower depths i.e., in the thermocline. This pattern, as we shall see, is repeated in spectra calculated from more recent data sets. Pinkel (1983) presents depth averaged spectra (100-450m) of clockwise acceleration which show harmonics of the near-inertial frequency as well as of the tidal frequency (Fig. 4-6). The relative magnitude of these harmonics is observed to increase with increasing magnitude of the fundamentals (i.e. the inertial and tidal peaks).

4.3 Finestructure Contamination

All the reports to date of harmonics in internal wave spectra, except for those based on FLIP data, are derived from measurements collected by fixed depth sensors. Eulerian measurements of this kind are subject to finestructure contamination which can produce spectral harmonics.

Suppose that we consider measurements of temperature and assume, for the sake of argument, that isothermal surfaces in the sea are sinusoidally deformed by internal waves. Phillips (1971) has demonstrated that the output of a fixed depth temperature sensor will not be sinusoidal if the background temperature gradient is not linear. With a step-like background gradient, harmonics of the sinusoidal vertical displacement record can appear in the fixed depth sensor output. Desaubies and Gregg (1981) have pointed out that, even if the average oceanic temperature gradient is linear, the internal wavefield is sufficiently intense to distort it significantly. The distortion occurs in fixed phase with the wave displacement and results in a nonlinear

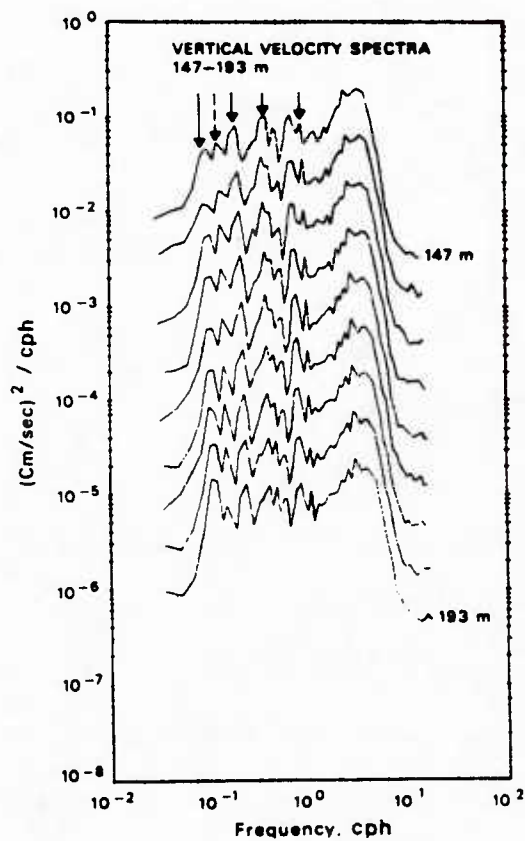


figure 4-5 Vertical velocity spectra (from Pinkel, 1981). The scale for the uppermost spectrum is correct. Subsequent spectra are displaced by -5 dB. Solid arrows indicate the frequencies of the M2 tide and its first three harmonics. The dashed arrow marks the sum of inertial and tidal frequencies.

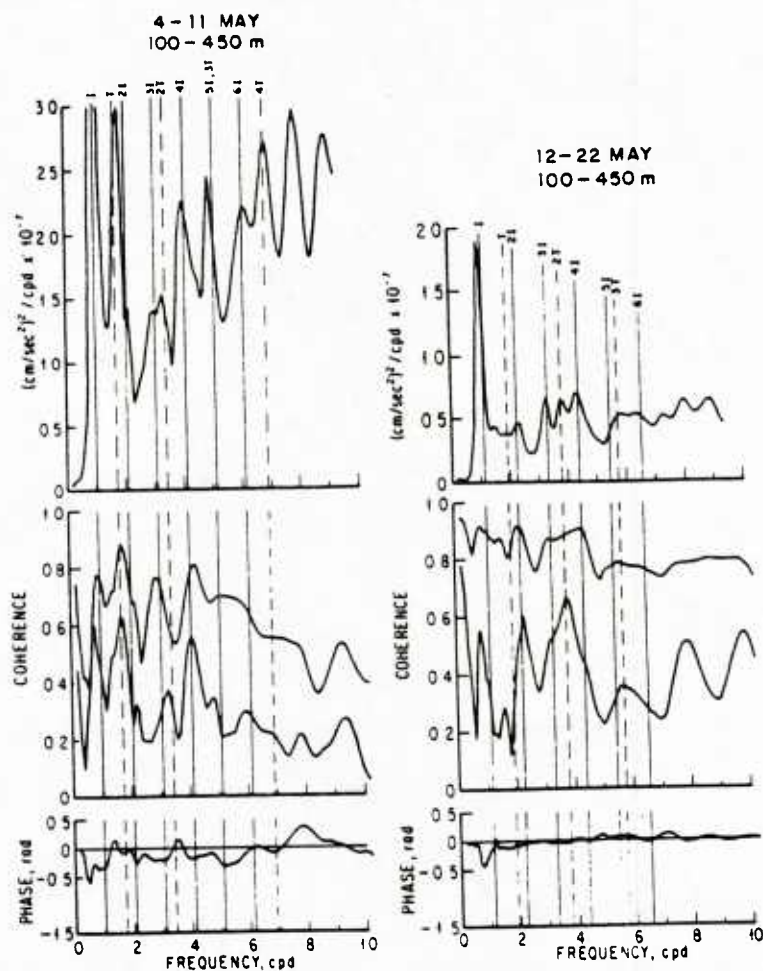


figure 4-6 Depth-averaged clockwise slant-acceleration spectra, slant coherence and phase, 100-450 m average (from Pinkel, 1983). Note that the larger inertial peak in the 4-11 May data has been truncated. It actually reaches a value of $9 \times 10^{-4} (cm/s^2)^2 / cpd$. Coherences are plotted for slant separations of 20 and 40 m in the 4-11 May data, 15 and 45 m for the 12-22 May data. Coherence values at the smaller of these separations are slightly overestimated. This results from the finite length of the acoustic pulse, which averages over 30-40 m in space.

sensor response to a sinusoidal vertical displacement. As a simple example, consider $\eta(T_o, t) = z(T_o) - z_o$ the vertical displacement of an isotherm of temperature T_o about mean depth z_o . The vertical displacement measured at the fixed depth z_o is not $\eta(T_o, t)$, but is given by:

$$\eta(T_o, t) = \eta(z_o, t) + \frac{\partial \eta}{\partial z} \Big|_{z_o} (z(T_o) - z_o) + \dots \quad (4-1)$$

but

$$z(T_o) - z_o = \eta(T_o, t)$$

so

$$\eta(z_o, t) = \eta(T_o, t) \left(1 - \frac{\partial \eta}{\partial z} \Big|_{z_o}\right) + \dots$$

Hence there is a non linear response by a fixed depth sensor. Desaubies and Gregg refer to this as fine structure contamination resulting from internal wave straining.

The repeated profiling CTD data is of interest in that it can be analyzed in a variety of different ways, each of which responds differently to potential sources of nonlinearity in the measurements. Temperature time series at fixed depths can be calculated. These are analogous to conventional moored measurements. They are sensitive to contamination by both the background gradient and by internal wave straining. Alternatively, a technique exists for calculating fixed depth time series of vertical velocity. These are not sensitive to contamination by the background temperature gradient but are influenced by internal wave straining. Finally, time series of isotherm displacement can be produced. These are unaffected by both forms of contamination. If power spectra of isotherm displacement series are smooth and continuous while those of the fixed depth time series show harmonic structures, it might be argued that the previously reported harmonics are unimportant artifacts of the measurement technique. On the other hand, if the harmonics appear most strongly in the "uncontaminated" data, their role in the dynamics of the wavefield must be

addressed. It might be that fine structure contamination has served to obscure a simple and obvious harmonic structure in the internal wave spectrum.

A sequence of 220 temperature profiles is presented in Fig. 2-3 and illustrates the nature of the data. When using repeated profiling data, internal wave spectra are usually produced from time series analysis of isotherm (isopycnal) displacement records. In some sense this can be considered a semi-Lagrangian measurement, as the vertical displacement of a surface is being tracked. A set of 140 isotherms is presented in Fig. 4-7 spanning a period of 24 hours. Isotherms are separated by 0.1°C in temperature. Thus, regions of closely spaced isotherms, such as 100 - 175m, are regions of high temperature gradient. The mixed layer, down to 90m, is indicated by a relative absence of isotherms. A diurnal mixed layer is seen to form in the first 8 hours of the record. Vertical displacement of the isotherms results primarily from internal wave motions. The high frequency (several cycles per hour) motions are seen to be remarkably coherent with depth. High frequency disturbances can be seen extending through 200 - 300m in the vertical with no apparent change in phase. The decay of the highest frequency motions with depth is also seen. Internal waves are confined to that region of the water column in which their frequency is less than the Vaisala frequency. The measurement interval (0 - 400m) spans the waveguide completely for the highest frequency waves. The lower frequency motions are considerably more energetic and far less coherent in depth.

With traditional moored measurements, time series of temperature/current at fixed depth are the starting point for subsequent spectral analysis. Fig. 4-8 illustrates this purely Eulerian measurement for the same period of time covered in Fig. 4-7. Here, time series of temperature at fixed depths ranging from 70-400 m and separated by 6 m vertically are shown. The motions are strikingly less sinusoidal than those in Fig. 4-7. The difference is ascribed to fine structure contamination.

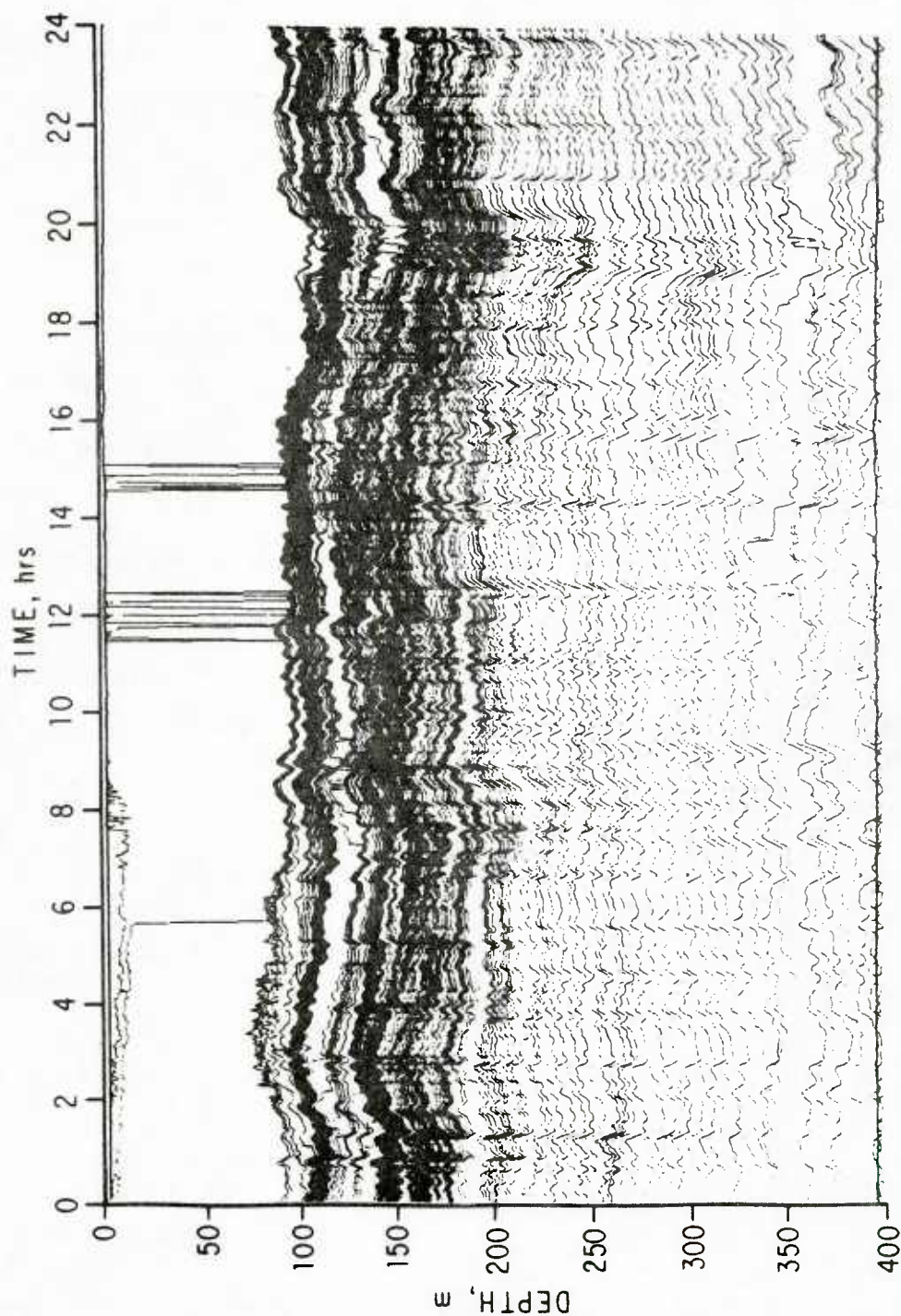


figure 4-7 A set of 140 isotherms covering the period noon 19 May 1980 to noon 20 May 1980. Isotherms are separated by 0.1°C in temperature. The vertical coherence of the high frequency internal waves is pronounced. Note that the highest frequency waves are confined to region of high Vaisala frequency, between 100 and 200 m. Deep records resemble low pass filtered versions of their shallower counterparts.

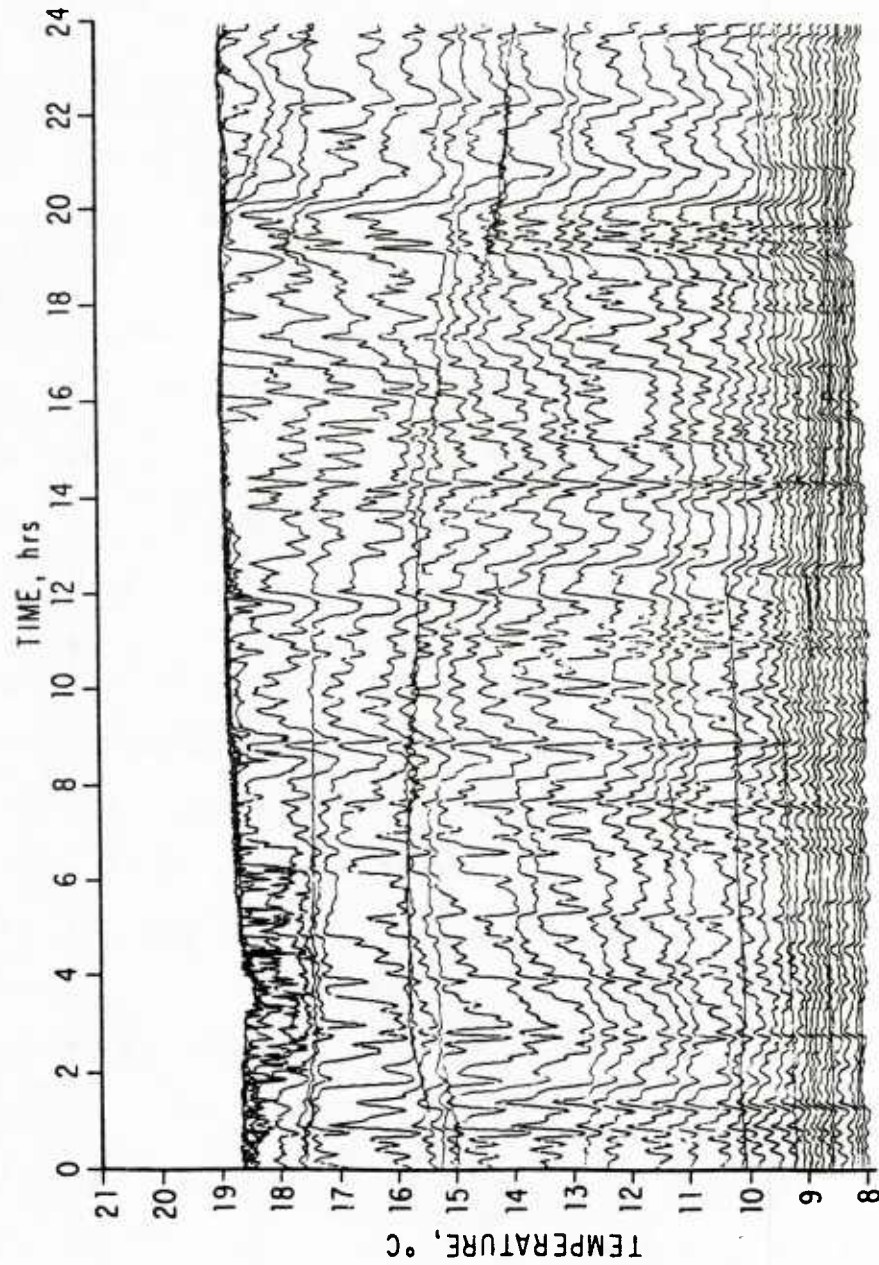


figure 4-8 Time series of temperature at fixed depths from 70-400 m, separated by 6 m vertically. The period covered is noon 19 May 1980 to noon 20 May 1980. The nearly horizontal lines through the figure correspond to quasi isothermal layers advecting under FLIP. The depth of the layer is altered by internal wave motions, but the temperature is not.

In previous studies (Pinkel, 1981), a method of analysis has been used to produce fixed depth Eulerian measurements which are not contaminated by the mean background temperature gradient. At each depth of interest, the temperature measured on a given profile is recorded. On the subsequent profile the new depth at which the temperature is encountered is determined. From the depth difference which has occurred during the interval between profiles, the mean vertical velocity at the depth of interest can be inferred. In contrast to the isotherm following approach, a new set of reference temperatures is then calculated at the depths of interest. These are tracked in the following profile. The result is a set of vertical velocity time series which are calculated at (near) fixed depths yet are not fine structure contaminated. These data differ from the isotherm displacement series by the non linear wave straining term, $\eta \partial \eta / \partial z$

4.4 Spectral Analysis

It remains to form the power spectra of the semi- Lagrangian (isotherm), uncontaminated Eulerian (fixed depth vertical velocity), and contaminated Eulerian (fixed depth temperature) series. The spectra can be compared and the presence or absence of harmonic peaks can be determined. It was decided to make the comparison in the different depth intervals 140 - 170m, 200 - 230m, and 260 - 290m. It would be desirable to extend this study to shallower depths. However, lateral intrusions significantly altered the temperature field during several portions of the cruise at depths above 120 m.

Time series were produced at sixteen equally spaced depths within each interval for the two Eulerian methods. In the semi-Lagrangian calculation isotherms are equally spaced in temperature and not depth. This leads to unequal numbers of isotherms being produced in each depth interval, i.e., 16 (140-170 m), 10 (200-230 m) and 7

(260-290 m). To aid in the comparison of the spectra, the isotherm displacement series were converted to an equivalent time series of vertical velocity by first differencing in time. The fixed depth temperature time series was also converted to an effective vertical velocity series by first differencing in time and then dividing by a constant mean temperature gradient.

A sequence of 10240 temperature profiles, stretching over 16 days, was used to produce the time series. This was broken into nine 2048 drop 50% overlapping sub-series. Each sub series was multiplied by a Hamming window and Fourier transformed. The resulting spectral estimates from all sub series in each depth range were averaged together to improve the statistical stability of the spectral estimates. The amount of statistical improvement resulting from the depth averaging is uncertain. The wavefield is highly coherent over 30 m in the vertical (Briscoe, 1975; Pinkel, 1975). The adjacent time series in each depth range are certainly not independent realizations of the same random process. Nevertheless, some noticeable smoothing of the data was achieved by the depth averaging. Further smoothing was achieved by cross frequency averaging of the spectral estimates. The resulting power spectra are presented in Figures 4-9, 4-10, and 4-11. Two sets of confidence limits are presented in Figure 4-9. The outer set reflects the pessimistic point of view that the vertical averaging did nothing to improve the statistical stability of the estimate. This is clearly the proper viewpoint for the high frequency motions, which are so coherent in depth. The inner set assumes the converse, giving the confidence intervals as if the series averaged in the vertical were actually independent. These limits are more appropriate for lower frequency, less coherent motions. The issue of statistical stability is somewhat beside the point in this discussion. The presence of spectral harmonics suggests that motions in different frequency bands are not independent.

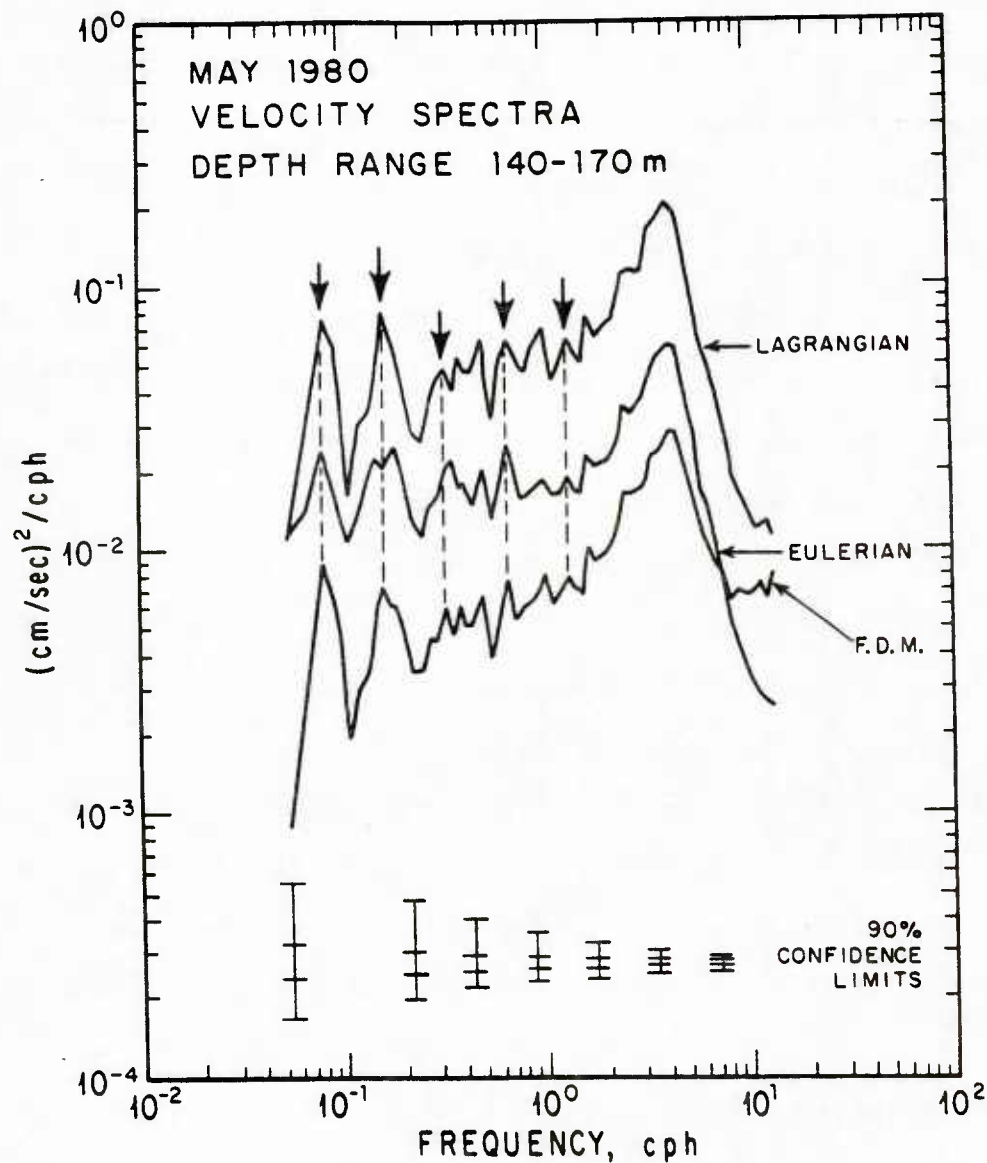


figure 4-9 Power spectra of vertical velocity as estimated from isotherm following (Lagrangian), fixed depth velocity (Eulerian) and fixed depth temperature (F.D.M.) time series. The scale is appropriate to the topmost spectrum. The others are successively offset by -5 dB increments. The 90% confidence limits are presented for the two limiting interpretations of the analysis discussed in the text. The two large low frequency peaks are the baroclinic semi-diurnal tide and its first harmonic. Arrows indicate 1, 2, 4, 8 and 16 times the tidal frequency.

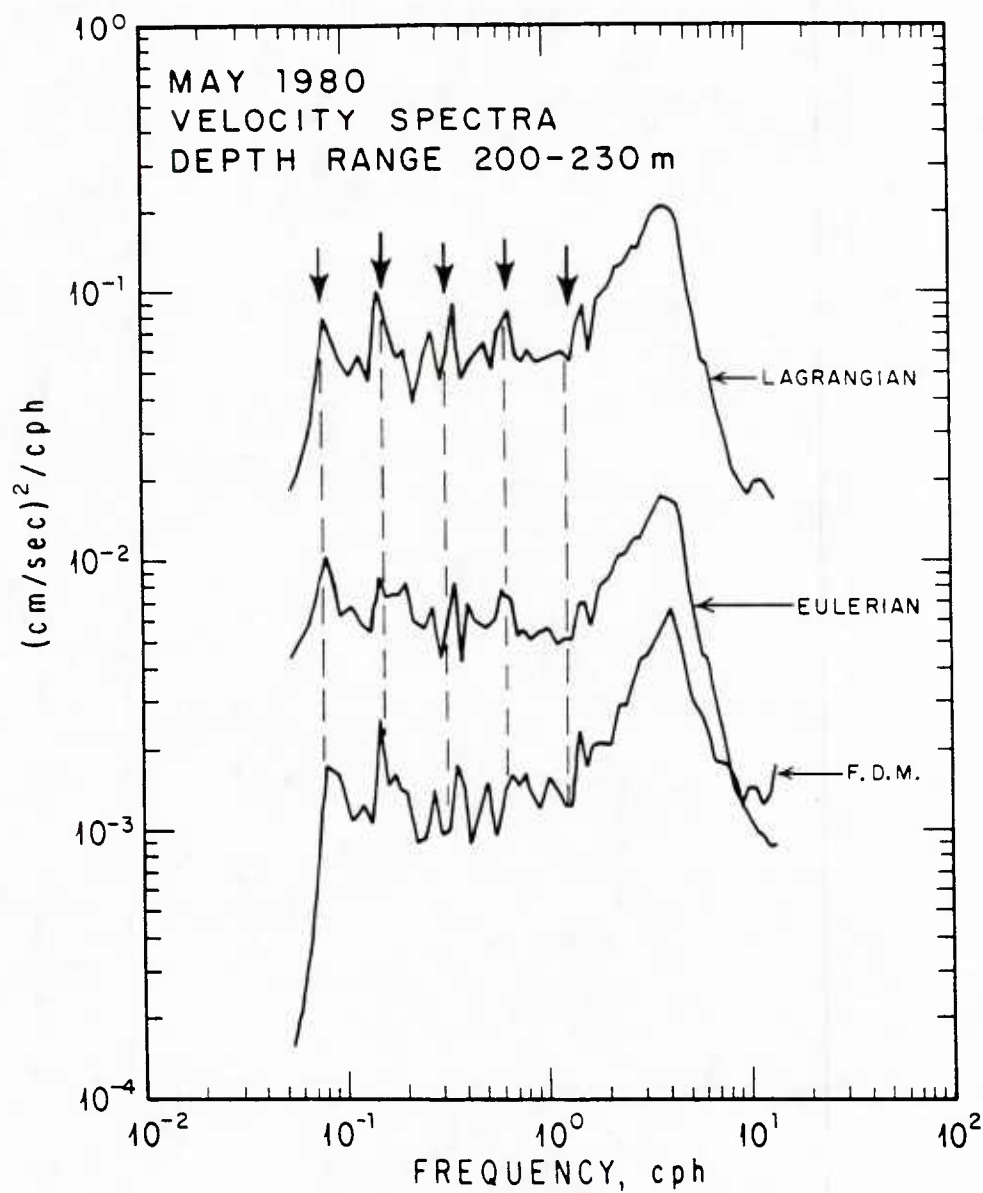


figure 4-10 Power spectra of vertical velocity as estimated in figure 4-9. The scale is appropriate to the topmost spectrum. The others are successively offset by -10 dB increments. Reference arrows indicate 1, 2, 4, 8 and 16 times the tidal frequency.

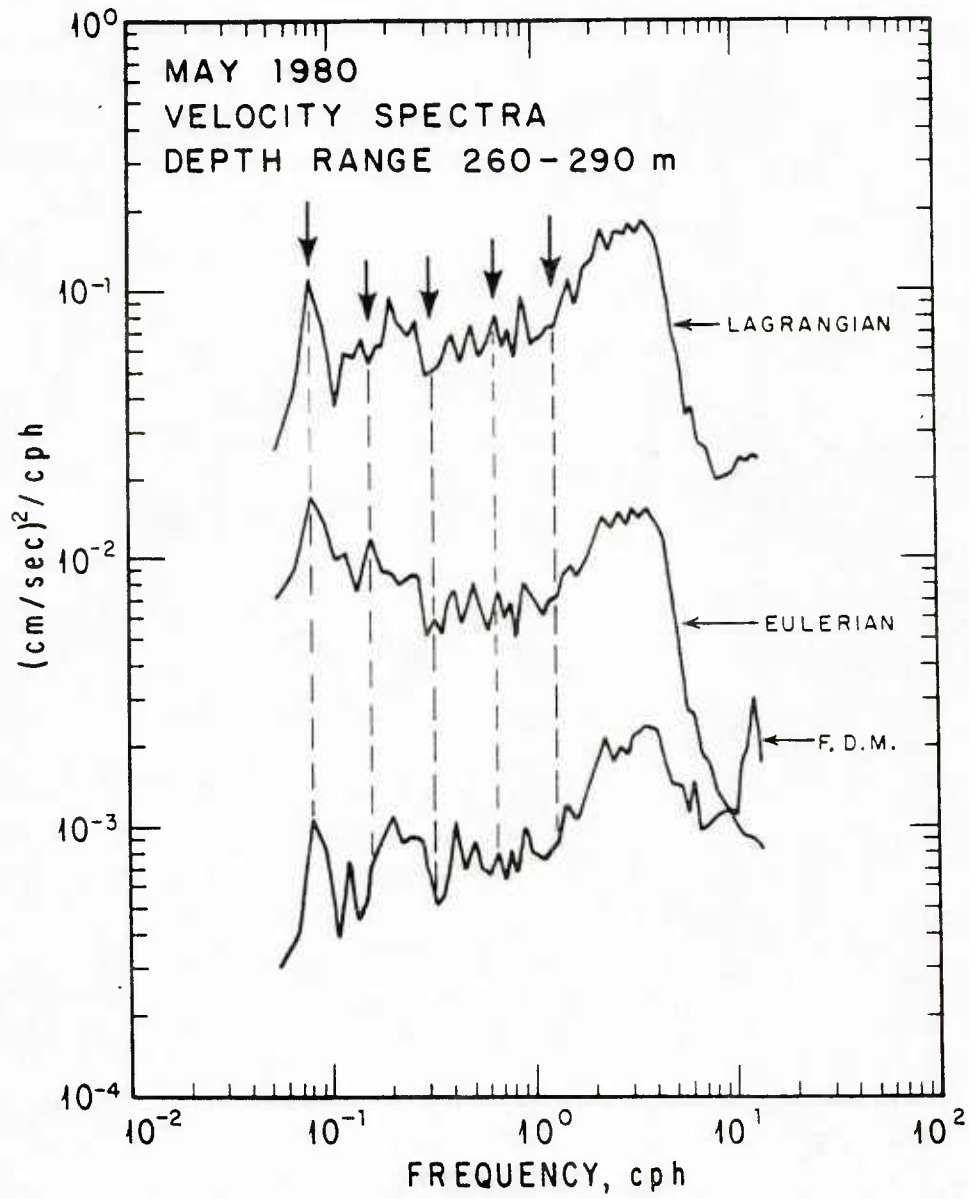


figure 4-11 Power spectra of vertical velocity, as estimated in figure 4-9. The scale is appropriate to the topmost spectrum. The others are successively offset by -10 dB. Reference arrows indicate 1, 2, 4, 8 and 16 times the tidal frequency.

The variance in the spectra is seen to be confined between the inertial (0.04 cph) and local Vaisala frequencies. The total variance increases slightly with depth, in accordance with linear theory. The Vaisala cutoff is preceded by a pre-cutoff peak. Most of the vertical velocity variance in the upper ocean occurs in this peak. The Vaisala cutoff is least apparent in the Fixed Depth Mooring Spectra, due to fine-structure contamination. The peak at the low frequency end of the spectra is the semi-diurnal baroclinic tide. The adjacent peak is the first harmonic of the tide. In the upper two depths, Figures 4-9, 4-10, this has vertical velocity variance comparable with the tide itself.

Discussion

It is clear from Figures 4-9 to 4-11 that the three different analysis methods yield spectra that are equally irregular at low frequency peaks. There are no significant peaks in the Eulerian or Fixed Depth Mooring Spectra which are absent in the Lagrangian spectra. Arrows and dashed reference lines indicate the position of the semi-diurnal tide and some of its even harmonics. These appear to fall on spectral peaks in the upper two depth intervals, but not the deepest. In all spectra there are peaks which occur between the harmonic lines which are of the same order as those which fall on the lines. These might be odd harmonics of the tide, harmonics of near inertial motions which themselves do not appear in these spectra, or perhaps inter-modulation products of the inertial and semi-diurnal tidal motions.

The original concern is that the harmonics identifiable in the Eulerian or Fixed Depth Mooring spectra resulted from internal wave straining or fine structure contamination. This is not supported by the data. The Lagrangian spectra show the harmonic structures perhaps the clearest of any.

CHAPTER 5

FORCED VERSUS FREE WAVES

5.1 Introduction

In Chapter 4 evidence is presented which is consistent with the view that contamination effects alone are not strong enough to account for the observed harmonics in internal wave spectra. It is appropriate at this point to consider dynamic explanations for the harmonics. Two possible explanations are forwarded which are not mutually exclusive. The first of these assumes that the harmonics are *locally* forced (locally interacting) in the water column. These harmonics will be in fixed phase relative to the fundamental and are referred to as forced waves. The second explanation assumes that the waves at the harmonic frequencies are generated at remote locations and propagate to the site independently from the fundamental. These harmonics will have random phase relative to the fundamental at the observation site, and are referred to as free waves. Mechanisms which lead to both *locally* forced and free waves are reviewed.

The issue is to distinguish which of these two proposed mechanisms is more appropriate for describing the observations. Bispectral analysis is a mathematical and computational technique which can help answer this question. The 1983 isopycnals are analyzed with this technique and the results discussed.

5.2 Mechanisms

Some of the first observations of non-sinusoidal internal waves in the ocean were made by Lafond (1966). Fig. 5-1 is taken from this paper and shows the shape of finite amplitude internal waves calculated from temperature data collected at the Naval Electronics Laboratory Tower off Mission Beach, California. Notice how the

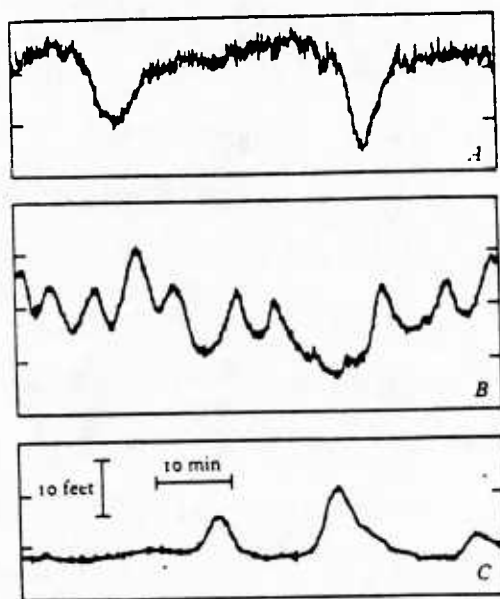


figure 5-1 Smoothed records of the shape of internal waves (A) near the sea surface, (B) at an intermediate depth and (C) near the sea floor. (From LaFond, 1966. In Encyclopedia of Oceanography, ed., R. W. Fairbridge).

shape of the waves changes with depth: they peak downwards at the surface and upwards near the seafloor while at mid-depths they tend to a shape which is more symmetrical about the horizontal and more sinusoidal. Lafond notes that the shape of the waves at different depths depends upon the depth of the thermocline, indicating that stratification plays a key role in determining the shape of the waves. These observations are in agreement with laboratory studies that show the shapes near the surface commonly appear to be like inverted trochoids with broad crests and narrow troughs while near the bottom the trend is reversed and the crest, like those of surface waves, are narrower than the troughs.

In 1968, Thorpe published a comprehensive study on the shape of finite amplitude progressive internal waves in a stratified fluid. He presents a review of previous work on two layer systems as well as a theory for the continuously stratified case. The two layer case which is most relevant to the deep ocean is that of a shallow layer overlying a deeper denser layer. Here the equation for wave displacement shows that the wave is more sharply peaked on the side pointing into the deeper layer.

Thorpe's derivation for the shape of the wave profile in the continuously stratified case uses similar expansion techniques to those employed by Stoke's in the derivation of the shape of surface waves in deep water. In the latter case the non-linearity comes from the surface boundary conditions whereas, in Thorpe's model, it is embodied in the two dimensional vorticity equation expressed in terms of the stream function. Second order corrections for the stream function are obtained which are forced by the second derivative of density ($\partial^2\rho/\partial z^2$). These can be expanded in terms of eigenfunctions of the homogeneous equation. Using the continuity equation, a second order equation is then derived for the wave profile. Thorpe derives some wave forms using standard density profiles. Fig. 5-2 shows the shape of a mode 1 wave profile to second order in a "tanh" density profile with boundary conditions of zero

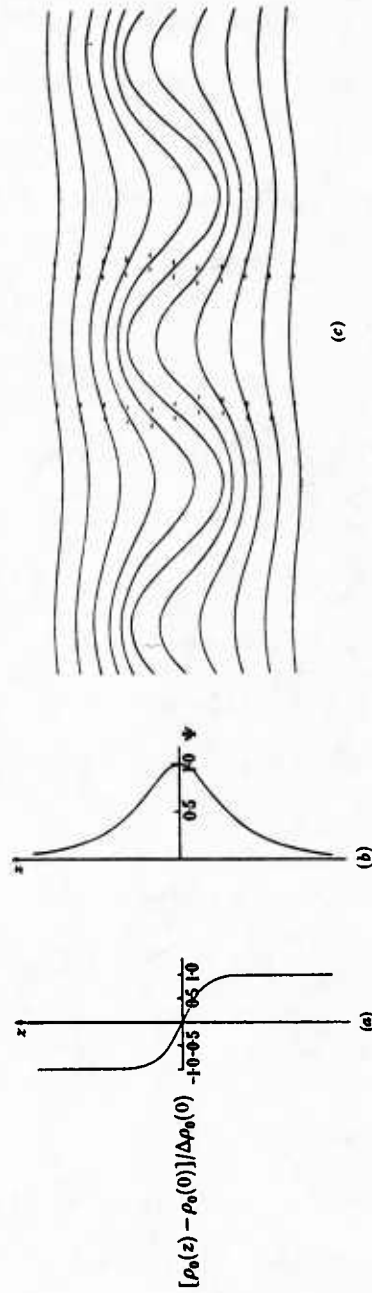


figure 5-2 Waves of the first mode ($m = 1$) in a fluid with density $\rho_0(z) = \rho_0(0)(1 - \Delta \tanh az)$. (a) The distribution of ψ . (b) The wave shape with $ak^2/\sigma = \pi/3$, $k/a = 1/2$ and $f_3(z) \equiv 0$ (see 3.3.21). The short horizontal lines mark the levels from which the lines of constant density are disturbed (from Thorpe, 1968).

vertical velocity at the top and bottom boundaries. This type of density structure is similar to that found near the pycnocline in the ocean. At the level where $\partial^2\rho/\partial z^2 = 0$, the forcing for the second order stream function is zero and, hence, a sinusoidal wave shape is predicted. Above and below this level $\partial^2\rho/\partial z^2$ is non-zero but with opposite sign. The corresponding forcing leads to nonlinear waves whose shapes are horizontally symmetric about the level at which $\partial^2\rho/\partial z^2 = 0$. Fig. 5-3 shows the shape of a mode 1 wave profile in a linear density profile. This type of density structure is similar to that found beneath the pycnocline in the ocean. Although $\partial^2\rho/\partial z^2 = 0$ and the second order stream function is zero, the second order density correction is, in general, non-zero and non-sinusoidal shapes are again predicted.

Besides stratification, background shear is also known to have a nonlinear effect on the shape of internal waves. Again Thorpe has done much of the theoretical and laboratory work to document its effects. For example, in Thorpe (1978), the case where both the Vaisala frequency and shear are concentrated in a narrow transition layer is examined (Fig. 5-4). When there is positive shear* the waves have narrow crests and flat troughs like surface waves, but when there is negative shear the waves have flat crests and narrow troughs.

The effects of stratification and shear, as discussed above, lead to *locally* forced waves. The essential feature which distinguishes these from free waves at the same frequencies is that they are phase locked to the fundamental. Free waves, on the other hand, will have random phase. If we now assume that the observed harmonics are due entirely to free waves, we still require a mechanism which accounts for the increased levels of variance at these frequencies. Resonant interaction is a candidate since it can produce waves at such sum frequencies. The product waves, which can

* Positive refers to positive values of $\underline{c} \cdot (\underline{g} \times \text{curl } \underline{u})$ where \underline{c} , \underline{g} and \underline{u} are vectors of phase velocity, gravity and ambient velocity.

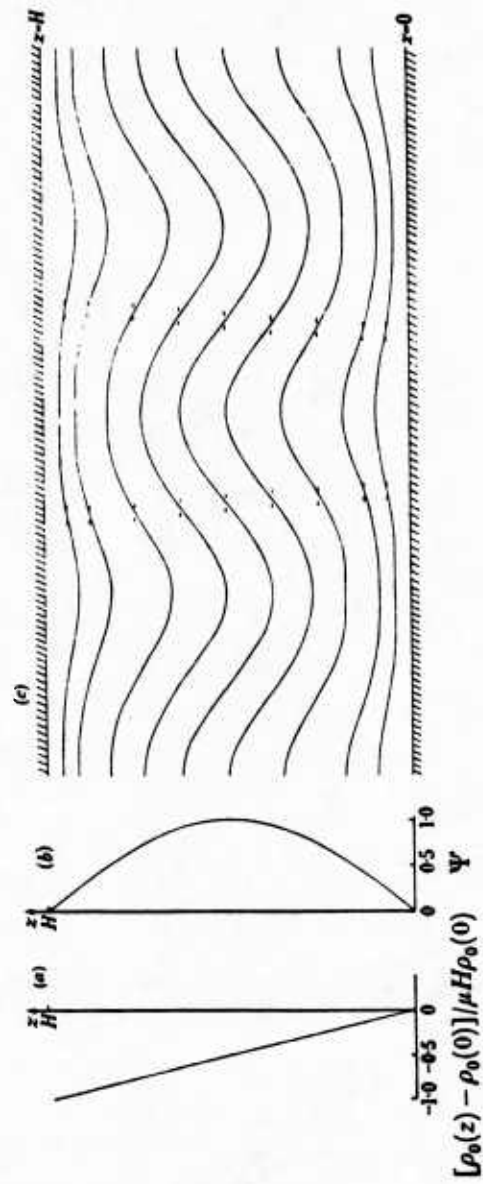


figure 5-3 Waves of the first mode ($n=1$) in a fluid density $\rho_0(z) = \rho_0(0)(1 - \mu z)$. (a) The density distribution. (b) The distribution of Ψ . (c) The wave profile with $A/H = 0.125$, $kh = 2\pi$ and $f_3(z) = 0$ (see 3.3.4). The short horizontal lines mark the levels from which the lines of constant density are disturbed (from Thorpe, 1968).

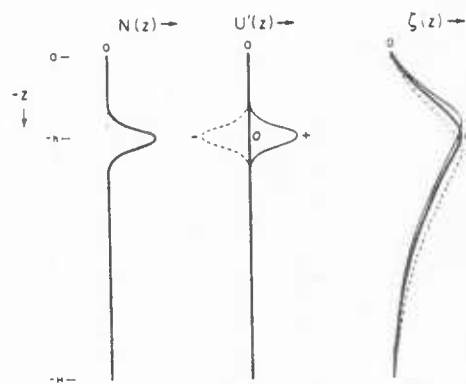


figure 5.4 First mode vertical displacements in a flow where U' and N are confined to a narrow transition layer (from Munk, 1981).

exist independently from their parents since they satisfy their own dispersion relations, will fall out of phase with them as they propagate through the ocean. If we assume that the sources for such waves are widespread, the resultant phase between the fundamental and a harmonic at any particular location will be a random function of time. For internal waves of tidal period, Rattray et al (1969) consider resonant interaction as unimportant in the open ocean, except where horizontal velocities are constrained to a narrow pycnocline region. Thus, if this mechanism is important, we expect to observe its effects in the thermocline.

Blackford (1978) proposes an interesting mechanism for the generation of the first harmonic of the semi-diurnal tide at a sill. Essentially the mechanism depends upon the Venturi effect. The tidal currents passing over the edge of a sill attain their extrema *twice* every tidal period. The corresponding changes in pressure generate an internal wave at twice the tidal frequency. This wave will propagate away from the sill as a free wave. This model could be extended to include generation at seamounts and continental slopes.

Both forced and free waves can manifest themselves as harmonics of the fundamental in internal wave spectra. At issue is which mechanism is more appropriate for describing the observations. The essential question is whether there is phase locking between the harmonic and the fundamental. In theoretical studies this determination can often be made by merely observing the waveform of an isolated wave in a given background. In the ocean many wave groups are present in the same volume of water at the same time. Simple observations of the waveform are not sensitive tests for non linearity. Instead, more sophisticated techniques such as bispectral analysis must be used.

5.3 Bispectral Analysis

Bispectral analysis is used in several branches of physics to determine if the modes in a system are interacting quadratically to produce components at sum and difference frequencies. It is thus a suitable technique for studying interactions between oceanic internal waves which are, for the most part, quadratic.

The bispectrum of a real, stationary process, $x(t)$, with zero mean is defined as:

$$B(k, l) = E[X_k X_l X_{k+l}^*] \quad (5-1)$$

where $E[\]$ is the "expected value" operator and

$$X_k = \lim_{T \rightarrow \infty} \int_{-T/2}^{T/2} x(t) e^{-i\omega_k t} dt \quad (5-2)$$

where $X_{-k} = X_k^*$, $\omega_k = 2\pi k/T$, and T is the record length of $x(t)$. It can be shown that the bispectrum satisfies the following symmetry relations:

$$\begin{aligned} B(k, l) &= B(l, k) = B^*(-k, -l) \\ B(k, l) &= B(-k - l, l) = B(k, -k - l) . \end{aligned} \quad (5-3)$$

To illustrate the use of the bispectrum, consider two waves in a system with frequencies ω_k and ω_l which interact quadratically to produce a third wave at the sum frequency ω_{k+l} . The bispectral component of interest, $B(k, l)$, will, as a result of this coupling, be non-zero.

Hasselmann et al (1963) were the first to apply the technique successfully to oceanographic wave data. They demonstrate that harmonics observed in surface wave height spectra are due to quadratic interactions of the type predicted theoretically. For data they use time series of effective wave height (bottom pressure) in 11 m depth. Here theory predicts non-linear mechanisms to be important in causing the waves to peak. They find that the real part of the bispectrum (co-bispectrum) contains the majority of the information about the interactions. This observation indi-

cates that at this depth the waves are nearly vertically symmetric like Stoke's waves. In a more recent paper (Elgar and Guza, 1985) bispectra of surface waves in much shallower water ($\sim 2\text{m}$) show much larger contributions to the quadrature bispectrum. Their findings are in agreement with theory, which predicts sawtooth wave profiles in very shallow water and biphasic values of $-\pi/2$.

Neshyba and Sobey (1975) were the first to use bispectral analysis in the study of internal waves. Their time series are of vertical displacement inferred from temperature profiles collected under the Arctic ice-cap. They interpret their bispectra in terms of weak non-linear resonant interaction theory. McComas and Briscoe (1980) discount their conclusions. They investigate the bispectrum that is obtained after perturbing a model Garrett and Munk wavenumber-frequency spectrum and find that unrealistically large amounts of data would be required to verify, in a statistical sense, that weak nonlinear resonant interactions are occurring.

In general, the bispectrum is a complex valued function possessing real and imaginary parts. An alternative and sometimes very useful representation is in terms of the bicoherence and biphasic defined respectively as:

$$b^2(k,l) = \frac{|B(k,l)|^2}{E[|X_k X_l|^2] E[|X_{k+l}|^2]} \quad (5-4)$$

and

$$\phi(k,l) = \tan^{-1} \left\{ \frac{\text{Im}[B(k,l)]}{\text{Re}[B(k,l)]} \right\} \quad (5-5)$$

The bicoherence, $b(k,l)$, is bounded by $0 \leq b \leq 1$. The bicoherence and biphasic have several important applications which are discussed below and used in the analysis of the 1983 isopycnals.

With finite amounts of data, it is necessary to estimate the confidence limits

on any statistical quantities calculated. There are no generally agreed upon confidence limits for bispectral estimates. However, there is an alternative approach for assessing their statistical significance which involves the bicoherence. Haubrich (1965) calculates the 95% confidence interval on zero bicoherence for a Gaussian (linear) process. He finds it equal to $4/\nu$, where ν is the number of degrees of freedom. ν is defined as twice the number of independent realizations (records) from which the bispectral estimates are calculated. When a bicoherence estimate exceeds the 95% value, we have confidence that the corresponding bispectral estimate is not due to random noise present in a Gaussian process.

For limited amounts of data the bicoherence spectrum, since it is normalized, is the most suitable statistic for determining whether certain modes in a system are the result of quadratic coupling (forced) or not (free). Kim and Powers (1979) illustrate this use of bicoherence. Fig. 5-5 is taken from their paper and illustrates some of the relevant results. In Fig. 5-5(a) the peak at frequency d corresponds to a wave whose phase is the sum of the phases at frequencies b and c . This case is analogous to a quadratically coupled system. Accordingly, we see that the bicoherence at (b, c) is 1. On the other hand, in Fig. 5-5(b) the spectrum and bicoherence correspond to a system which is not quadratically coupled. The phase at frequency d is random with respect to the phases at frequencies b and c . The resulting bicoherence at (b, c) is thus negligible.

The bicoherence is also helpful in determining the proportion of the variance at a given frequency which is the result of quadratic interaction. For example, given that the waves at frequencies ω_k and ω_l are interacting to produce waves at the sum frequency ω_{k+l} , $b^2(\omega_k, \omega_l)$ is the proportion of the variance at frequency ω_{k+l} which is due to this interaction.

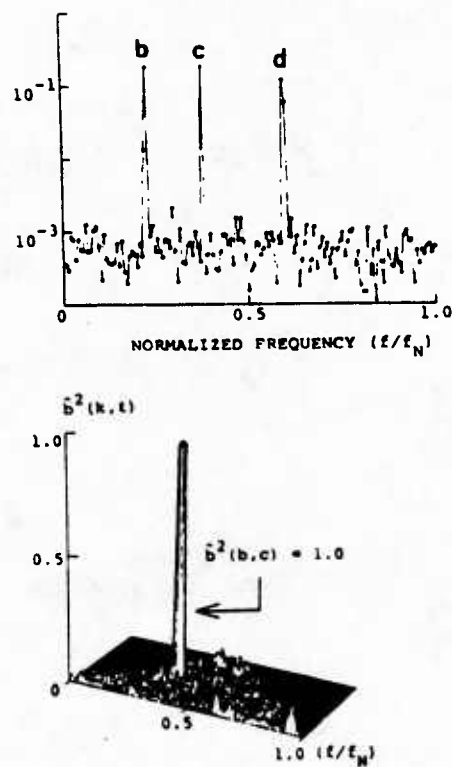


figure 5-5 a The power spectrum (top) and the squared bicoherence spectrum (bottom) of a signal which contains three waves with consistent phases ($\theta_d = \theta_b + \theta_c$) plus Gaussian background noise (from Kim and Powers, 1979).

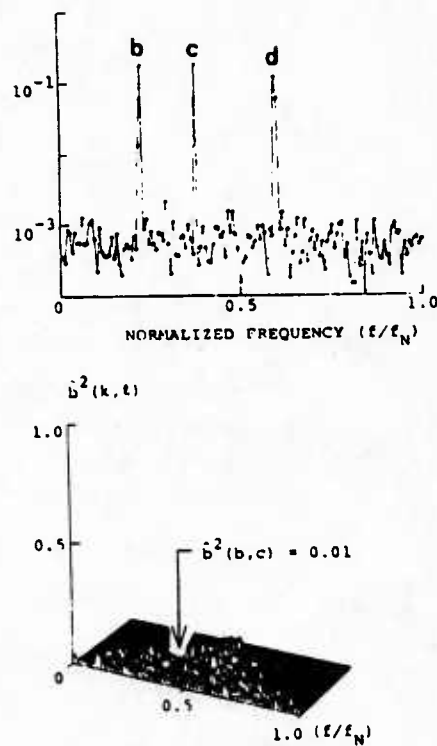


figure 5-5 b The power spectrum (top) and the squared bicoherence spectrum (bottom) of a signal which contains three waves with independent phases plus Gaussian background noise (from Kim and Powers, 1979).

The biphasic is useful for interpreting the shapes of nonlinear waves. as an example, consider a wave profile, $\eta(t)$, given by

$$\eta(t) = \cos \omega t + A \cos(2\omega t + \phi) + \dots \quad (5-6)$$

where A is a constant and ϕ in the biphasic at (ω, ω) . ϕ can take on values from $-\pi$ to $+\pi$. We observe that: (a) if $\phi < 0$ ($\phi > 0$), waves are tilted forward (backward); and (b) if $|\phi| < \pi/2$ ($|\phi| > \pi/2$), crests become sharp (flat) while troughs become flat (sharp). For Stoke's waves, the biphasic values associated with the harmonics of the fundamental are all zero. On the other hand, waves on the verge of breaking on a beach have biphasic values of $-\pi/2$ (Elgar and Guza, 1985). The theoretical models of Thorpe which investigate the forcing of harmonics in the presence of stratification or shear do not allow for biphasic values different from zero or 180° . These values (0 and 180°) correspond to non-linear internal waves which are vertically symmetric, like Stoke's waves, peaking either up or down. Biphasic values which are different from 0 or 180° can be obtained from models which allow Fourier amplitudes to be slowly varying functions of space or time. Such is the case in the model of Elgar and Guza (1985) for waves on a sloping beach. Here the biphasic evolves from a value of zero in deep water (Stoke's wave) to a value of $-\pi/2$ in shallow water (almost breaking wave).

Skewness is a statistic which is closely related to the bispectrum. It is given by:

$$S = \frac{E[x(t)^3]}{E[x(t)^2]^{3/2}} \quad (5-7)$$

where

$$E[x(t)^3] = 12 \sum_{k,l} \sum_{k>l} \text{Re}\{B(k,l)\} + 6 \sum_k \text{Re}\{B(k,k)\} \quad (5-8)$$

It is the third moment of the probability density function for the process, $x(t)$, and is a measure of how skewed the shape of this function is. Because it contains information

about the bispectrum, it is often used as a test for non-linearity. However, care must be exercised in its interpretation as it contains no information about the imaginary part of the bispectrum. For instance, a sawtooth wave which has biphasic values of $-\pi/2$ will have a bispectrum which is totally imaginary and a skewness of zero.

5.4 Data Analysis

This section describes an analysis of the 1983 isopycnals. The work is an attempt to distinguish whether spectral harmonics of the internal tide are due to free or forced waves. Included in the section is a description of the bispectral analysis of the isopycnals.

In chapter 2, Fig. 2-6, a cascade plot of σ_θ profiles covering a 24 hour period is presented. There are 6710 such profiles covering the period 29 October - 13 November 1983. The isopycnals were calculated from these profiles in the following manner. All 6710 profiles were averaged to obtain the smooth profile shown in Fig. 5-6. The 155 reference densities for the isopycnals, corresponding to depths which are equally spaced by 2 meters, were calculated from this profile. Fig. 5-7 shows the isopycnal surfaces that correspond to the profiles shown in Fig. 2-6. The flattening of the deepest isopycnals is an artifact of the programming. We see that isopycnals do not suffer from the distorting effects of lateral intrusions which isotherms do and, hence, they are a more faithful representation of the internal wave-field. Note that the most energetic motions, as expected, are due to the internal tide. Notice also the several groups of high frequency low mode waves which have been observed in many other data sets.

Time gaps ($\sim 7\%$ of the total time) in each isopycnal were filled by linear interpolation, and the resulting time series sub-divided in seven sub-sections each 1024 points long (51.2 hours). 50% overlapping and a Hamming window were applied

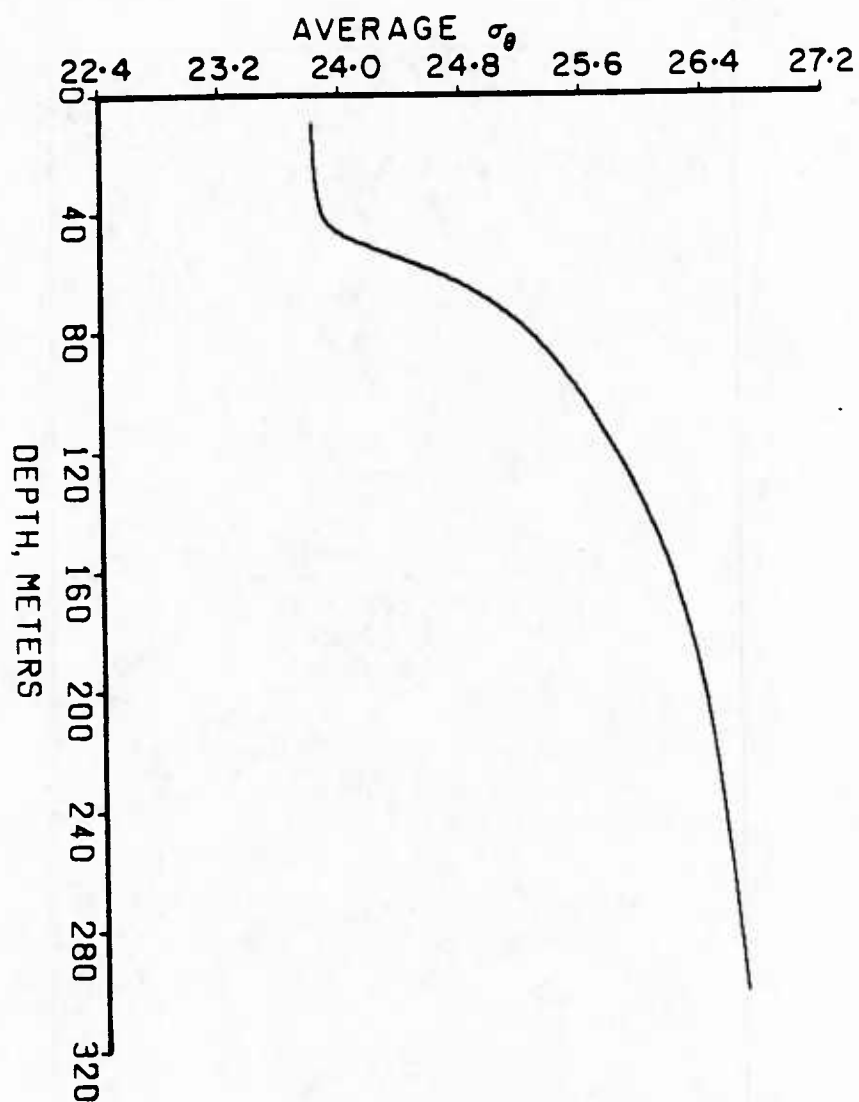


figure 5-6 Average σ_t profile for MILDEX. This average was calculated from 6710 CTD profiles collected from 29 October - 13 November, 1983.

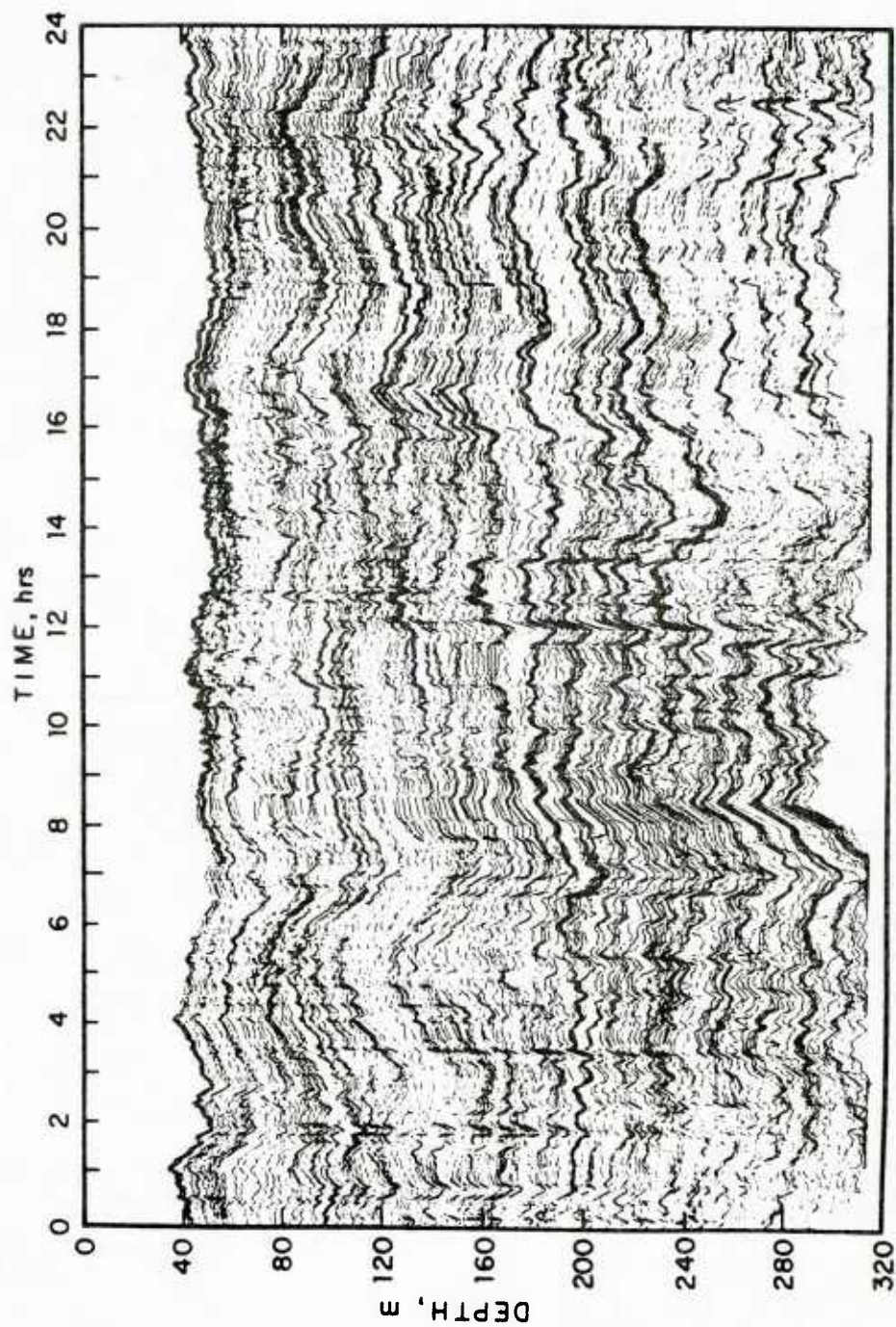


figure 5-7 The isopycnal surfaces corresponding to the σ_t profile displayed in figure 2-6. The isopycnals are separated by approximately 2 meters in depth.

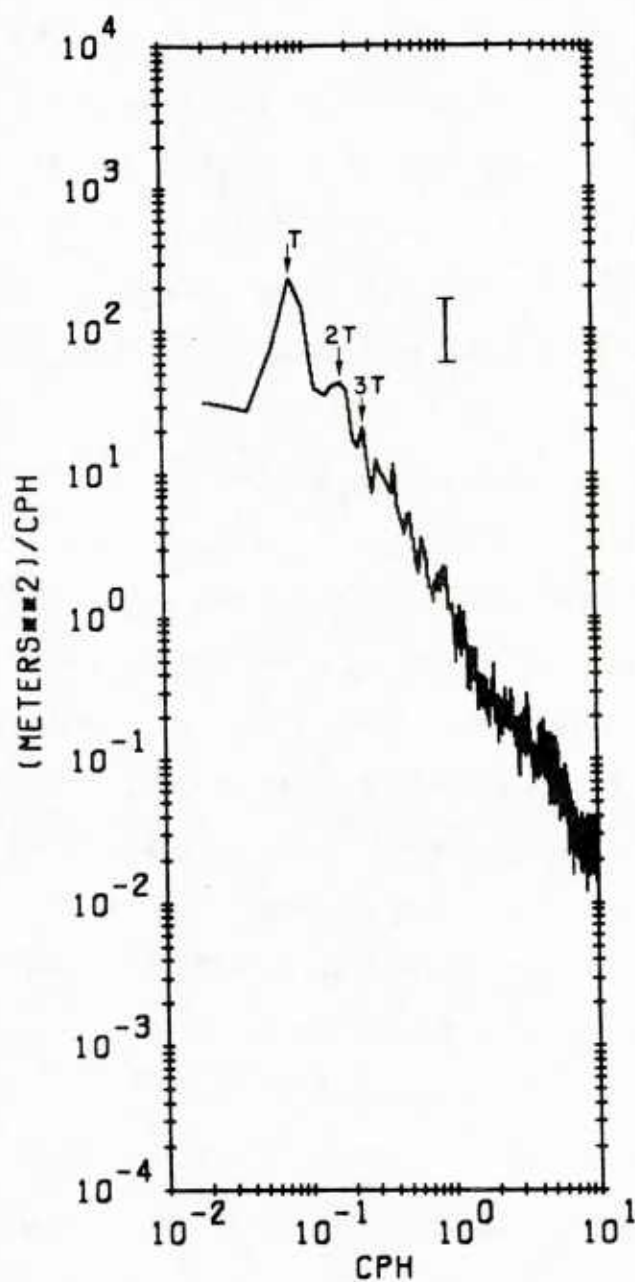


figure 5-8 Vertical displacement spectrum calculated from the isopycnal whose mean depth is 80 m. The error bar denotes the 90% confidence limits. The arrows indicate the frequencies of the internal tide and its first two harmonics.

before calculating the power spectra. As an example, the spectrum for the 80 m isopycnal is presented in Fig. 5-8. Harmonic structure is again visible as well as the familiar -2 slope and the pre-Vaisala maximum. Harmonic structure is observed in all the spectra from 40-310 m. Since the primary concern is with the internal tide and its harmonics, the high frequency information was discarded at this stage in the analysis to save on computation time. Accordingly, the isopycnals were low pass filtered below 1 cph and decimated by seven. The resulting time series are 1011 points long with a sampling interval of 21 minutes (see Fig. 5-9).

In previous studies (Pinkel, (1981), and Levine et al (1983)) the ratio of the harmonics to the internal tide is found to be greatest in the thermocline and decrease with depth. Is this behavior again the case for the 1983 isopycnals? These ratios were calculated and two of them are displayed in Fig. 5-10 together with a plot of the amplitude of the internal tide versus depth. Variances at each depth were obtained from the spectra by integrating over frequency bands 0.02 cph wide centered at 0.081, 0.162 and 0.243 cph. These spectra were formed from the FFT's of the time series shown in Fig. 5-9. Again, we see that the harmonics are relatively stronger in the thermocline suggesting that the mechanisms causing them are more effective in this region. This observation is consistent with the predictions of three generation mechanisms discussed in an earlier section. In Thorpe's model for nonlinearity due to the stratification (Thorpe, 1968), the forcing term in the second order equation for the stream function is proportional to $\partial^2 \rho / \partial z^2 \left(\sim \partial N^2 / \partial z \right)$ which has its extrema in the thermocline (see Fig. 5-11). Secondly, vertical gradients of horizontal current velocity are typically highest just beneath the mixed layer (see Fig. 5-12) suggesting that forcing due to the shear mechanism (Thorpe, 1978) should be important.

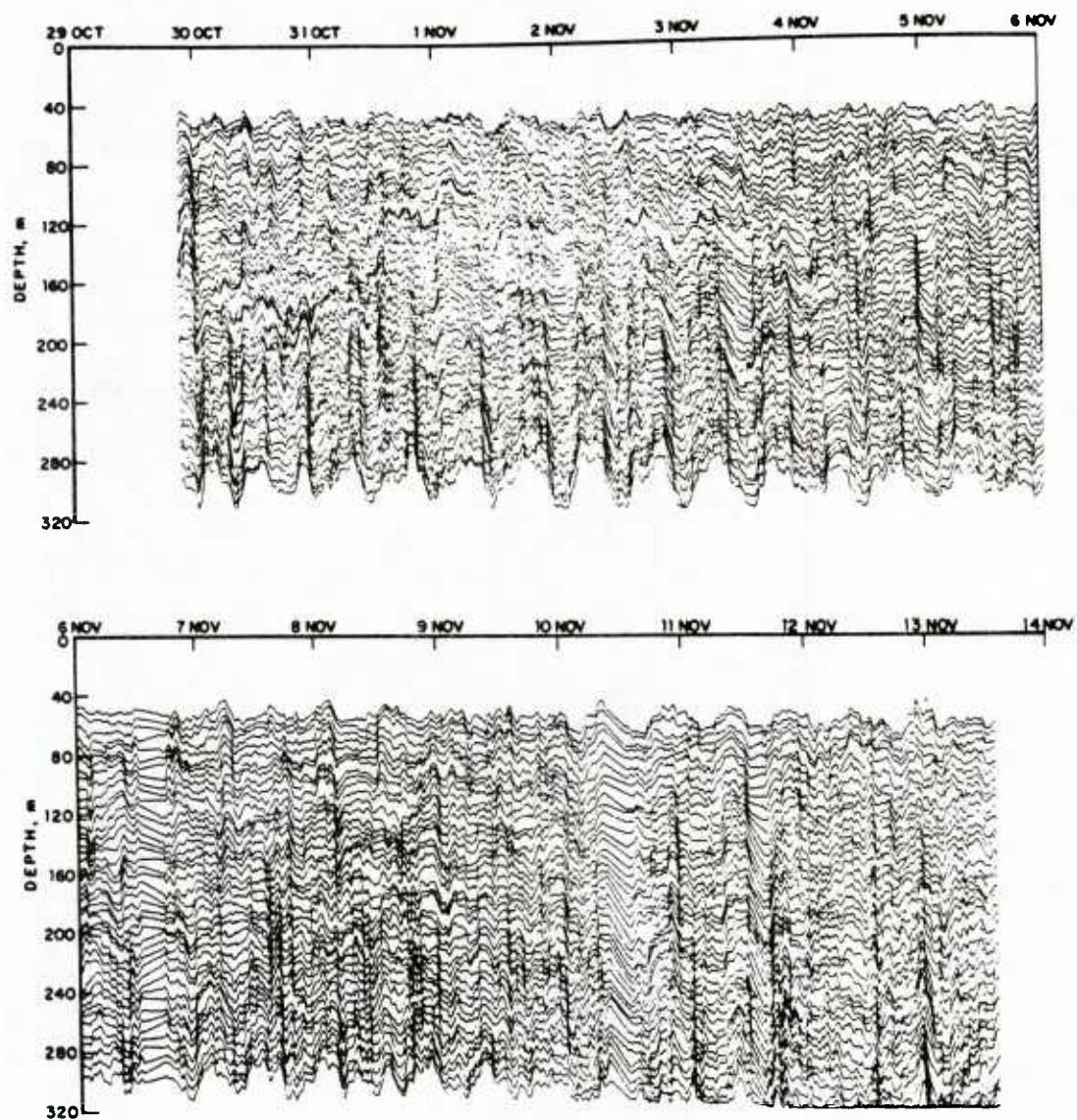


figure 5-9 A low pass filtered (< 1 cph) version of the 1983 isopycnals. Straight lines indicate time gaps.

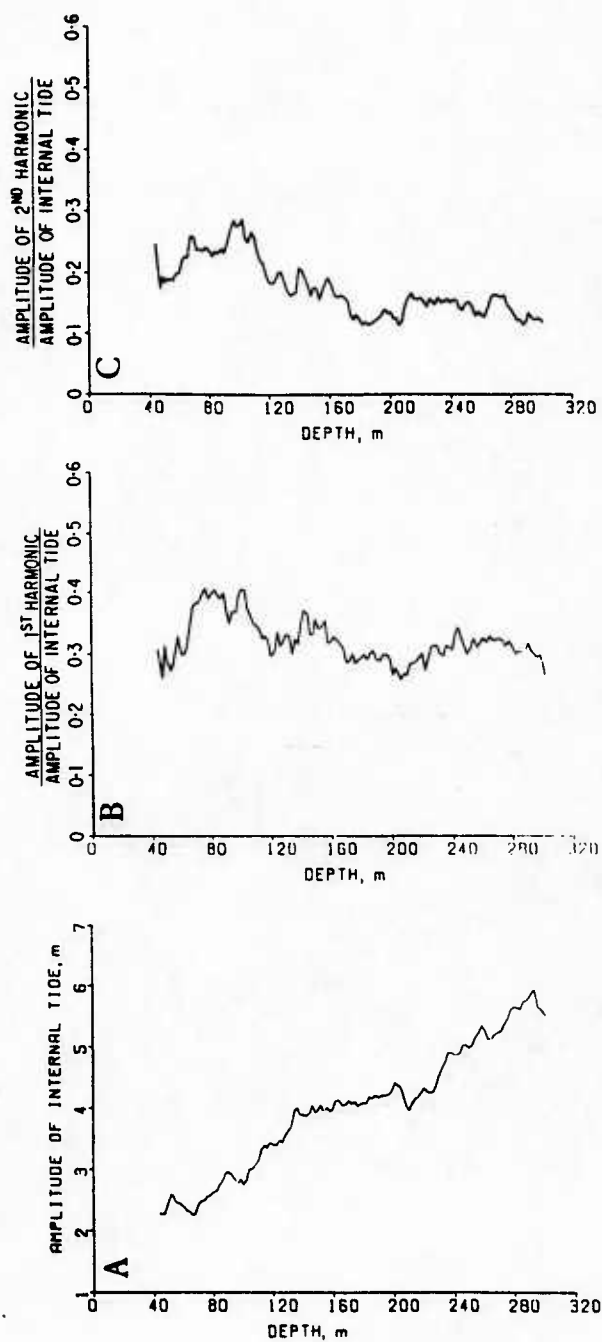


figure 5-10 A) Amplitude of the internal tide vs. depth. B) Ratio of the amplitude of the first harmonic of the internal tide to the amplitude of the internal tide vs. depth. C) Ratio of the amplitude of the second harmonic of the internal tide to the amplitude of the internal tide vs. depth.

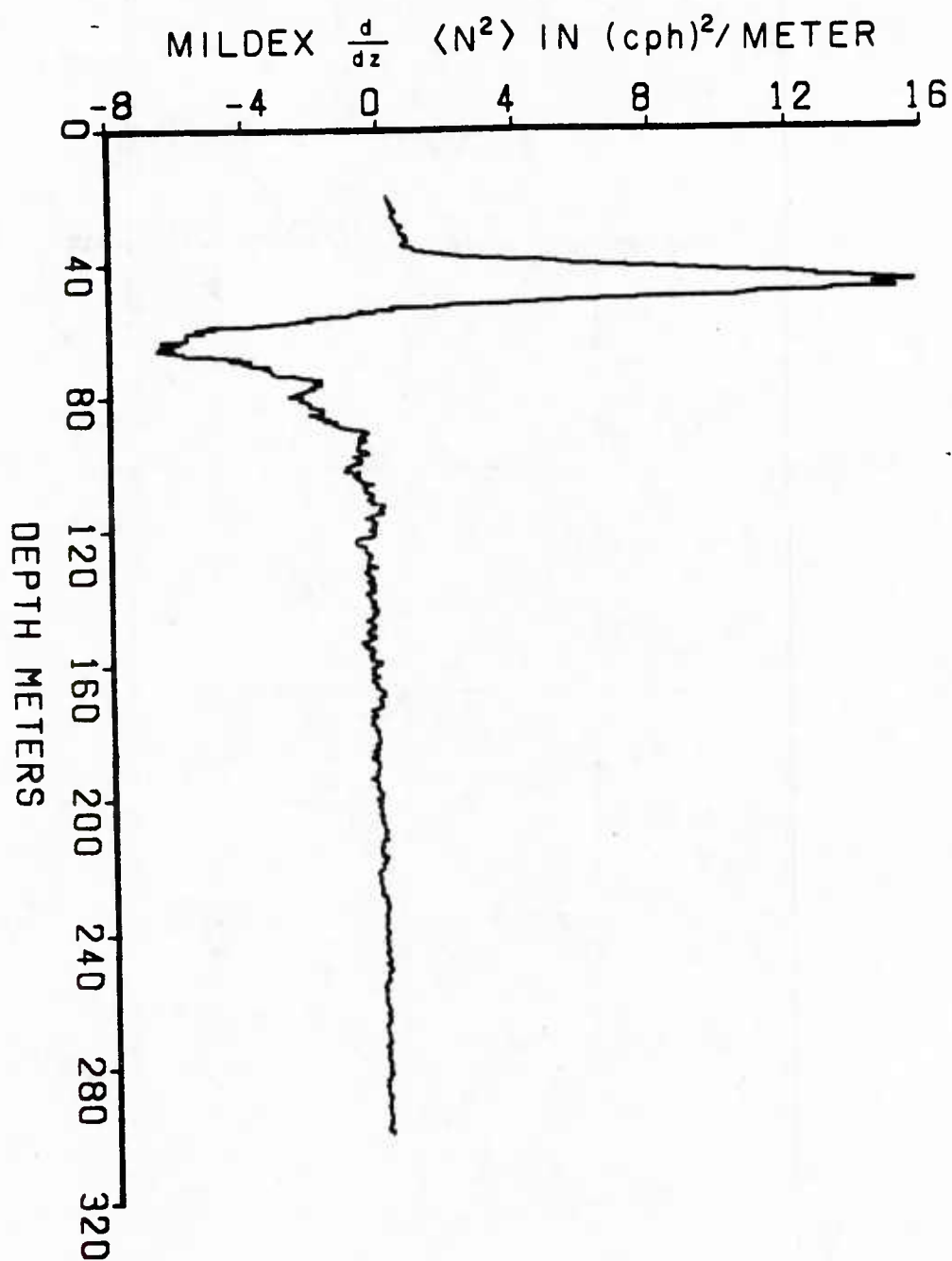


figure 5-11 Average profile during MILDEX of the vertical gradient of N^2 where N is Vaisala frequency.

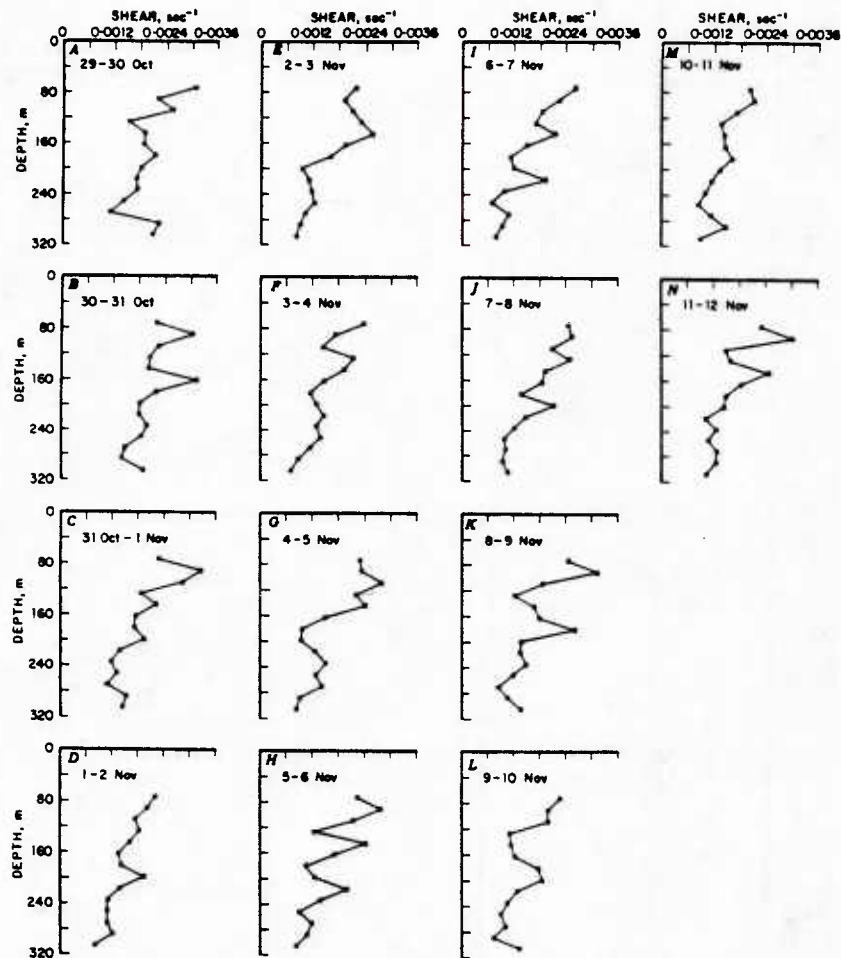


figure 5-12 Twenty-four hour average shear profiles calculated from the Doppler sonar current velocity profiles obtained during MILDEX (data courtesy A. J. Plueddemann).

Thirdly, resonant interaction involving internal waves of tidal period can be important in the pycnocline (Rattray et al., 1969).

A simple first order test for nonlinearity is to calculate the skewness. Skewness is one of a hierarchy of moments (mean, variance, skewness, kurtosis etc) which describes a probability density function (pdf). Linear processes have Gaussian shaped pdf's which have zero skewness. On the other hand, skewed pdf's are obtained from non-linear processes and hence skewness can be regarded as a measure of nonlinearity. As a guide, Lii (personal communication), who has worked extensively in the area of bispectral analysis of turbulence data, considers skewness values of 0.1 and above as indicative of nonlinearity. However, it must be noted that Lii typically deals with large amounts of laboratory data which represent many realizations of the processes under investigation (e.g. Helland, Lii and Rosenblatt, 1979)

Before calculating the skewness of the isopycnals, the lowest frequency (≤ 0.06) information was first removed with a high pass filter. The resulting time series contain information in the band 0.06 - 1 cph which spans the semi-diurnal tidal frequency and its first eleven harmonics. Thus any nonlinearity in the internal tide, which is not entirely vertically asymmetric, will contribute to the skewness. Fig. 5-13 shows skewness as a function of depth. For the majority of the depth range, except between 50-90 m, its value is positive. The largest values are found deeper where the corresponding amplitude of the internal tide is large (Fig. 5-10). Assuming for the moment that the skewness is entirely due to the nonlinear shape of the internal tide, one could conclude that positive skewness indicates that the tide has crests pointing downwards and, conversely, in the range 50-90 m, where skewness is negative, it has crests which are peaked upwards. Note that, between 40 and 50 m where the skewness is positive, $\partial N^2 / \partial z$ is also positive (Fig. 5-11) and between 50 and 90 m both change sign and become negative. The depths of the zero crossings for skewness and

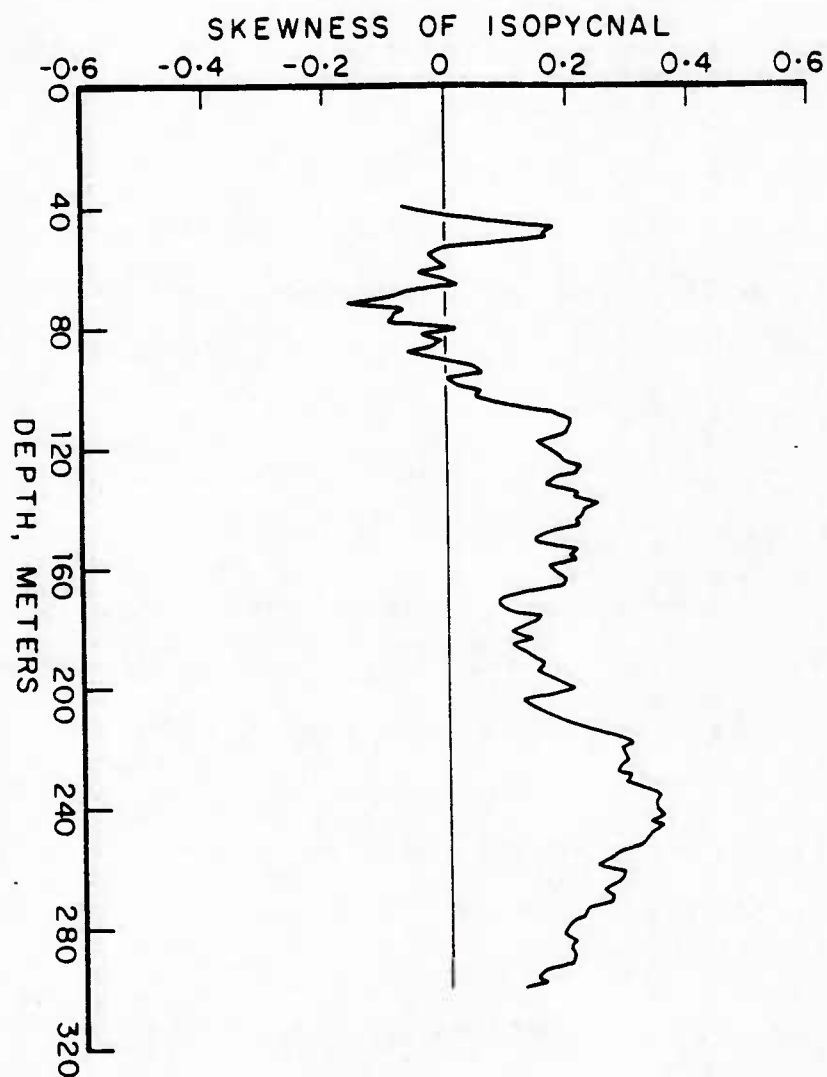


figure 5-13 Skewness of the 1983 (MILDEX) isopycnals.

$\partial N^2 / \partial z$ are approximately equal ($\sim 50\text{m}$). This type of behavior is exactly the kind Thorpe's model (1968) predicts in the regions of rapidly changing density (e.g. "tanh" density profile). Below the pycnocline the positive values of skewness are consistent with Thorpe's model (1968) for a linear density profile (Fig. 5-3). A qualitatively similar pattern for skewness is obtained for the 1980 isotherms (Fig. 5-14). During the 1980 experiment the depth of the mixed layer changed considerably (see Fig. 5-15) but on average the depth range for the thermocline was between 90 and 140 m which again is where we see negative values of skewness. This consistent pattern is evidence that the internal tide may be nonlinear in the upper ocean. If this is indeed the case, the amplitude of the harmonics, as a function of time, should be directly proportional to the amplitude of the fundamental. The following analysis was performed to test this hypothesis. Information in two frequency bands, 0.02 cph wide, centered at 0.08 and 0.16 cph were band-pass filtered out of the isopycnals displayed in Fig. 5-9. The resulting time series were plotted with color contouring (Fig. 5-16). We see that, during periods and at depths where higher internal tide fluctuations are present, there is a corresponding increase in the amplitude of the first harmonic. On the other hand, at times when the internal tide is weak, the first harmonic can be either weak or strong, evidence, perhaps, that there is also free wave energy present at this frequency. In the light of these encouraging results it was decided to continue the analysis with an investigation of the bispectra.

A vertically decimated sample of the 155 time series used in the bispectral analysis is shown in Fig. 5-9. These time series are 1011 points long, with a sampling interval of 21 minutes. Each record was padded with zeros out to 1024 points and its Fourier transform calculated. From these, bispectra were formed by the method prescribed in Appendix D. In Haubrich (1965) the derived confidence levels on zero

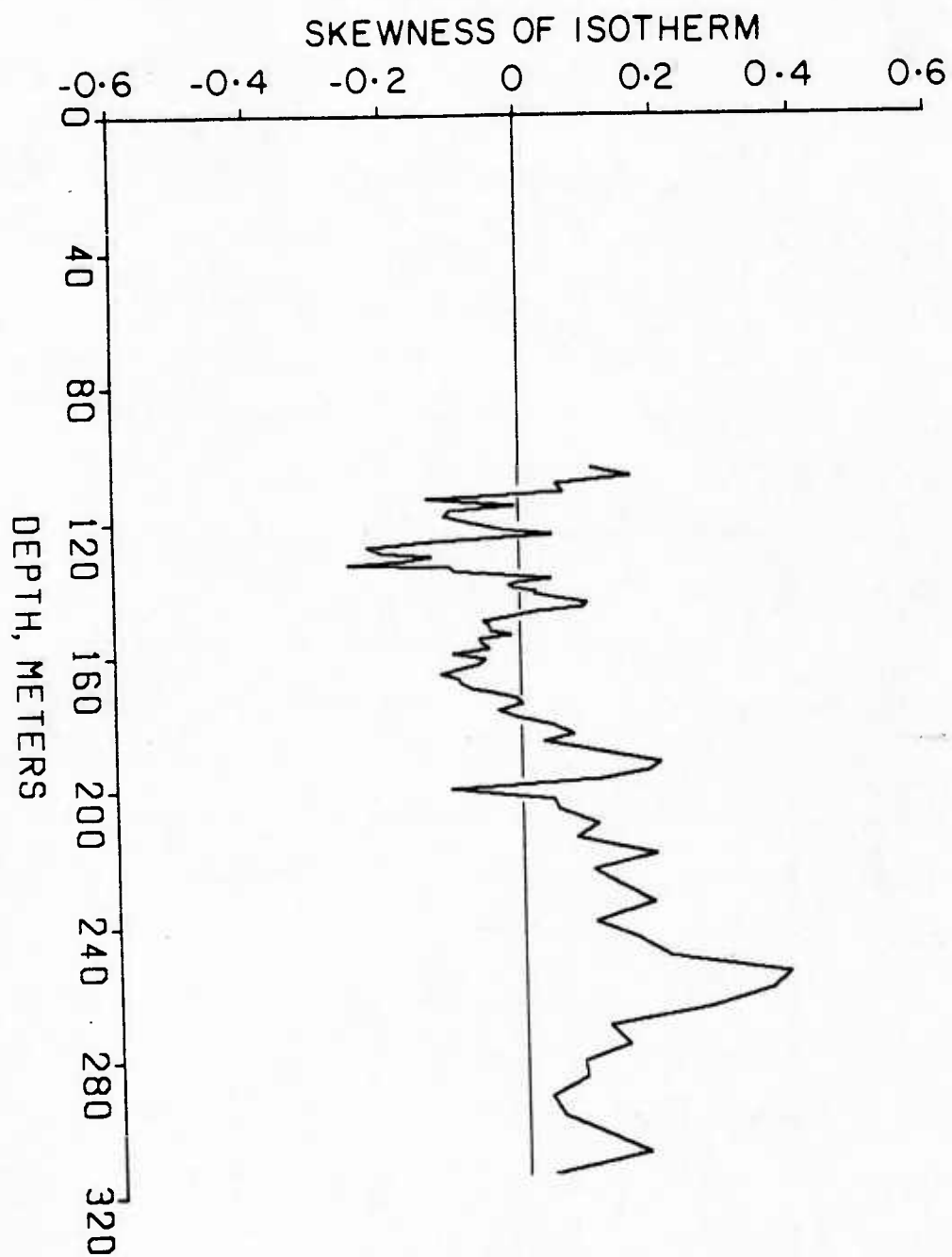


figure 5-14 Skewness of the 1980 isotherms.

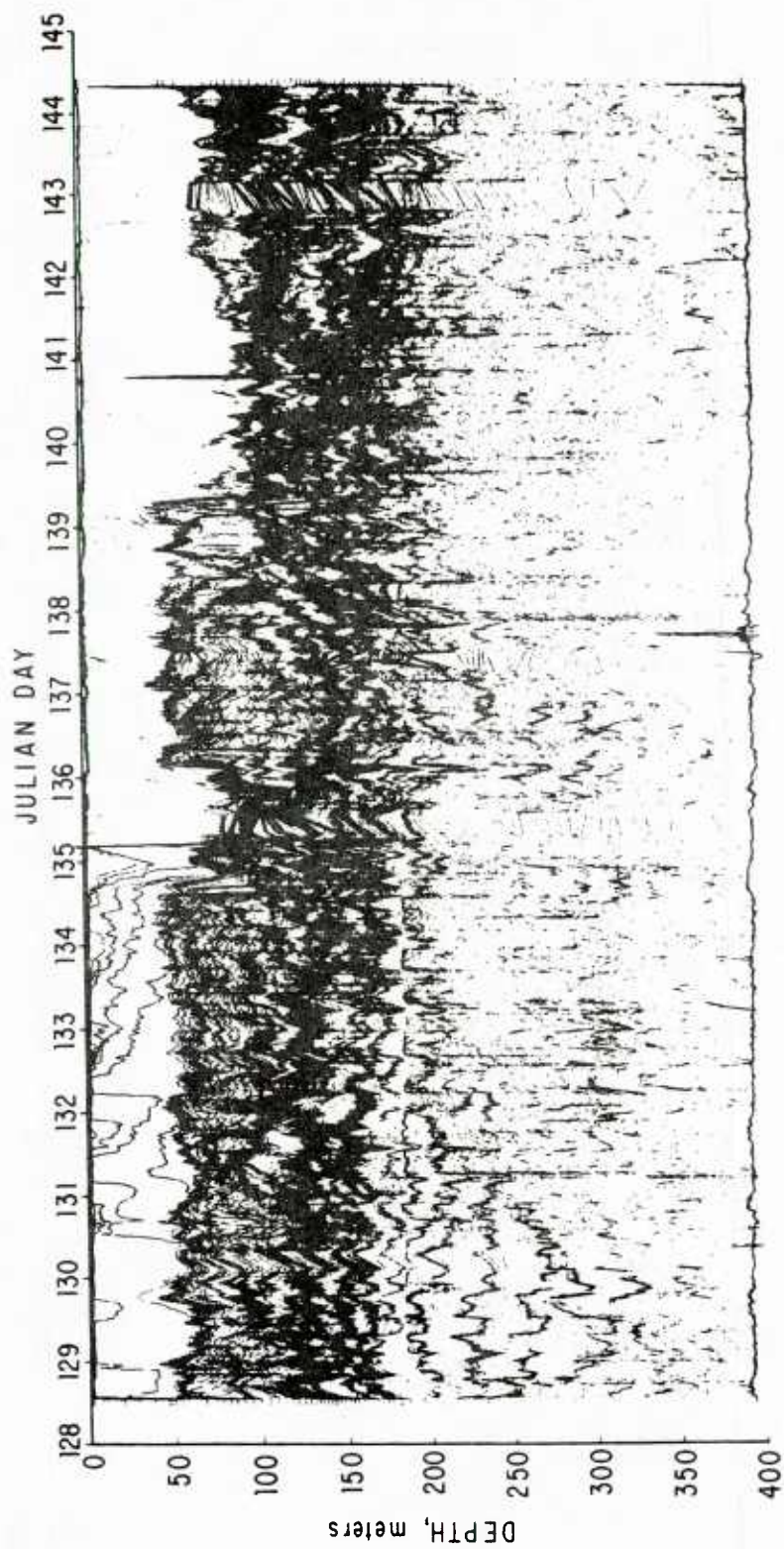


figure 5-15 A low pass filtered (<1 cph) version of the 1980 isotherms.

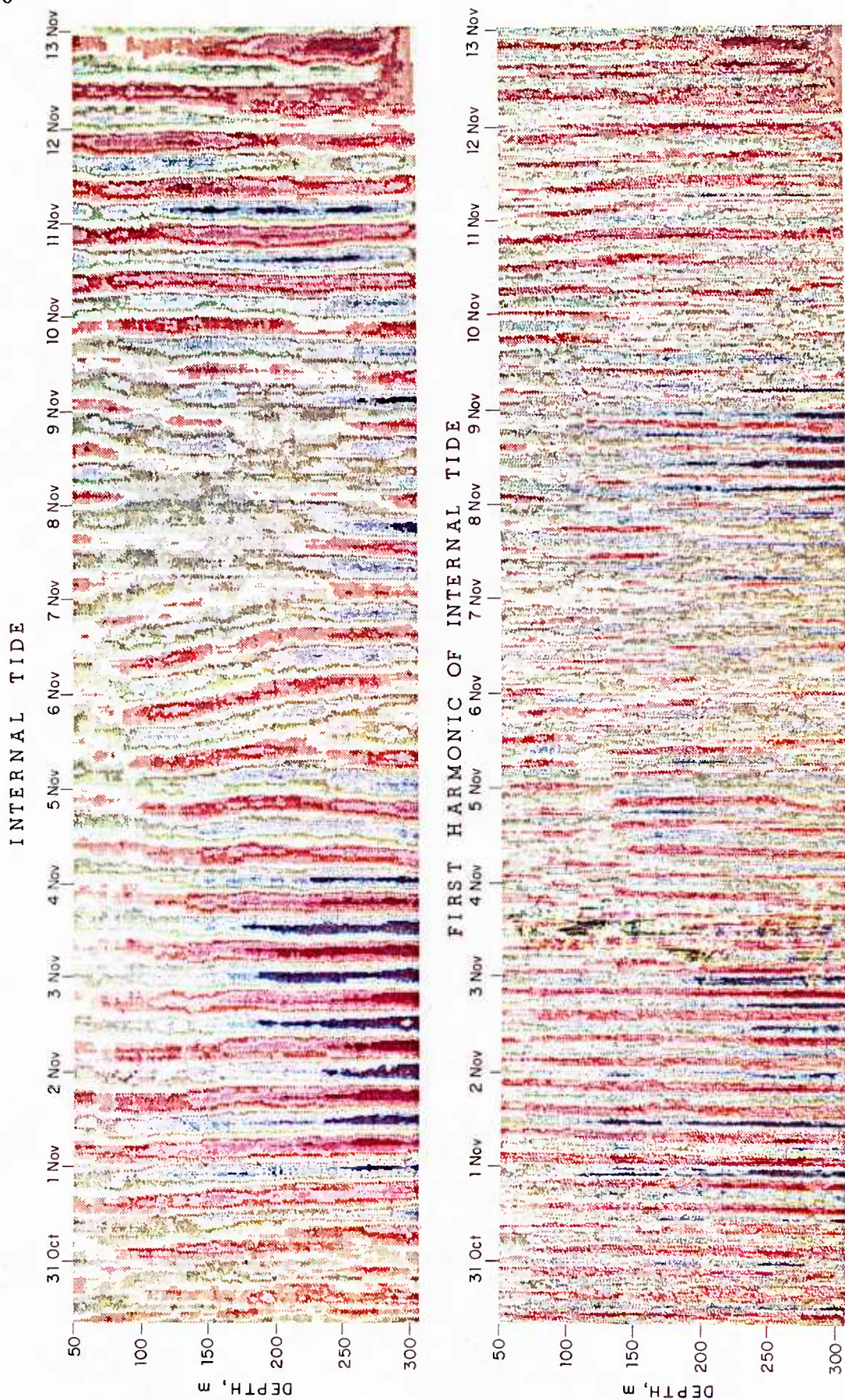


figure 5-16 Band pass filtered isopycnals plotted using color contouring. Pass bands are 0.02 cph wide centered at 0.08 and 0.16 cph.

bicoherence are based on ensemble averaging bispectra from separate realizations. Since we only have one realization of the process (i.e. the set of isopycnals, which are approximately 30 tidal periods long), extra degrees of freedom can only be obtained by "spatial" averaging over the frequency-frequency domain. This technique is acceptable as the internal tide, unlike the surface tide, is a broad band process. A moving window 7×7 (0.02 cph \times 0.02 cph) frequency bins in extent was applied resulting in estimates which have 98 degrees of freedom.* The corresponding 95% confidence level on zero bicoherence is 0.2.

Two representative bispectra are presented, the first is calculated from the 80 m isopycnal (Fig. 5-17) and the second from the 250 m isopycnal (Fig. 5-18). Only that portion of the bispectrum corresponding to the lower frequencies is displayed since it contains the majority of the relevant information. Note that the complete bispectrum for these isopycnals is defined over the triangle whose vertices have the frequency co-ordinates in cph of (0.0, 0.0) (1.43, 1.43) and (2.86, 0.0). Each isopycnal was first normalized by its standard deviation before its bispectrum was calculated. In this way, meaningful inter-comparisons could be made. The contour levels for both the real and imaginary parts of the bispectrum are set at ± 0.3 . Isometric plots of these quantities are displayed to give the reader an appreciation of the relative magnitudes of the peaks and valleys. The view is from slightly above and to the left of the line of symmetry. Together with each bispectrum, the spectrum and bicoherence are presented.

After inspection of Figs. 5-17 and 5-18, several conclusions can be drawn.

- 1) The overall level of activity in the bispectrum at 80 m is greater than that at the deeper depth, indicative that more quadratic coupling occurs at the shallower depth.

* Estimates which lie on the line of symmetry have 49 degrees of freedom and a 95% confidence level of 0.28.

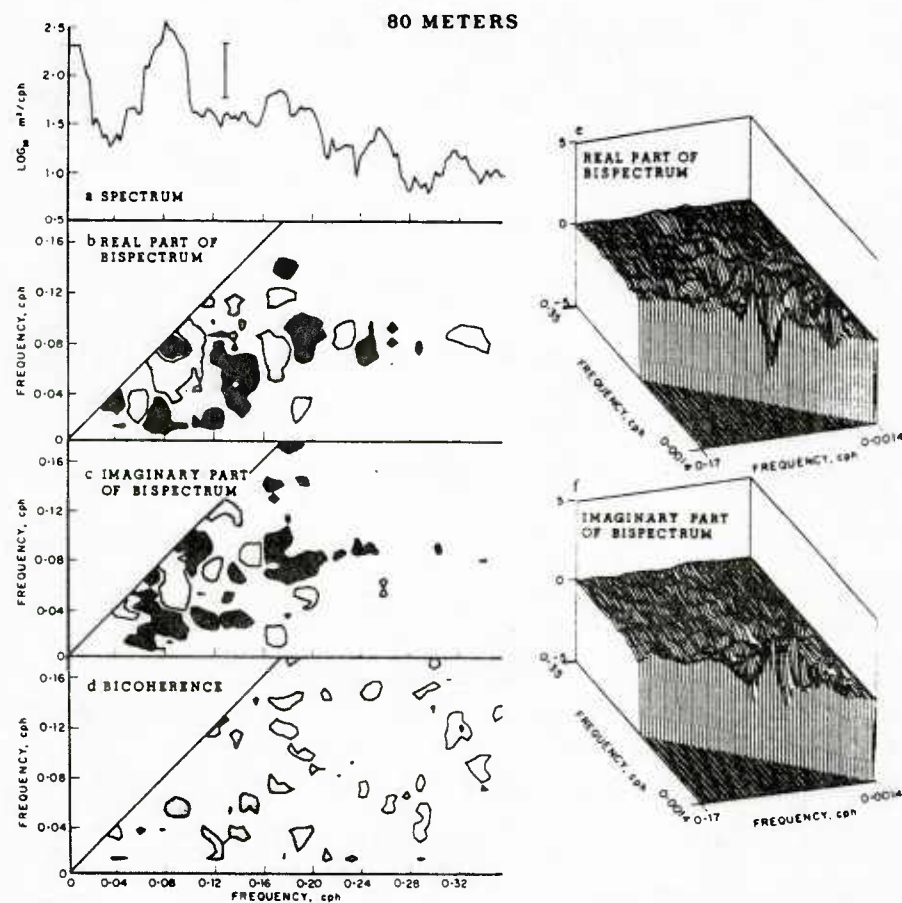


figure 5-17 The spectrum (a), bispectrum (b, c, e and f) and bicoherence (d) for the isopycnal whose average depth is 80 m. Only a section of the bispectrum and bicoherence is presented. The triangular domain over which these are completely defined has vertices with co-ordinates in cph (0.0, 0.0), (1.43, 1.43) and (2.86, 0.0).

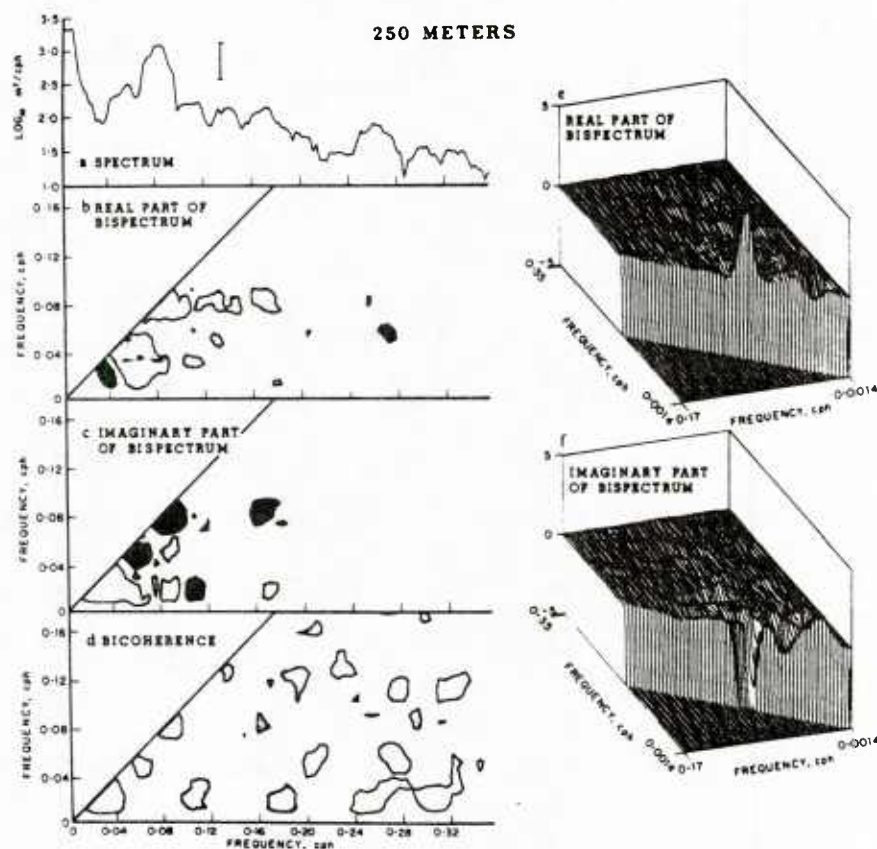


figure 5-18 The spectrum (a), bispectrum (b, c, e and f) and bicoherence (d) for the isopycnal whose average depth is 250 m. Only a section of the bispectrum and bicoherence is presented. The triangular domain over which these are completely defined has vertices with co-ordinates in cph (0.0, 0.0), (1.43, 1.43) and (2.86, 0.0).

2) The largest contribution to the bispectrum at both depths is at (f_T, f_T) where f_T is the semi-diurnal tidal frequency (0.081 cph). In both cases the estimate at (f_T, f_T) is complex, possessing both real and imaginary parts. These change in both sign and magnitude as we go from 80 to 250 m, indicating that the biphase at (f_T, f_T) is a function of depth.

3) Structure is found at both depths close to the ordinate associated with f_T indicating that the internal tide may be interacting with several different frequencies. In particular, structure in the neighborhoods of $(2f_T, f_T)$, $(3f_T, f_T)$ and $(4f_T, f_T)$ is evidence that the harmonics are coupled.

4) At both depths the bicoherence spectra are extremely noisy, undoubtedly a direct result of the limited amount of data available. The contouring level for bicoherence has been set at 0.2, the value of the 95% confidence level on zero bicoherence for an estimate *not* lying on the line of symmetry. At 80 m the bicoherence at (f_T, f_T) is below this level while at 250 m it is above. At 250 m the level at $(2f_T, f_T)$ is also above 0.2, evidence that, at the shallower depth, the harmonics are not as coupled to the fundamental.

5) Structure can be found at frequency pairs not involving tidal harmonics. For instance, at 250 m there is structure in both the bispectrum and the bicoherence in the neighborhood of (f_I, f_I) where f_I is the near-inertial frequency. Could this indicate a self-self interaction for near-inertial motions? This observation is interesting in view of the fact that the level of near-inertial energy observed throughout MILDEX was unusually low. Perhaps, during periods with higher near-inertial energy levels, more coupling involving this frequency band might be apparent.

In an effort to condense the information contained in the bispectrum, it was decided to focus on the contributions associated with the tide and its harmonics. Accordingly, the biphase and bicoherence at the relevant frequency pairs were

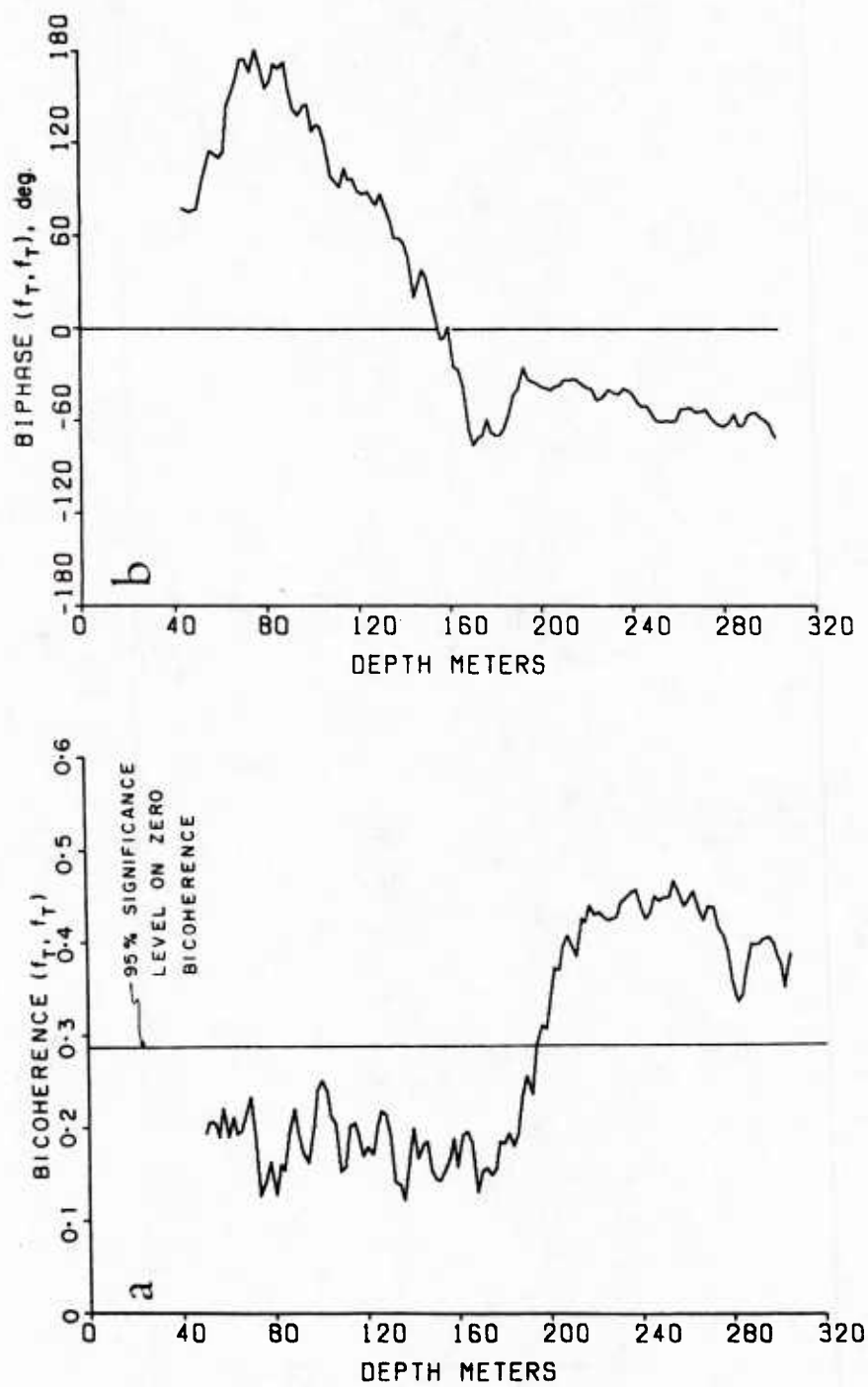


figure 5.19 The bicoherence (a) and biphaseness (b) at (f_T, f_T) vs. depth.

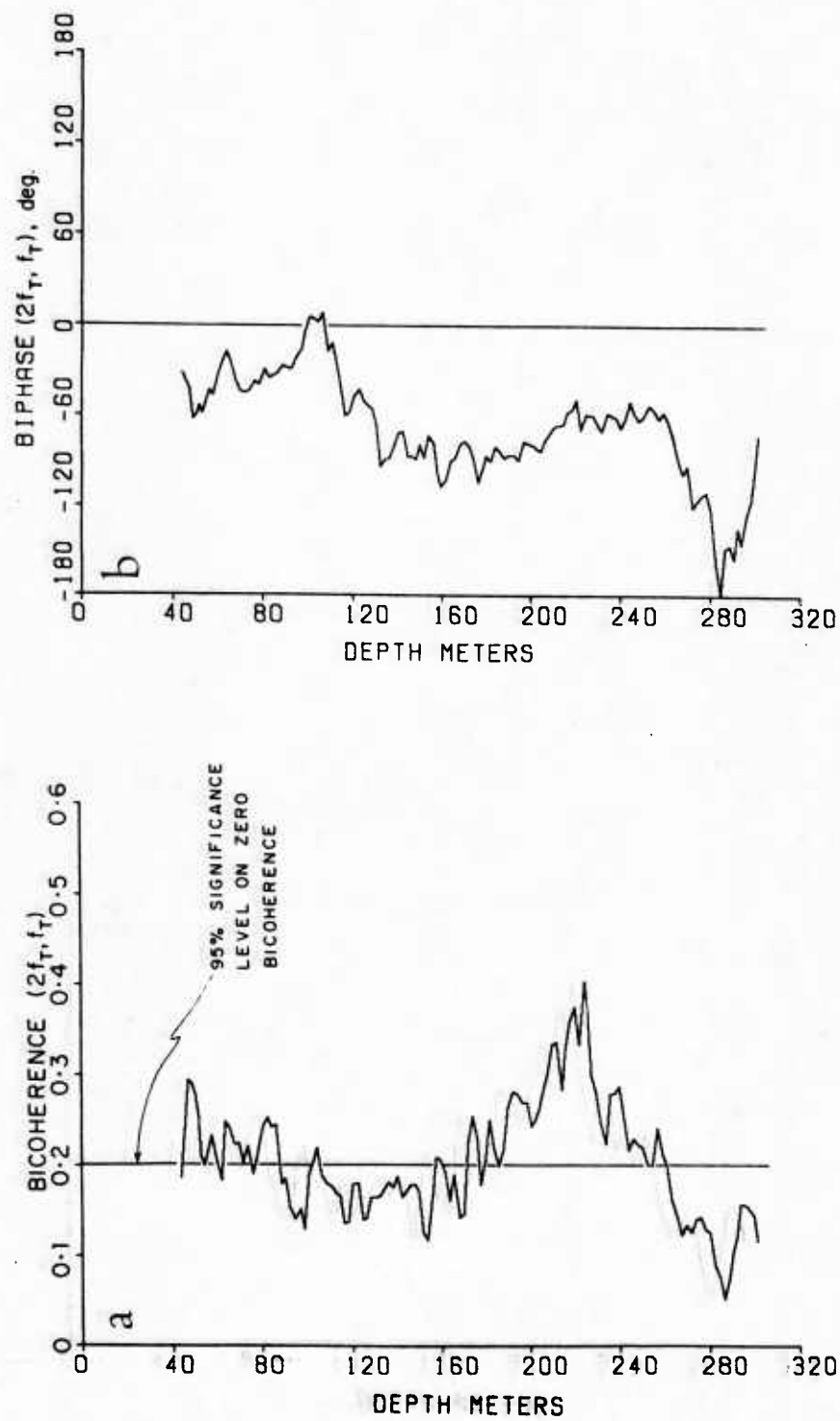


figure 5-20 The bicoherence (a) and biphaser (b) at ($2f_T, f_T$) vs. depth.

calculated as functions of depth. At the frequency pairs (f_T, f_T) and $(2f_T, f_T)$, these functions show non-random structure (Figs. 5-19 and 5-20). The bicoherence at (f_T, f_T) is significant at the deeper depths (> 200 m). Here we can conclude from the definition of bicoherence that $\sim 20\%$ of the variance in the first harmonic ($2f_T$) can be attributed to quadratic coupling. The biphas below 200 m tends towards -60° indicating that at these depths the internal tide is vertically asymmetric and tending towards a sawtooth profile (biphase $= -90^\circ$). Evidence of this shape can be seen in Fig. 5-21 which shows the 270 m isopycnal from 31 October - 4 November. At the shallower depths in the thermocline (~ 80 m), the biphas tends towards a value of 180° . Were these estimates statistically significant, they would imply that the internal tide is peaking upward like a Stoke's wave. At $(2f_T, f_T)$ larger values for bicoherence are again found at the deeper depths. Between 180 and 260 m where the highest values are observed, the biphas tends to a value $\sim -60^\circ$. At the other frequency pairs, involving higher harmonics, e.g. $(2f_T, 2f_T)$ $(3f_T, f_T)$, the depth structure of the biphas and bicoherence appears to be random.

It has been noted before that the bicoherence spectra are extremely noisy. This is thought to be due to the limited amount of data. Depth averaging of bispectra is a technique which can reduce this noise level. However, it should not be used as a way to increase confidence in the estimates. We see from the biphas and bicoherence plots that there appears to be more consistent behavior at the deeper depths. Accordingly the range chosen for depth averaging was 200-280 m and the results are displayed in Fig. 5-22. The maxima in the bicoherence now begin to exhibit a pattern which is reminiscent of coupled harmonics (see, for instance, Elgar and Guza (1985) Fig. 2). This is strong evidence that at the deeper depths the harmonics are *locally* forced.

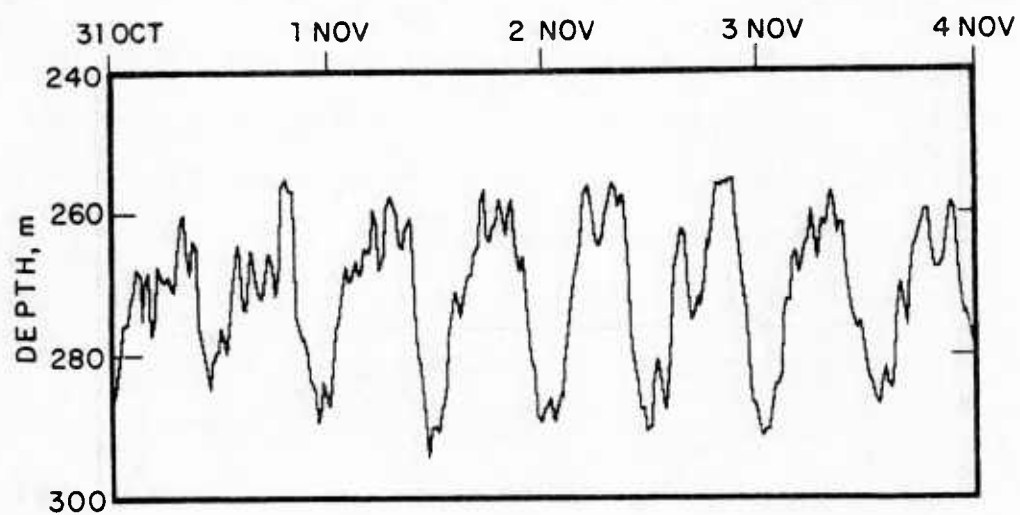


figure 5-21 The isopycnal whose average depth is ~ 270 m from 31 October - 4 November, 1983.

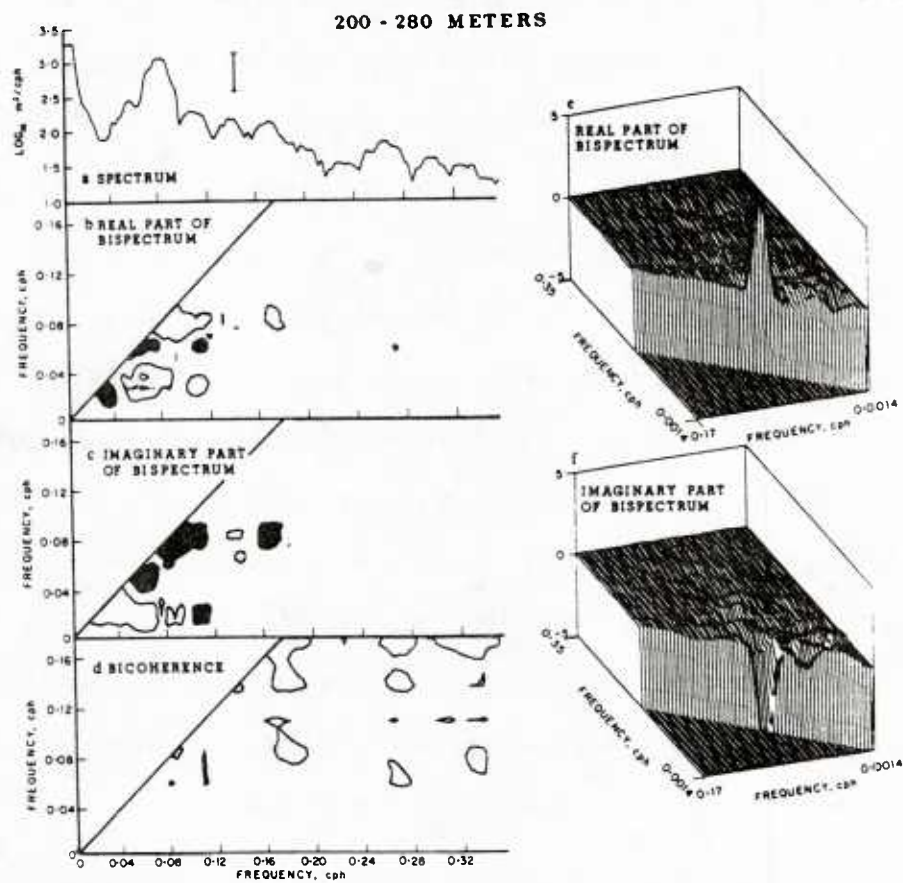


figure 5-22 Average spectrum, bispectrum and bicoherence over the depth range 200-280 m.

5.5 Discussion

The investigation of the bispectra was originally motivated by a desire to determine if the harmonics of the semi-diurnal tides are due to locally forced or free waves. The results of the present analysis do not permit us to give a clearcut answer to this question. With such a limited data set, it is not possible to calculate adequate statistics from which such firm conclusions can be drawn. Instead, the following more general but, nevertheless, worthwhile statements can be made.

There appear to be two different regimes in the water column which can be associated with differing behavior of the internal tide and its harmonics. These regimes are: 1) the shallower water in the depth range of the pycnocline and 2) the deeper water below 200 m. We find that the relative magnitudes of the harmonics are biggest in the pycnocline but that the bicoherences associated with them are biggest at the deeper depths. If the harmonics are simply due to one forcing mechanism, one would expect the highest bicoherence values to occur in the shallower water. Since this is not the case, and the bicoherence values associated with the harmonics are significant only in the deeper water, one suspects that local forcing is more important in the deeper water where the amplitude of the internal tide is greatest.

The following scenario is proposed to describe the observations. In the region of the pycnocline, where it is known that all the mechanisms leading to either locally forced or free waves can be effective, it is the free waves which are dominant. As a result, phase coupling between harmonics caused by local forcing is masked in the bicoherence by the random phase relationships of the free waves. At the deeper depths the dominant mechanism is local forcing, which can be due to either stratification or shear.

From the biphas at (f_T, f_T) we see that the non-linear shape of the internal

tide is a function of depth. At the deeper depths the biphasic at (f_T, f_T) tends to -60° , a value which is associated with a wave peaking downwards and approaching a sawtooth profile (biphase $= -90^\circ$). These observations are not consistent with the vertically symmetric shapes predicted by either of Thorpe's models. In Thorpe (1968), the second order equation for the wave profile (Eqn 3-2-26) is given by and, in

$$\eta = \frac{\alpha k}{\sigma} \Psi \cos(kx - \sigma t) - \frac{\alpha^2 k^2}{2\sigma^2} \left\{ \sum_{n=1}^{\infty} \frac{C_n^2}{4c^2 - C_n^2} a_n \Phi_n - \Psi \Psi' \right\} \cos 2(kx - \sigma t) + \alpha^2 f_3(z) \quad (5-9)$$

Thorpe (1978), the second order equation for the wave profile (Eqn. 12) is given by:

$$\eta = \epsilon \eta_1(z) \cos(kx - \sigma t + \delta) + \epsilon^2 \eta_2(z) \cos 2(kx - \sigma t + \delta) \quad (5-10)$$

Only biphasic values of 0° or 180° will result from such predictions. A model is required that allows for biphasic to vary with depth. In the theory for the shape of non-linear surface waves over a sloping bottom (Elgar & Guza, 1985) evolving biphasic values are predicted because spatially varying Fourier amplitudes for the harmonics are included in the model. This model also assumes that the harmonics satisfy the resonance condition for shallow water surface waves. This assumption plays a key role in the development of the theory. In Thorpe (1966) it is proved that resonant interaction is not possible amongst three waves belonging to the same mode. In particular, self-self interaction of the mode 1 internal tide is not possible. Any comparable internal wave model which allows for depth evolving biphasic will have to include some different physics.

Lastly, we see from the bicoherence that, at the deeper depths, significant proportions of the variances of the first two harmonics are due to quadratic coupling. In the case of the first harmonic, $\sim 20\%$ of its variance is attributable to forcing by the fundamental (the internal tide). This forcing is a means by which energy can be pumped from lower to higher frequencies. The internal tide can thus be regarded as a source for the internal wave continuum. This fact, coupled with the widespread

occurrence of semi-diurnal tidal harmonics, leads one to conclude that the internal tide is playing a major role as such a source. This view contradicts a proposal by Olbers and Pomphrey (1981) who discount the notion that it is a major source for the internal wave continuum. Their conclusions are based entirely on theoretical calculations involving weak nonlinear interactions.

CHAPTER 6

SUMMARY

The work described in this thesis addresses two issues which are concerned with the internal tide. The first is the directionality of the internal tide off Southern California and the second is the widespread occurrence in internal wave spectra of semi-diurnal tidal harmonics.

In an attempt to determine the directionality, data collected by FLIP during MILDEX in 1983 were analyzed. The observations indicate that the internal tide is low mode in character and that its direction of propagation is variable. However, there does appear to be a favored direction of propagation which is oriented approximately from the NNW to SSE. These findings are in approximate agreement with those of Murray Levine, another participant in MILDEX, whose conclusions are based on an independent set of measurements. These observations are not consistent with the commonly held view that the Patton escarpment is a major source for the internal tide in this region. Accordingly, theoretical models, such as those developed by Rat-tray which deal with internal tide generation at continental slopes, do not appear to be appropriate in this case. An alternative model, which takes into account different generation mechanisms, must be considered if the observations are to be more fully understood. These mechanisms may include generation of the internal tide by the barotropic tide passing over seamounts and the backscattering of the internal tide by topographic features.

Peaks have been observed in internal wave spectra at frequencies of the harmonics of the tide. At issue is whether these harmonics are A) artifacts of the measurement technique, B) the signature of free waves present at these frequencies, or C) the manifestation of local nonlinearity of the internal tide. If C) is the case, the harmonics have the potential to provide us with valuable information about energy

transfer mechanisms within the wavefield.

In an attempt to resolve this issue, CTD data collected by FLIP during two cruises were analyzed. Temperature profiles collected in 1980 were processed in a variety of different ways to determine if A) is important. In particular, the effects of finestructure contamination on fixed depth measurements is assessed. The analysis indicates that the type of measurement induced nonlinearity which finestructure contamination can produce, tends to obscure rather than cause the observed levels of harmonics.

In an attempt to differentiate between B) and C), the bispectra and related statistics of the 1983 isopycnals, which span the depth interval 0-310 m, were calculated. From the bicoherence, we see that the highest degree of quadratic coupling between the internal tide and its harmonics occurs at the greater depths (200-310 m) where the amplitude of the internal tide is highest. In this region of the thermocline the bicoherence is very low indicating that free waves dominate, in spite of the fact that the ratios of the variances of the harmonics to that of the fundamental are highest here. The depth variation of isopycnal skewness indicates that the inferred nonlinear shape of the internal tide is consistent with that predicted by Thorpe's model for the shape of progressive internal waves in a continuously stratified fluid. However, the biphasic values at (f_T, f_T) indicate that this nonlinear shape is, for the most part, vertically asymmetric. For instance, below 160 m a biphasic of $\sim 60^\circ$ is obtained implying a shape which approaches a sawtooth profile ($\sim 90^\circ$). Biphasic values such as these cannot be obtained from Thorpe's model which admits only values of 0° or 180° .

To conclude, we see from the bicoherence that, at the greater depths, significant proportions of the variances of the first two harmonics of the internal tide are due to quadratic coupling, $\sim 20\%$ in the case of the first harmonic. This forcing is

a means by which energy can be pumped from lower to higher frequencies. The internal tide can thus be regarded as a source for the internal wave continuum. This fact, coupled with the widespread occurrence of semi-diurnal tidal harmonics, leads one to conclude that the internal tide is playing a significant role as such a source. This view contradicts a recent proposal, based on weak nonlinear resonant interaction theory, which discounts the notion that it is a major source for the internal wave continuum.

REFERENCES

- Blackford, B. L. (1978). "On the generation of internal waves by tidal flow over a sill - a possible nonlinear mechanism," *J. Mar. Res.* **36**, 529-549.
- Briscoe, M. G. (1975). "Preliminary results from the Trimooored Internal Wave Experiment (IWEX)," *J. Geophys. Res.* **80**, 3872-3884.
- Cartwright, D. E., B. D. Zetler, and B. V. Hamon (1979). "Pelagic tidal constants," IAPSO Publication Scientifique.
- Davis, R. E., R. DeSzoeki, D. Halpern, and P. Niiler (1981). "Variability of the upper ocean during MILE. Part I: The heat and momentum balances," *Deep-Sea Res.* **28A**, 1427-1451.
- Desaubies, Y. and M. C. Gregg (1981). "Reversible and irreversible finestructure," *J. Phys. Oceanog.* **11**, 541-556.
- DeWitt, L. M., M. D. Levine, C. A. Paulson, and W. V. Burt (1985). "The semi-diurnal internal tide in JASIN," unpublished manuscript.
- Dietrich, G. (1944). "Die Schwingungssysteme der Halb-und Eintägigen Tiden in den Ozeanen," *Geographisch-Naturwissenschaftliche Reihe* **41**.
- Elgar, S. and R. T. Guza (in press). "Bispectral analysis of shoaling surface gravity waves," *J. Fluid Mech.*
- Elgar, S. and R. T. Guza (submitted). "Nonlinear model predictions of shoaling surface gravity wave bispectra," *J. Fluid Mech.*
- Fu, L. L. (1981). "Observations and models of inertial waves in the deep ocean," *Rev. of Geophys. and Space Physics* **19**, 141-170.
- Gregg, M. C. and W. C. Hess (submitted). "Dynamic response calibration of the Sea-Bird temperature and conductivity probes," *J. Atmospheric and Oceanic Technol.*

- Hasselmann, K. W., W. Munk, and G. MacDonald (1963). "Bispectrum of ocean waves," in *Time Series Analysis*, edited by M. Rosenblatt (Wiley, New York), pp. 125-139.
- Haubrich, R. A. (1965). "Earth noise, 5 to 500 millicycles per second, 1. spectral stationarity, normality and nonlinearity," *J. Geophys. Res.* **70**, 1415-1427.
- Hendershott, M. C. (1981). "Long waves and ocean tides," in *Evolution of physical oceanography*, edited by B. A. Warren and C. Wunsch (MIT Press), pp. 292-341.
- Hendry, R. (1977). "Observations of the semi-diurnal internal tide in the western North Atlantic," *Philosophical Trans. of the Royal Soc. of London Series A*, 1-24.
- IEEE Press (1979). "Programs for digital signal processing,"
- Irish, J., W. H. Munk, and F. Snodgrass (1971). " M_2 amphidrome in the northeast Pacific," *Geophys. Fluid Dynamics* **2**, 255-360.
- Kim, Y. C. and E. J. Powers (1979). "Digital bispectral analysis and its applications to nonlinear wave interactions," *IEEE Trans. in Plasma Science* **PS-7**, 120-131.
- Krauss, W. (1966). "Internal tides off southern California," NEL/Report.
- Lafond, E. C. (1966). in *Encyclopedia of Oceanography*, edited by R. W. Fairbridge (Litton Educational Publishing, Inc.).
- Levine, M. D., C. A. Paulson, M. G. Briscoe, R. A. Weller, and H. Peters (1983). *Internal waves in JASIN: Results of the Royal Society JASIN Project* (The Royal Society of London).
- Lii, K. S. and K. N. Helland (1981). "Cross-bispectrum computation and variance estimation," *ACM Trans. Math. Software* **7**, 284-294.
- McComas, C. H. (1978). "Bispectra of internal waves," Woods Hole Tech. Note 02543.
- McComas, C. H. and M. G. Briscoe (1980). "Bispectra of internal waves," *J. Fluid Mech.* **97, Part I**, 205-213.

- McKean, R. S. (1973). "Interpretation of internal wave measurements in the presence of fine-structure," *J. Phys. Oceanog.* **4**, 200-213.
- Muller, P. and D. J. Olbers (1978). "The IWEX spectrum," *J. Geophys. Res.* **83**, 479-500.
- Munk, W. (1981). "Internal waves and small scale processes," in *Evolution of Physical Oceanography*, edited by B. A. Warren and C. Wunsch (MIT Press), pp. 264-291.
- Neshyba, S. and E. J. C. Sobey (1975). "Vertical cross-coherence and cross-bispectra between internal waves measured in a multiple layered ocean," *J. Geophys. Res.* **80**, 1152-1162.
- Occhiello, L. M. and R. Pinkel (1976). "Temperature measurement array for internal wave observation," *OCEANS '76* **20E1-20E7**.
- Olbers, D. J. and N. Pomphrey (1981). "Disqualifying two candidates for the energy balance of oceanic internal waves," *J. Phys. Oceanog.*, 1423-1425.
- Phillips, O. M. (1971). "On spectra measured in an undulating layered medium," *J. Phys. Oceanog.* **1**.
- Phillips, O. M. (1977). *The dynamics of the upper ocean* (Cambridge University Press).
- Pinkel, R. (1975). "Upper ocean internal wave observations from FLIP," *J. Geophys. Res.* **80**, 3892-3910.
- Pinkel, R. (1981a). "On the use of Doppler Sonar for internal wave measurements," *Deep-Sea Res.* **28A**, 269-289.
- Pinkel, R. (1981b). "Observations of the near-surface internal wave field," *J. Phys. Oceanog.* **11**, 1248-1257.
- Pinkel, R. (1983). "Doppler Sonar observations of internal waves: wavefield structure," *J. Phys. Oceanog.* **13**, 804-815.
- Plueddemann, A. (in prep.). "Measurement of oceanic Reynolds' stresses using a multi-beam Doppler sonar."

- Prinsenbergh, S. J., W. L. Wilmot, and M. Rattray (1974). "Generation and dissipation of coastal internal tides," *Deep-Sea Res.* **21**, 263-281.
- Rattray, M. (1960). "On the coastal generation of internal tides," *Tellus* **12**, 54-62.
- Rattray, M. Jr., J. G. Dworski, and P. E. Kovals (1969). "Generation of long internal tides at the continental slope," *Deep-Sea Res.*, 179-195.
- Regal, R. and C. Wunsch (1973). " M_2 tidal currents in the western North Atlantic," *Deep-Sea Res.* **20**, 493-502.
- Sabinin, K. D. and V. A. Shulepov (1981). "Model of the frequency spectrum of internal waves in the ocean," *Izvestiya, Atmospheric and Ocean Physics* **17**, 48-53.
- Summers, H. J. and K. O. Emery (1963). "Internal waves of tidal period off southern California," *J. Geophys. Res.* **68**, 827-839.
- Thorpe, S. A. (1969). "On the shape of progressive internal waves," *Phil. Trans. of Royal Soc. of London, Series A* **26**, 563-614.
- Thorpe, S. A. (1978a). "On the shape and breaking of finite amplitude internal gravity waves in a shear flow," *J. Fluid Mech.* **85**, Part 1, 7-31.
- Thorpe, S. A. (1978b). "On internal waves in an accelerating shear flow," *J. Fluid Mech.* **88**, 623-639.
- Weigand, J. G., H. G. Farmer, S. J. Prinsenbergh, and M. Rattray (1969). "Effects of friction and surface tide angle of incidence on the coastal generation of internal tides," *J. Marine Res.* **27**, 241-259.
- Weller, R. A. (1981). "Observations of the velocity response to wind forcing in the upper ocean," *J. Geophys. Res.* **86**, 1969-1977.
- Wunsch, C. (1975). "Internal tides in the ocean," *Rev. of Geophys. & Space Physics* **13**, 167-182.

APPENDIX A

CALIBRATION OF 1980 CTD SENSORS

The CTD system operated during the 1980 experiment is described briefly in Chapter 2 and in more detail in Occhiello and Pinkel (1976). Data collected by it were used for the work described in Chapter 4. Unfortunately the sensors used were not calibrated either before or directly after the experiment. Instead, calibrations were performed in the Spring of 1982. The calibration of the Vibroton pressure sensor was achieved with the aid of a dead weight tester and those for the temperature and conductivity sensors were performed in the water bath at the SIO GEOSECS facility. The salinity of the water bath was kept constant during the entire period of calibration. Different conductivity values were obtained by changing the temperature of the bath water.

At the start and finish of the experiment, the towing vessel, USS Lipan, recorded CTD profiles to depths greater than 400 m. These measurements, taken with a Neil-Brown CTD operated by GEOSECS personnel, were used as another reference in the calibration of the temperature and conductivity sensors.

A.1 Vibroton Pressure Sensor (S/N 4173)

The points obtained by calibrating this sensor with the dead weight tester are plotted in Fig. A-1. The calibration was performed at room temperature (23.1 °C). The quadratic curve fitted to these data is described by equation (1) in table A-1.

In all the equations f represents the output frequency of the sensor.

Eqn. #	Eqn.	A	B	C
(1)	Pressure (decibars) $= A + Bf + Cf^2$	0.18202024 $\times 10^4$	0.48292 $\times 10^{-2}$	-0.28028576 $\times 10^{-5}$
(2)	Temperature ($^{\circ}\text{C}$) $= A + Bf + Cf^2$	-0.35202763 $\times 10^2$	0.69402810 $\times 10^{-2}$	-0.18877472 $\times 10^{-6}$
(3)	Temperature ($^{\circ}\text{C}$) $= A + Bf + Cf^2$	-0.9867009 $\times 10^2$	0.23478558 $\times 10^{-2}$	-0.11066360 $\times 10^{-7}$
(4)	Temperature ($^{\circ}\text{C}$) $= A + Bf$	-0.52151329 $\times 10^2$	0.92292845 $\times 10^{-3}$	
(5)	Conductivity (mmhos/cm) $= A + Bf$	-0.50015923 $\times 10^2$	0.23996127 $\times 10^{-2}$	
(6)	Conductivity (mmhos/cm) $= A + Bf$	-0.42643288 $\times 10^2$	0.17017554 $\times 10^{-2}$	
(7)	Conductivity (mmhos/cm) $= A + Bf$	-0.39507004 $\times 10^2$	0.21355264 $\times 10^{-2}$	
(8)	Conductivity (mmhos/cm) $= A + Bf$	-43.2 $\times 10^2$	0.17017554 $\times 10^{-2}$	

Table A-1 Calibration constants for the temperature and conductivity sensors

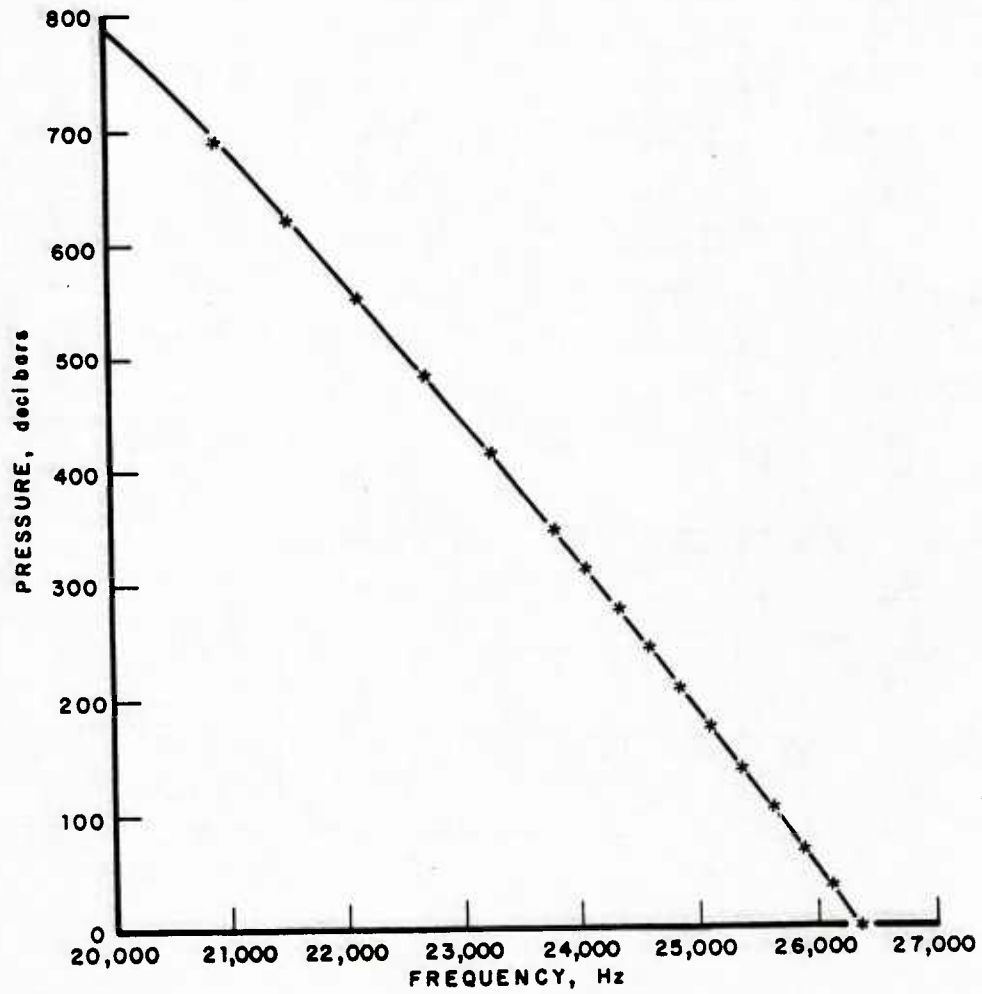


figure A-1 Calibration curve for Vibroton pressure sensor (S/N 4173).

A.2 Temperature Sensors

The upper temperature sensor (S/N 80-8) was cycled in the water bath through the range 7.4°C to 18.65°C . The calibration coefficients obtained (see equation (2)) were altered very slightly so that the last temperature profile of the experiment matched more closely the corresponding Neil-Brown profile (see Fig. A-2). During the course of the experiment the lower temperature sensor (S/N 80-3), which we subsequently lost, was replaced by another (S/N 80-2). It was cycled through the temperature range 6.2°C to 10.7°C resulting in the calibration curve shown in Fig. A-3 and described by equation (3). The profile at the end of the experiment calculated with this equation agrees very well with the corresponding Neil-Brown profile.

To calibrate 80-3, profiles before and after the change of sensors were forced to match up. This technique resulted in equation (4) for 80-3.

A.3 Conductivity Sensors

A variety of methods were used in an attempt to successfully calibrate the conductivity cells. As none of these proved entirely satisfactory, conductivity data were not used in any subsequent analyses. Nevertheless, a description of the work is included for completeness.

The upper conductivity cell (S/N 80-5) was first calibrated in the water bath. The salinity of the water was kept constant at 33.564 ppt and the bath temperature varied so as to cycle the conductivity of the water through the range 36.408 to 44.645 mmhos/cm. The curve obtained is shown in Fig. A-4 and is described by equation (5). Agreement between the resulting upper conductivity and Neil-Brown profiles was reasonable except in the lowest part of the upper profile where the frequency output from the sensor went out of its passband range. Consequently, attempts to calibrate the

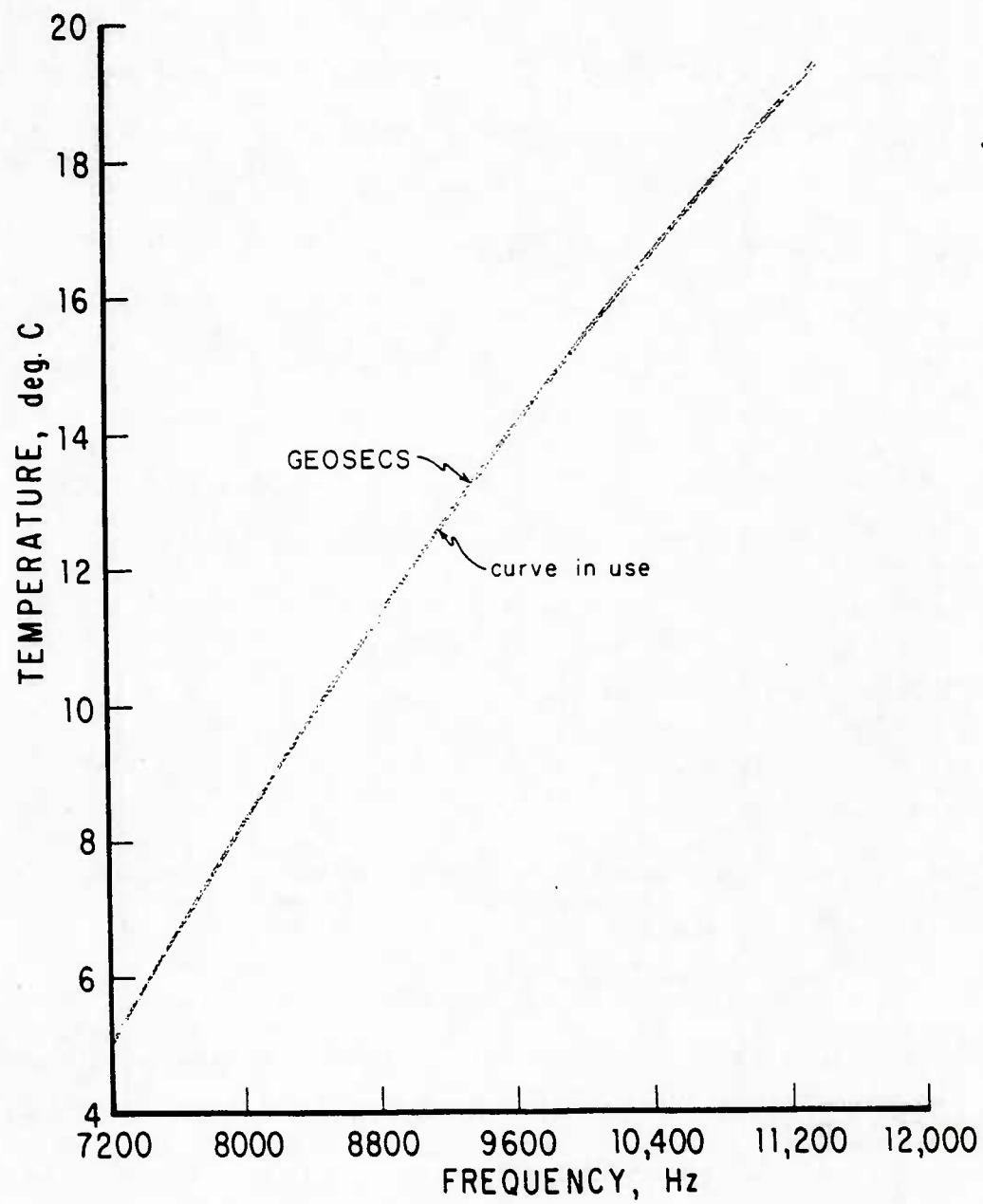


figure A-2 Calibration curve for upper temperature sensor (S/N 80-8).

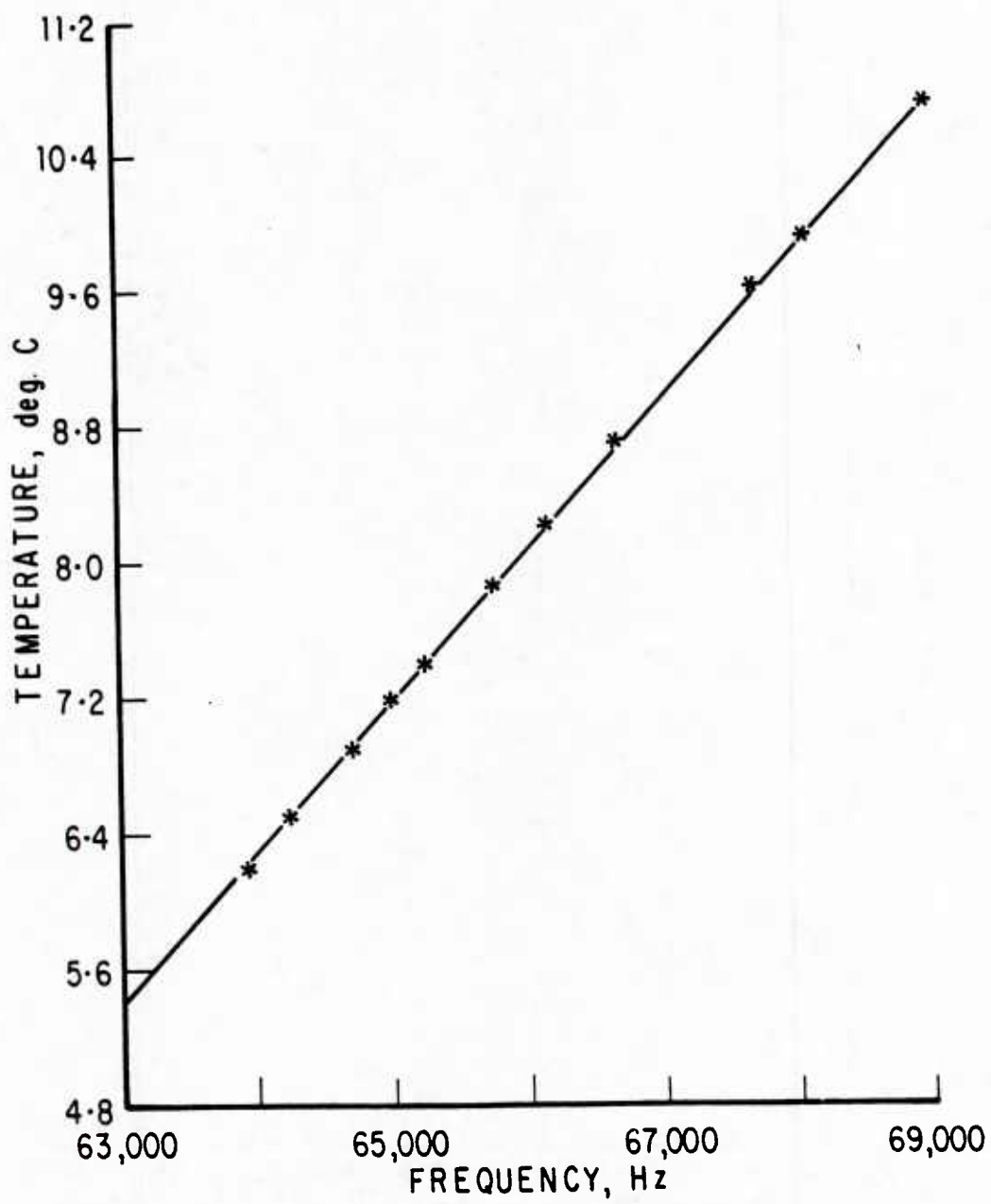


figure A-3 Calibration curve for lower temperature sensor (S/N 80-2).

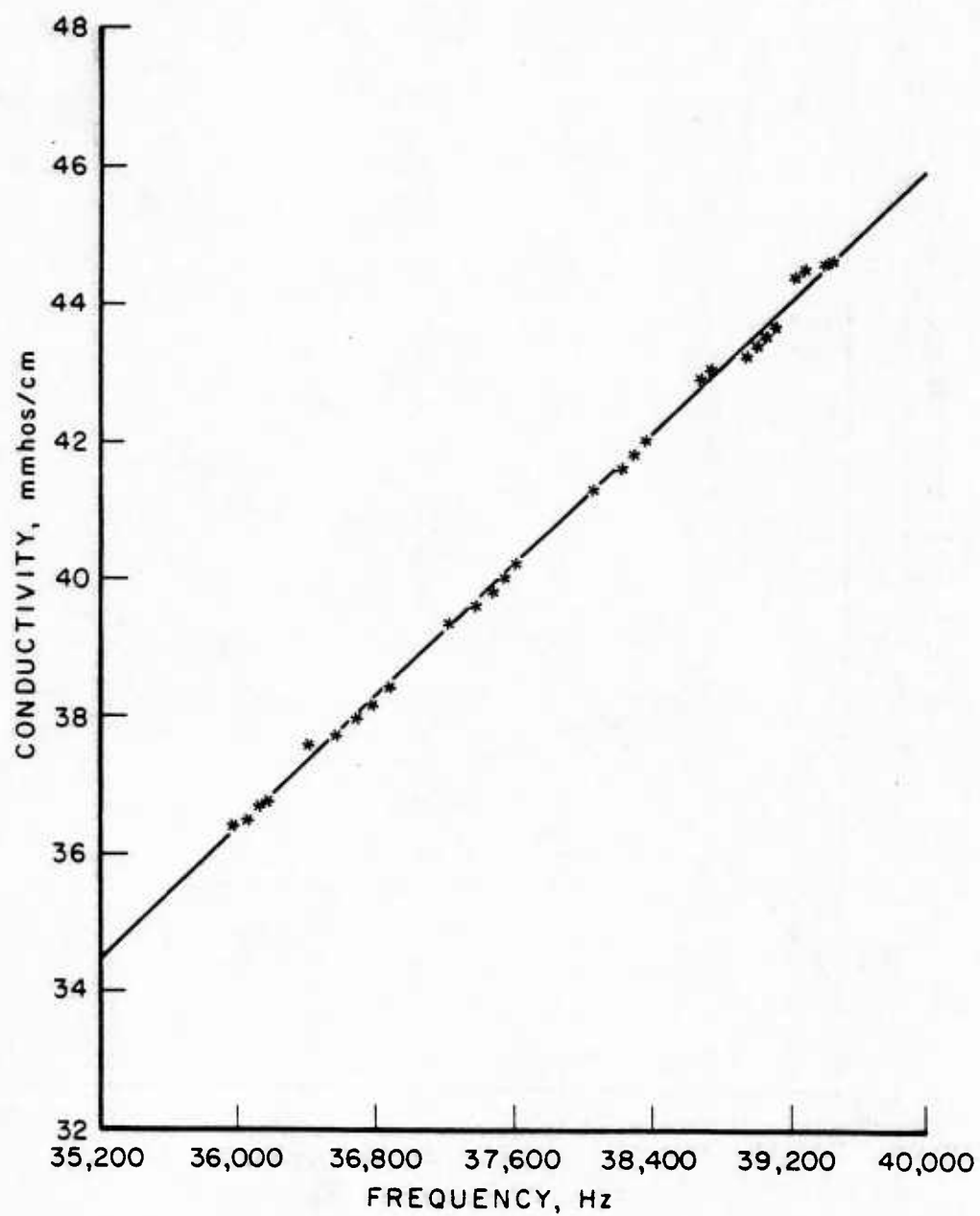


figure A-4 Calibration curve for upper conductivity cell (S/N 80-5).

lower conductivity cell (S/N 80-6) by using the overlap region, led to unreliable results. Instead, the lower conductivity profiles were forced to match up with the Neil-Brown profiles, a procedure which led to equation (6) for the lower conductivity cell. A new calibration curve, described by equation (7), for the upper cell was obtained by using the few good points in the overlap region. This method led to poor agreement between the upper conductivity and the Neil-Brown profiles.

An additional problem experienced with the lower sensor was that its calibration drifted during the course of the experiment. In an attempt to overcome this problem two curves were used, one before decimal Julian day 134.83926 and the other afterwards. The calibration equation corresponding to the latter part of the experiment is equation (6). The equation for the earlier part is equation (8).

APPENDIX B

THE SEA-BIRD ELECTRONICS CTD SYSTEM

The Sea-Bird Electronics (SBE) CTD system was deployed from FLIP during an engineering cruise in May 1983 and then, again, during MILDEX in October/November 1983. It is responsible for data presented in Chapters 3 and 5.

The system has two parts, a fish (Fig. B-1) and a deck unit (Fig. B-2). The fish consists of an oceanographic thermometer, a conductivity cell, a Parascientific digiquartz pressure transducer and associated electronics which are housed in an aluminum pressure casing. Details relating to the thermometer and the conductivity cell can be found in figures B-3 and B-4. All three sensors were calibrated during the period December 1982 - February 1983, with the thermometer and the conductivity cell being recalibrated in September 1983. The work was performed by personnel from Parascientific and Sea-Bird Electronics. The data sheets can be found on pages 129-131.

The electronics inside the fish digitize and multiplex the signals before transmitting them, via the conductor inside the electro-mechanical cable, to the deck unit onboard FLIP. Inside the deck unit the signals are demultiplexed and an averaging operation is performed that results in an effective sampling rate of 12 hertz. The data are then transmitted via an RS232 port to an HP1000 computer where the information is recorded on digital tape. The SBE system was chosen for use in conjunction with FLIP's rapid profiling system because of the fast response characteristics of the conductivity and temperature sensors. Details of these can be found in Gregg and Hess (1984). During MILDEX, profiles down to 310 m were obtained every three minutes with the package attaining fall rates of up to 4 m/s. At such fast speeds salinity spiking is still a problem in high temperature gradient regions. Salinity

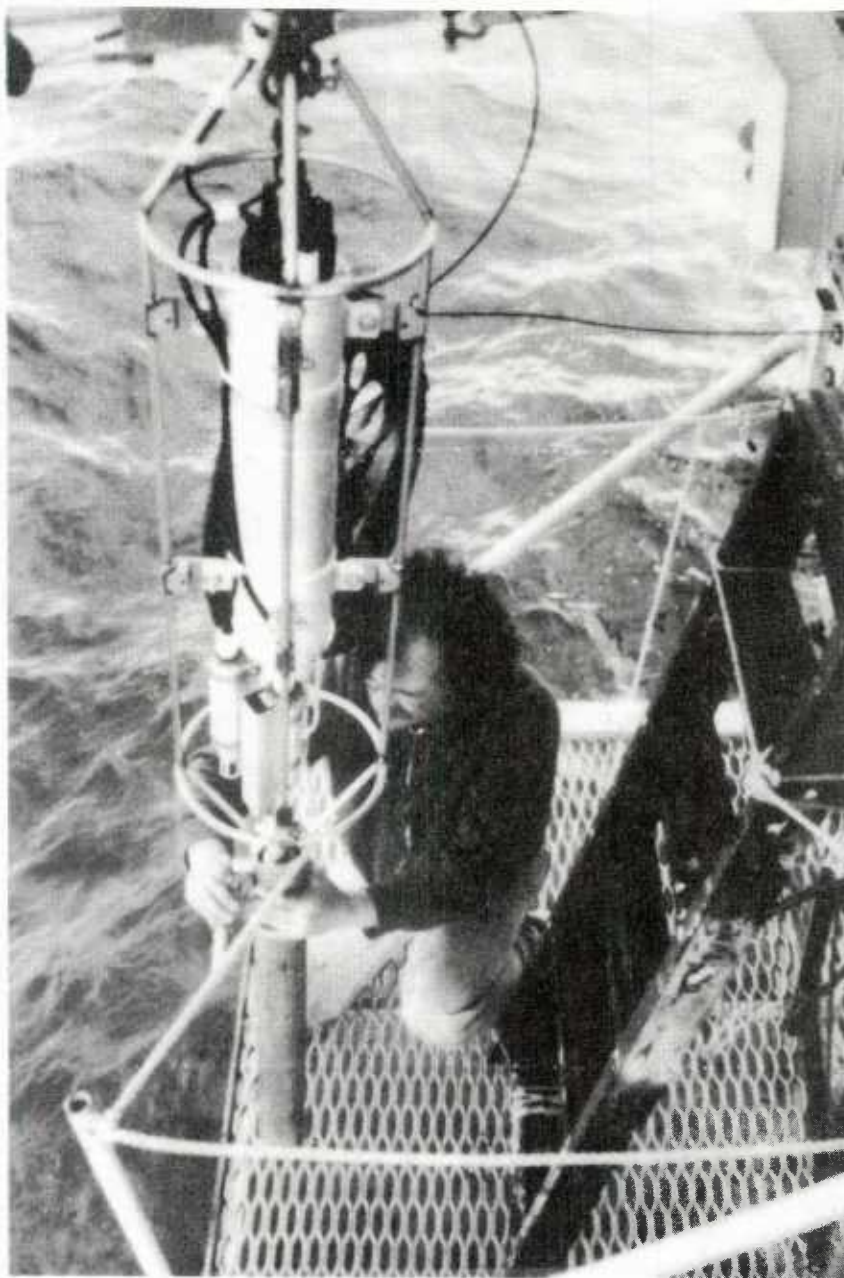


figure B-1 The CTD fish ready for deployment from FLIP.

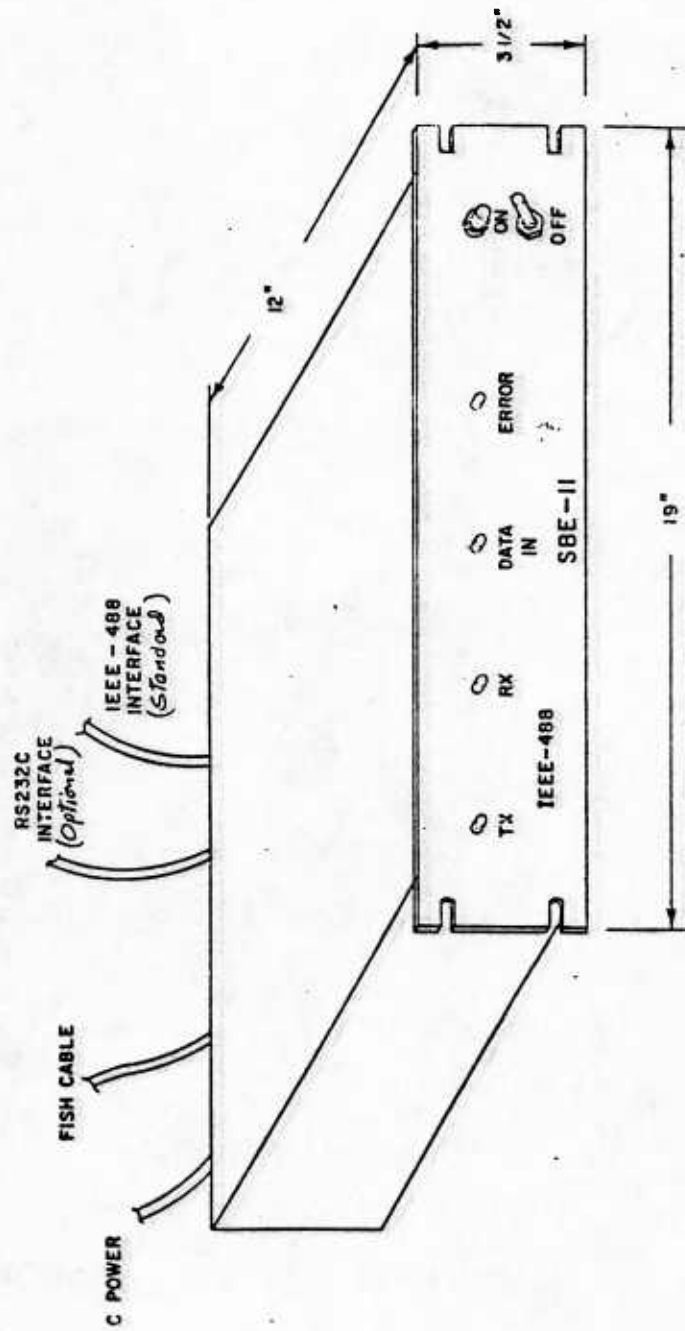
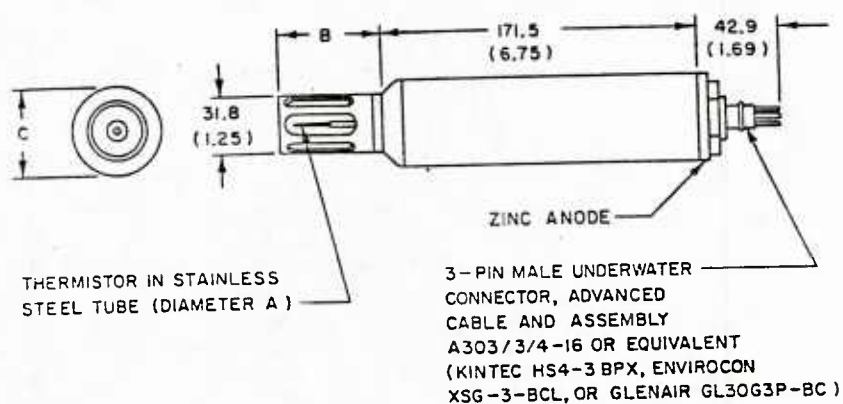


figure B-2 The SBE deck unit.

OCEANOGRAPHIC THERMOMETER MODEL SBE - 3

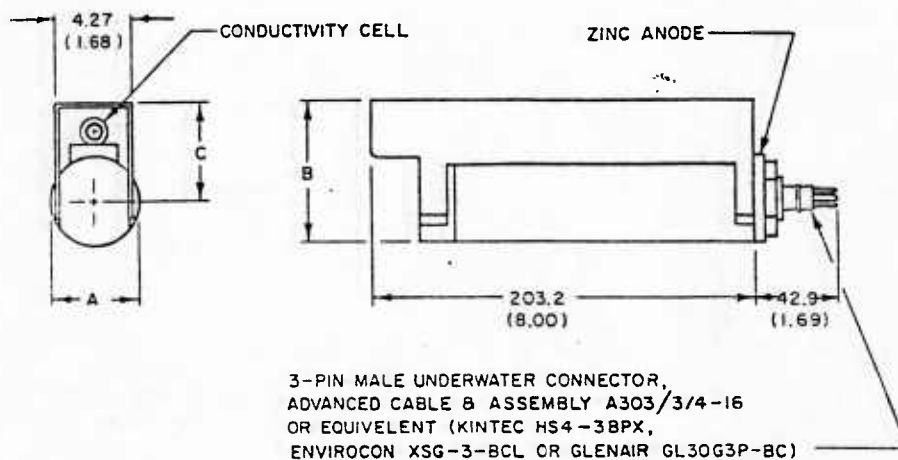


• DIMENSIONS AND WEIGHT SHOWN ARE IN MM (INCHES) AND GRAMS (OUNCES)

MODEL NUMBER	PRESSURE RATING	RESPONSE TIME	A	B	C	WEIGHT
SBE-3-01/F	5,000 PSI	≈ 50 MS	0.8 (0.032)	55.9 (2.20)	48.3 (1.9)	630 (22)
SBE-3-01/S	5,000 PSI	≈ 200 MS	2.1 (0.083)	84.8 (3.34)	48.3 (1.9)	630 (22)
SBE-3-02/F	10,000 PSI	≈ 50 MS	0.8 (0.032)	55.9 (2.20)	54 (2.12)	870 (31)
SBE-3-02/S	10,000 PSI	≈ 200 MS	2.1 (0.083)	84.8 (3.34)	54 (2.12)	870 (31)

figure B-3 The SBE thermometer.

CONDUCTIVITY METER MODEL SBE-4



- INSIDE OF CELL GUARD IS COATED WITH TRIBUTYL TIN OXIDE ANTI-FOULANT
- DIMENSIONS AND WEIGHT SHOWN ARE IN MM (INCHES) AND GRAMS (OUNCES)

MODEL NUMBER	PRESSURE RATING	A	B	C	WEIGHT
SBE 4-01	5,000 PSI	48.3 (1.9)	77.2 (3.04)	53.1 (2.09)	735 (26)
SBE 4-02	10,000 PSI	54.0 (2.12)	82.9 (3.26)	55.9 (2.2)	965 (34)

figure B-4 The SBE conductivity meter.

CALIBRATION COEFFICIENTS

DIGIQUARTZ PRESSURE TRANSDUCER

<u>SERIAL NO.:</u>	<u>MODEL:</u>	<u>PRESSURE RANGE:</u>	<u>CUSTOMER:</u>
13695	2900-AS-002	0 - 900 PSIA	SEA-BIRD ELECTRONICS

Installed in Fish

Calibration accuracy is 0.015% for pressure below 50 psi, 0.025% for pressures between 50 psi and 400 psi, and .03% above 400 psi.

CAUTION: Note pressure range. Do not apply more than 20% overpressure.

LINEARIZATION EQUATION:

$$P = A(1 - T_0/T) - B(1 - T_0/T)^2$$

COEFFICIENTS: OIL FILLED

TEMP.	70°F/21°C	70°F/21°C
A	9943.08 PSIA	
B	5009.10 PSIA	
T ₀	24.81514 MICROSECONDS	

COMPUTER RE-CHECK

DATE: DECEMBER 17, 1982



PAROSCIENTIFIC INC.

4500 145th AVE. NE
REDMOND, WASH 98052

Prepared by M. Miller DEC / 17 / 82

REV. A(H.P.)

Table B-1 Calibration constants for the digiquartz pressure transducer.

SEA-BIRD ELECTRONICS, INC.
 4735 W. MERCER WAY
 MERCER ISLAND, WASHINGTON 98040
 TELEPHONE: (206) 232 8958

TEMPERATURE CALIBRATION DATA
 CALIBRATION DATE: SEPTEMBER 1983

SENSOR SERIAL NUMBER = 555

A = 3.67461572E-03
 B = 4.1121951E-04
 C = 1.92262857E-05
 D = 4.93366636E-06
 F0 = 6489.02

BATH TEMP	INSTRUMENT FREQ	INSTRUMENT TEMP	RESIDUAL
31.018	12355.41	31.018	0
27.2829	11532.86	27.2829	0
22.9646	10629.31	22.965	4E-04
19.0073	9844.86	19.0068	-1E-03
14.9874	9090.34	14.9872	-2E-04
11.2303	8422.72	11.2304	1E-04
7.0399	7719.89	7.0399	0
3.2509	7121.59	3.2517	8E-04
-1.0127	6489.02	-1.0127	0

$$T = 1 / (A + B(\ln(F0/F)) + C(\ln(F0/F))^2 + D(\ln(F0/F))^3) - 273.15 \quad (\text{DEGREES C})$$

$$\text{RESIDUAL} = \text{INSTRUMENT TEMPERATURE (T)} - \text{BATH TEMPERATURE}$$

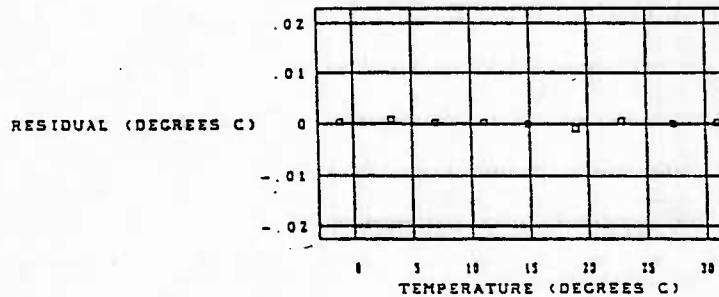


Table B-2 Calibration constants for the SBE thermometer.

SEA-BIRD ELECTRONICS, INC.
 4735 W. MERCER WAY
 MERCER ISLAND, WASHINGTON 98040
 TELEPHONE: (206) 232 8958

CONDUCTIVITY CALIBRATION DATA
 CALIBRATION DATE: SEPTEMBER 1983

FSS 1978: C(35,15,0) = 42.914 MMHOS/CM

SENSOR SERIAL NUMBER = 139

A = 1304.08624
 B = 1.1474449E-11
 C = 1.1E-03
 N = 2.88

BATH TEMP	BATH SAL	BATH COND	INSTRUMENT FREQ	INST COND	RESIDUAL
31.018	34.988	59.422	11548.88	59.421	-1E-03
27.2829	14.939	25.729	7619.14	25.7281	-9E-04
22.9644	34.988	50.935	10701	50.9359	9E-04
19.0078	14.94	21.704	6999.93	21.7025	-1.5E-03
14.9874	34.987	42.888	9824.25	42.8889	5E-04
11.2303	14.938	18.106	6395.21	18.1052	-8E-04
7.0399	34.986	35.307	8920.79	35.306	-1E-03
2509	14.937	14.64	5752.33	14.6417	1.7E-03
1.0127	34.987	28.159	7970.87	28.1585	-5E-04

CONDUCTIVITY = (FA2)/(A-B(FAN))^2 + C(TA2) (MMHO/CM)

RESIDUAL = INSTRUMENT CONDUCTIVITY - BATH CONDUCTIVITY

NOTE: DIVIDE MMHO/CM BY 10 TO OBTAIN SIEMENS/METER (S/M)

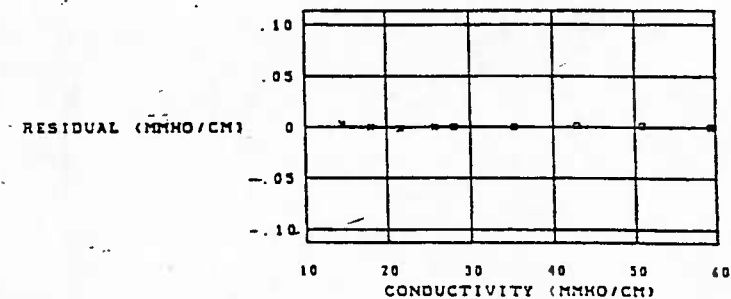


Table B-3 Calibration constants for the SBE conductivity meter.

spiking is discussed further in Appendix C.

One of the aims of the engineering cruise of FLIP in May 1983 was to test the newly acquired SBE system. It performed very well both electrically and mechanically. On return to Scripps, the data collected were analyzed to determine if any improvements could be made. A disturbing feature became apparent after performing a fall rate analysis of the pressure signal. Fig. B-5 shows the unacceptably large variance associated with the first difference of this signal. The cause of the problem was the piece of plastic tubing connecting the pressure port, which is flush with the aluminum casing, to the ambient ocean. The flapping of this tube in the turbulent wake of the temperature sensor housing and the surrounding cage caused the introduction of spurious dynamic pressure effects. The dynamic pressure, P , can be modelled as:

$$P = \frac{1}{2}\rho(\langle u \rangle + u')^2$$

where $\langle u \rangle$ is the mean speed of the package and u' is the component due to turbulence. u'^2 can be significant in the case where the tube is flapping about in a turbulent wake.

The problem was corrected before MILDEX by replacing the plastic tube with a longer rigid metal one which protruded out beyond the temperature probe. The open end of the tube was capped and four small holes drilled into its side close to this end. In this way the effects of dynamic pressure due both to mean speed and turbulence were reduced.

These changes greatly improved the quality of the pressure data which can be seen in Fig. B-6 which shows a typical profile of fall speed from the 1983 experiment.

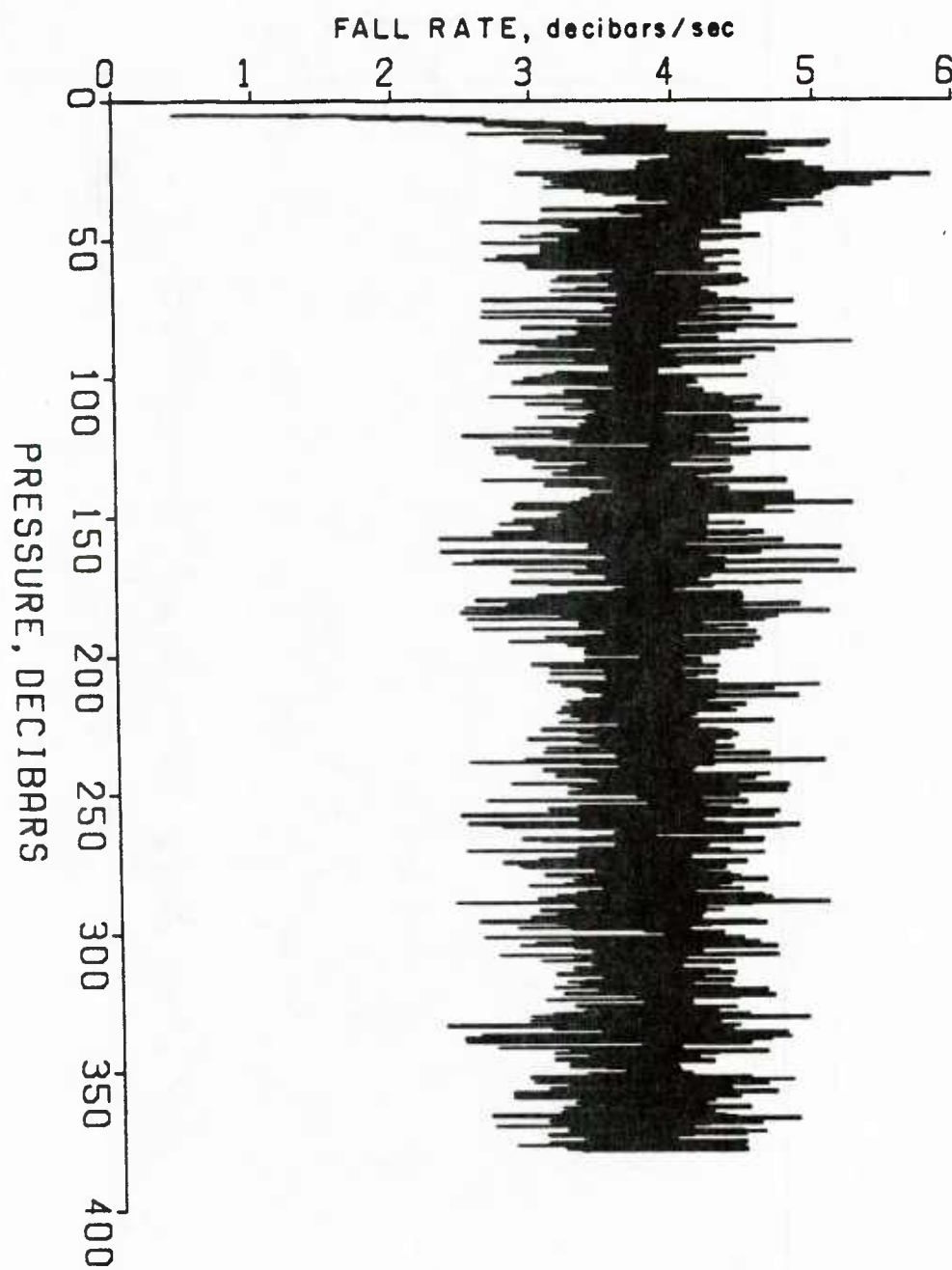


figure B-5 First difference of a pressure signal obtained during the May 1983 FLIP cruise.

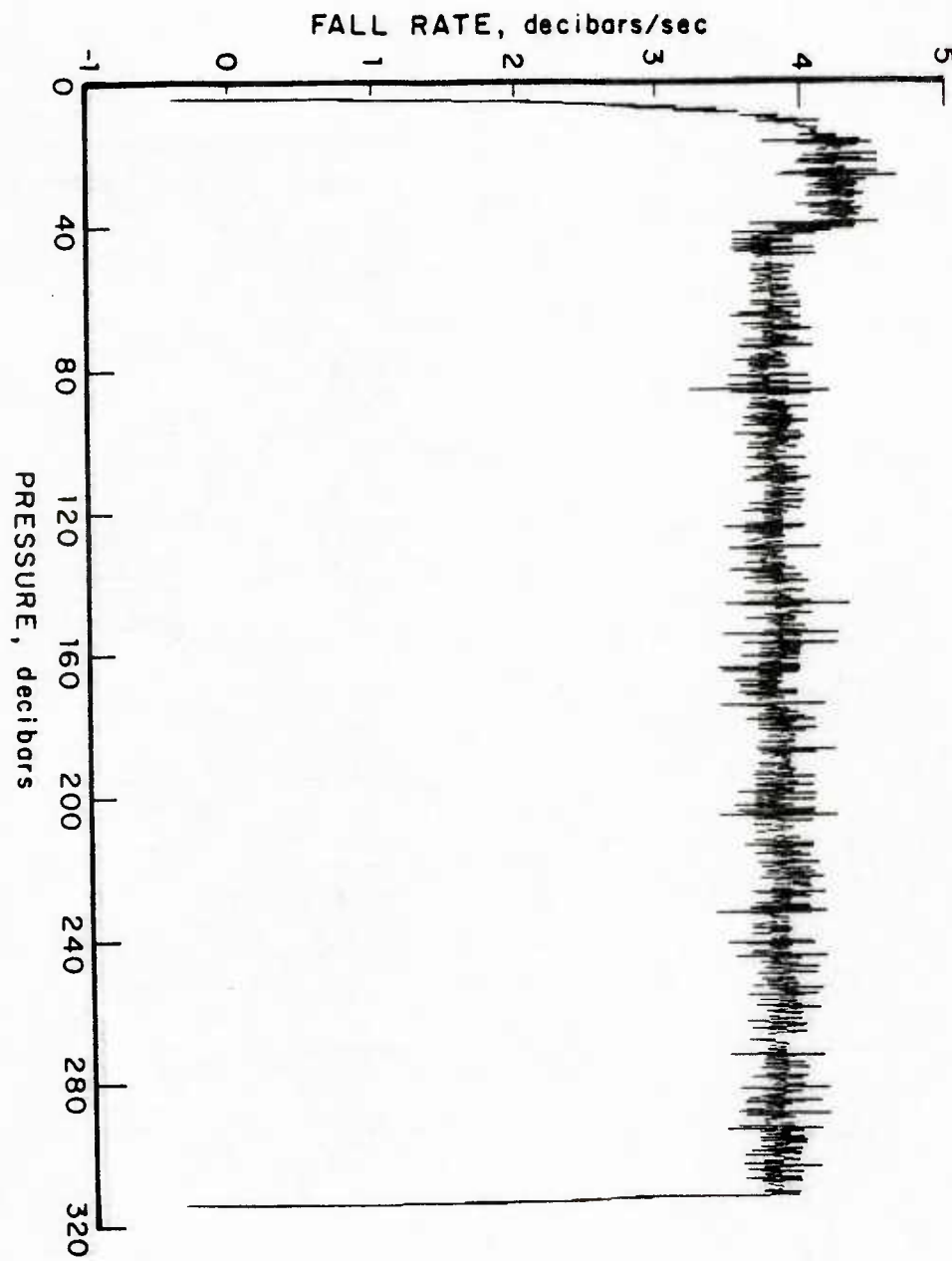


figure B-6 First difference of a pressure signal obtained during MILDEX in October 1983.

APPENDIX C

DIGITAL CORRECTION METHODS USED FOR SBE CONDUCTIVITY AND TEMPERATURE DATA

A common problem experienced with CTD systems is that differences in frequency response between temperature and conductivity sensors can cause spurious spiking to occur in salinity profiles. This problem was also experienced with data collected by the SBE system. This appendix describes an attempt to correct for this error by using digital signal processing techniques.

It should be noted that only *uncorrected* profiles were used for the analyses described in this thesis. It is considered worthwhile, however, to include this appendix as it describes the response characteristics of the SBE sensors operated under very unique conditions: FLIP's profiling system operates at very fast but, nevertheless, controlled speeds of up to 4 m/sec.

As an example of salinity spiking, see Fig. C-1. The spiking can be seen in the halocline between 40 and 80 meters. After the signal processing technique (to be described) had been applied, most of this kind of spiking in the profiles was removed. Fig. C-2 shows the corrected version of the profile presented in Fig. C-1. Much of the spiking has been removed and the complicated structure which remains in the halocline is thought to be due to overturning. Before embarking on a detailed description of the techniques used to achieve these improvements, a brief overview is first presented.

The conductivity cell has a faster response time than the thermister. This leads to differences in frequency response between the conductivity and temperature signals. These differences became progressively worse with increasing frequency (or wavenumber if a simple transformation involving the mean speed of the package is

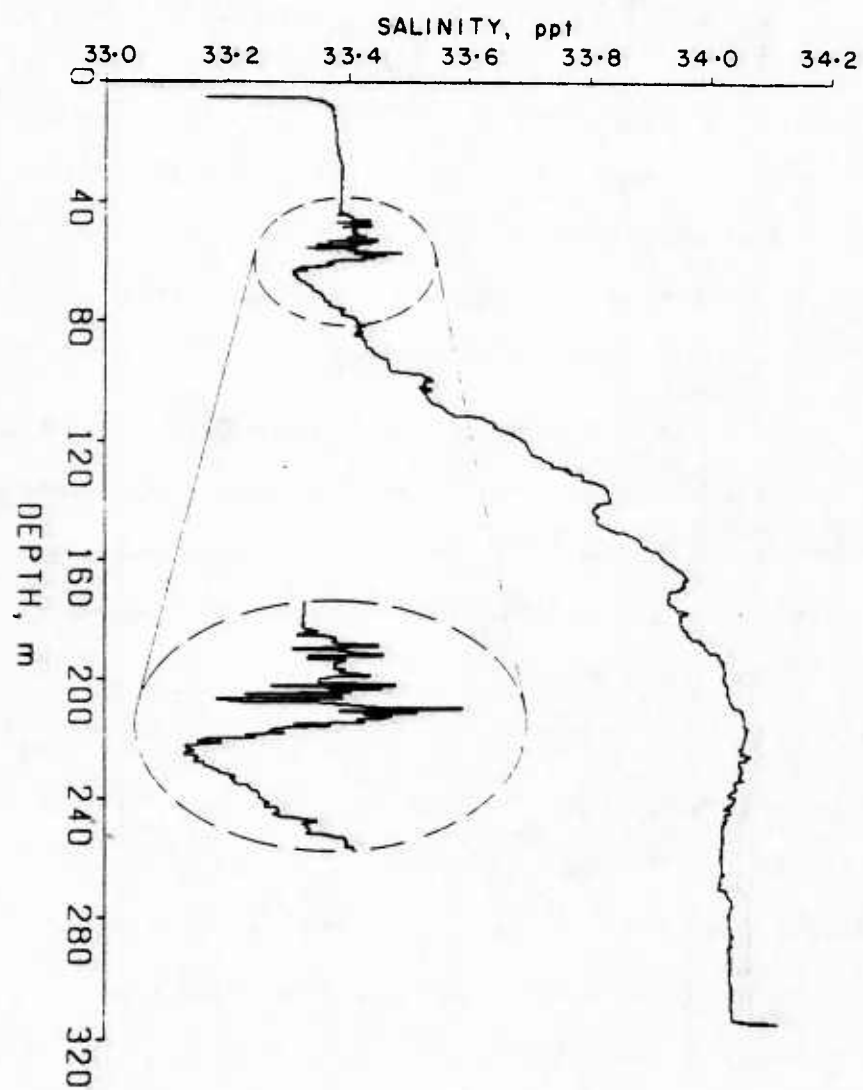


figure C-1 A salinity profile from MILDEX that shows salinity spiking.

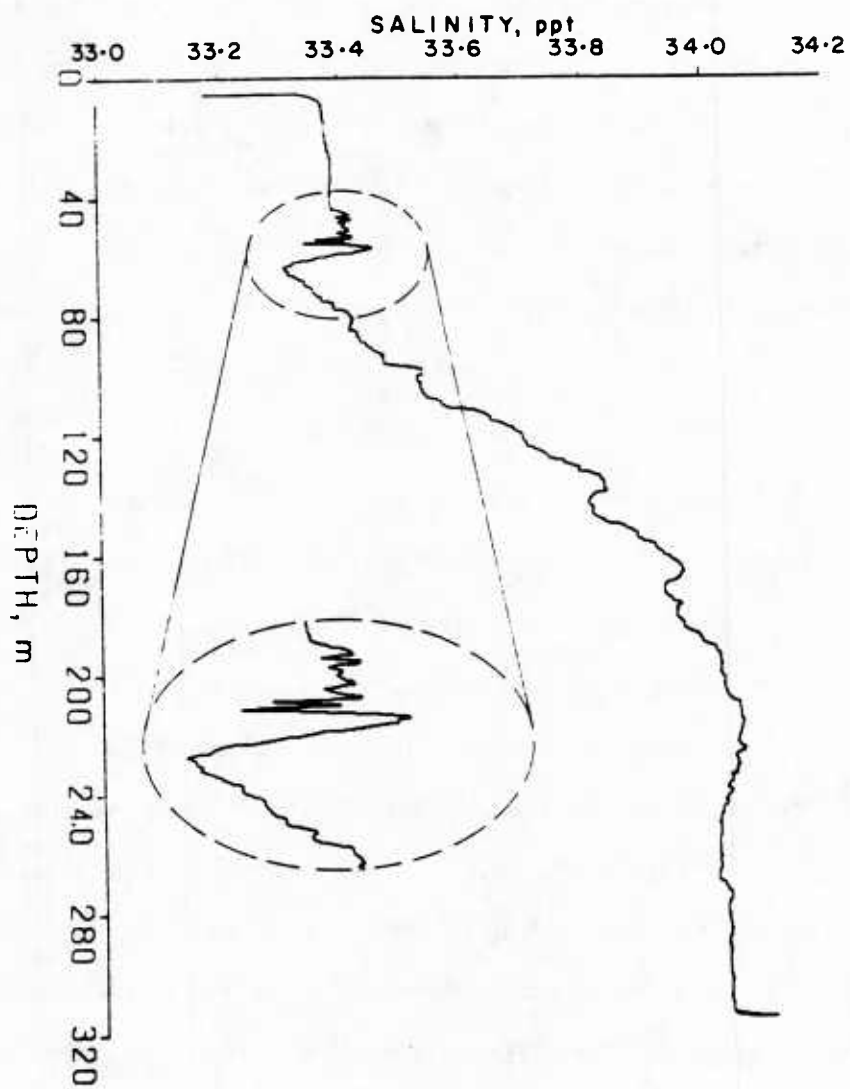


figure C-2 The same salinity profile as shown in figure C-1 after the correction technique has been applied.

implemented). In addition, even though the conductivity cell has better frequency response characteristics than the thermister, it too introduces errors into the signal at higher frequencies (wavenumbers). This latter problem manifests itself as differences in phase between the down and up-cast conductivity profiles. From these differences, phase corrections were calculated and applied to Fourier transforms of downcast $\partial C/\partial z$ profiles. On transforming these back into the spatial domain, more accurate profiles of the "true" conductivity were obtained. Next, the phase and amplitude response differences between the downcast temperature and conductivity signals were calculated. Appropriate corrections were then applied to down-cast temperature data to obtain the "true" temperature profiles.

First, the phase between the down- and up-cast conductivity profiles had to be obtained. Each down- or up-cast profile consists of 1024 points which were first differenced and de-meant, to remove the effect of trend, yielding $\partial C/\partial z$. From Fourier transforms of $\partial C/\partial z$, the average phase between the first 100 down and up-cast conductivity profiles was calculated. The result is shown in Fig. C-3. A similar plot was obtained for a set of 100 profiles collected towards the end of the experiment (Fig. C-4). We see in both figures that the phase becomes extremely noisy beyond about 0.32 cpm (~ 3 meter scale). This is because the upcast information is only good out to 0.32 cpm whereas the downcast information is good out to 1.35 cpm. The reason for the difference is that the CTD system was designed to collect reliable information out to high frequencies only on the downcasts. The average of the two plots shown in Figs C-3 and C-4, was calculated out to 0.32 cpm and the result divided by two (Fig. C-5). A quadratic was fitted to these numbers and extrapolated out to 1.35 cpm (Fig. C-6). The phase values obtained from the fit were added to the phases of $\partial C/\partial z$ on the down-casts and subtracted from the phases of $\partial C/\partial z$ on the up-casts. Fig. C-7 shows the average phase between the first 100 down- and up-cast conduc-

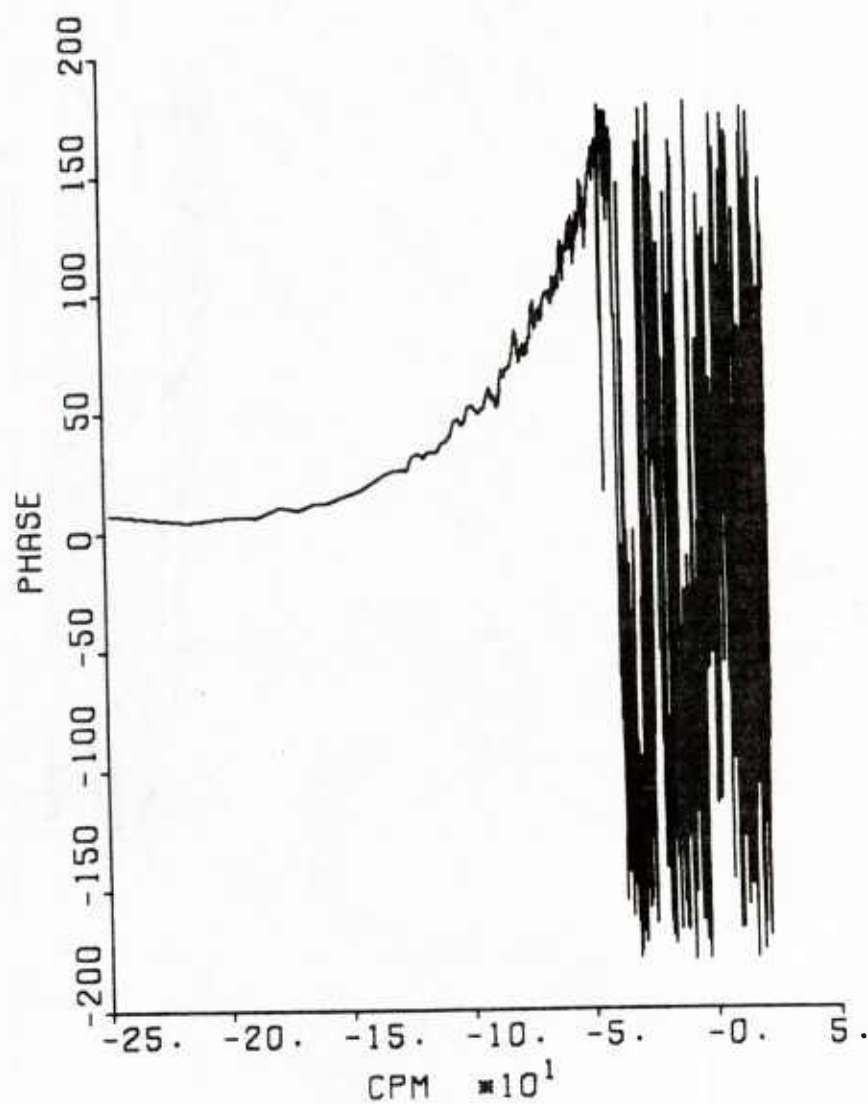


figure C-3 The phase between the downcast and upcast conductivity data, calculated from the first 100 down and upcast profiles. The horizontal scale is logarithmic.

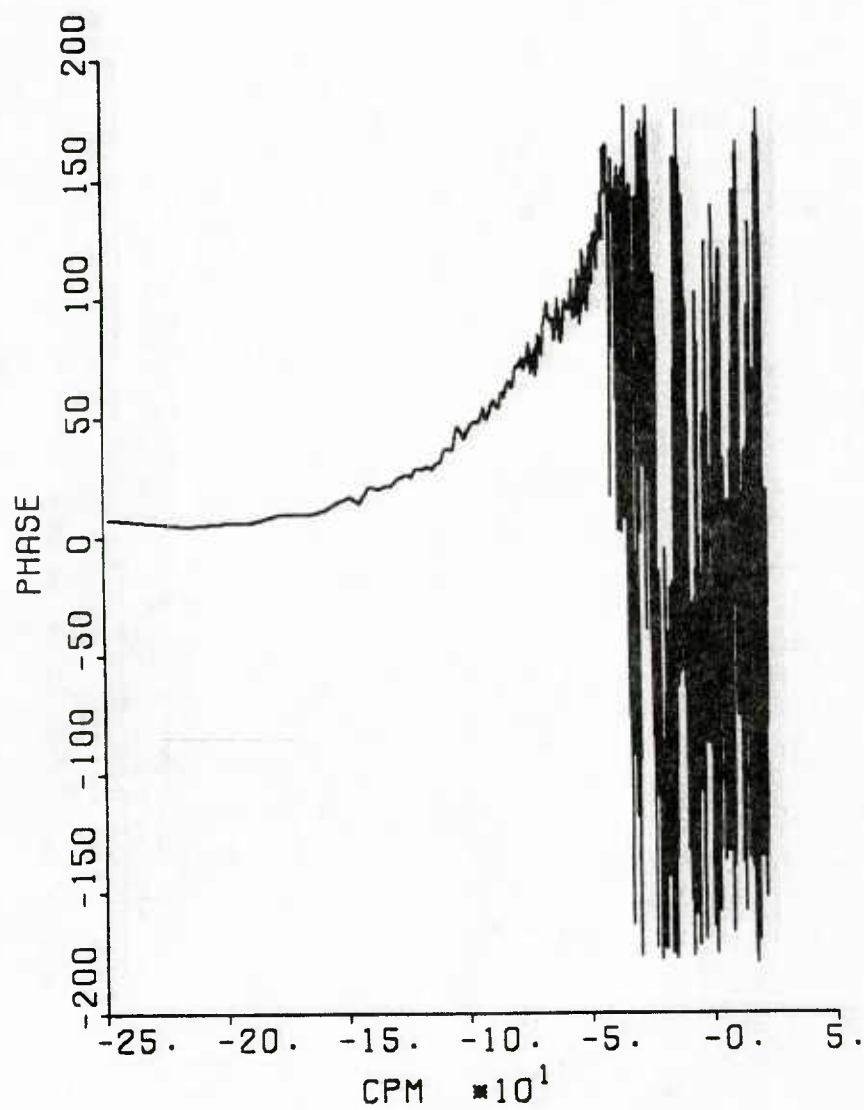


figure C-4 The phase between the downcast and upcast conductivity data, calculated from a set of 100 down and upcast profiles collected towards the end of MILDEX. The horizontal scale is logarithmic.

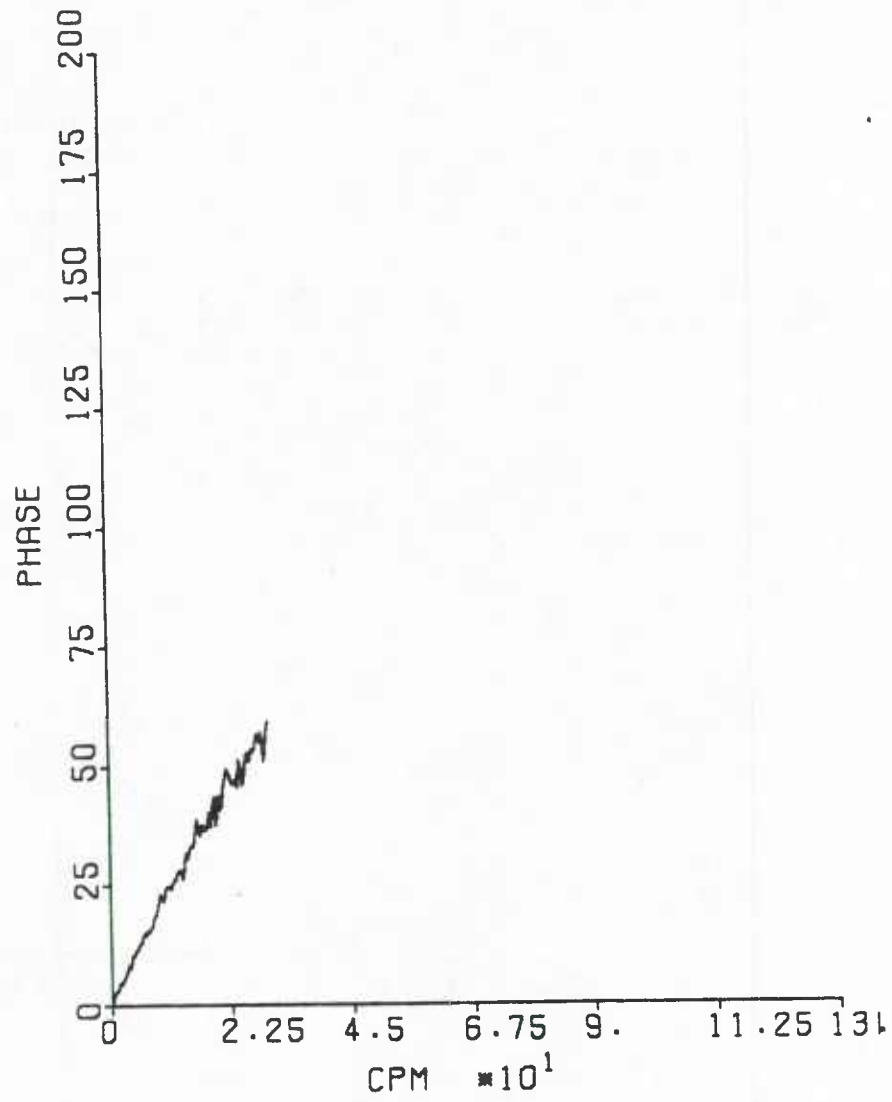


figure C-5 The phase out to 0.32 cpm between the down and upcast conductivity data.

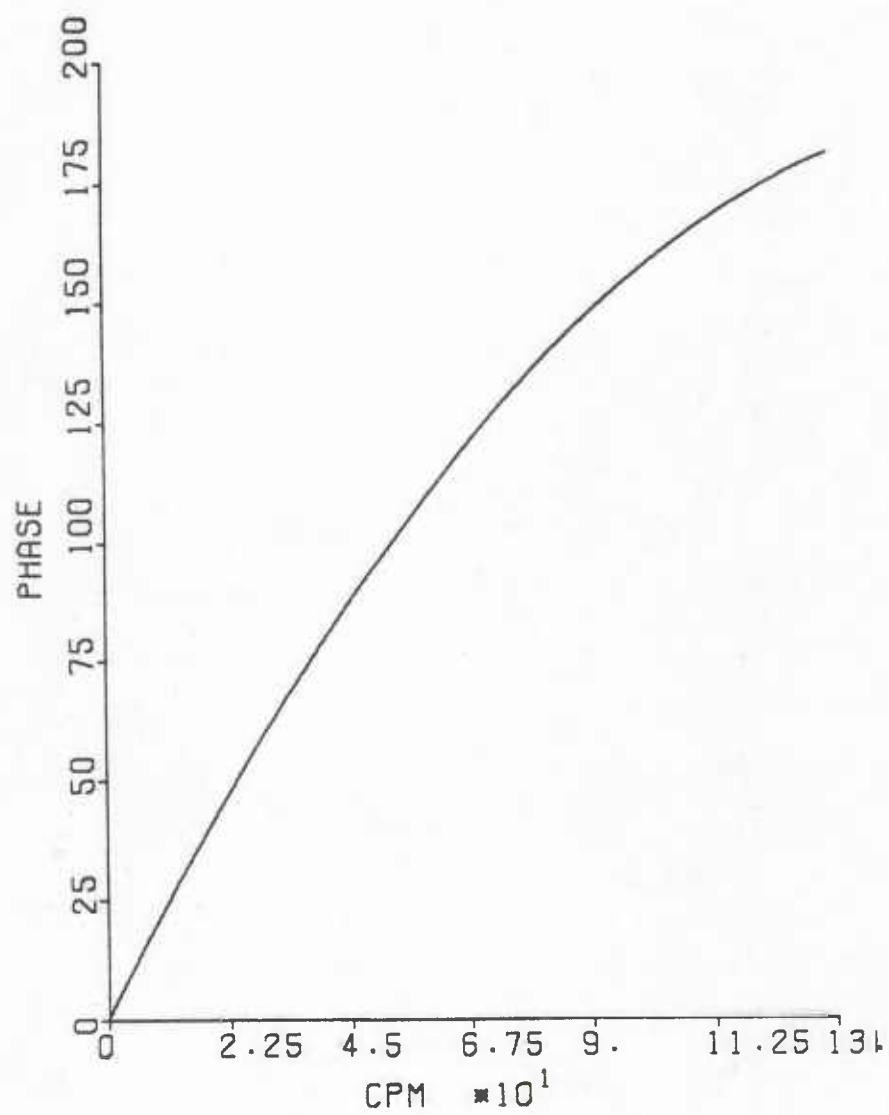


figure C-6 Cubic fit to the phase shown in figure C-5 extrapolated out to 1.35 cpm.

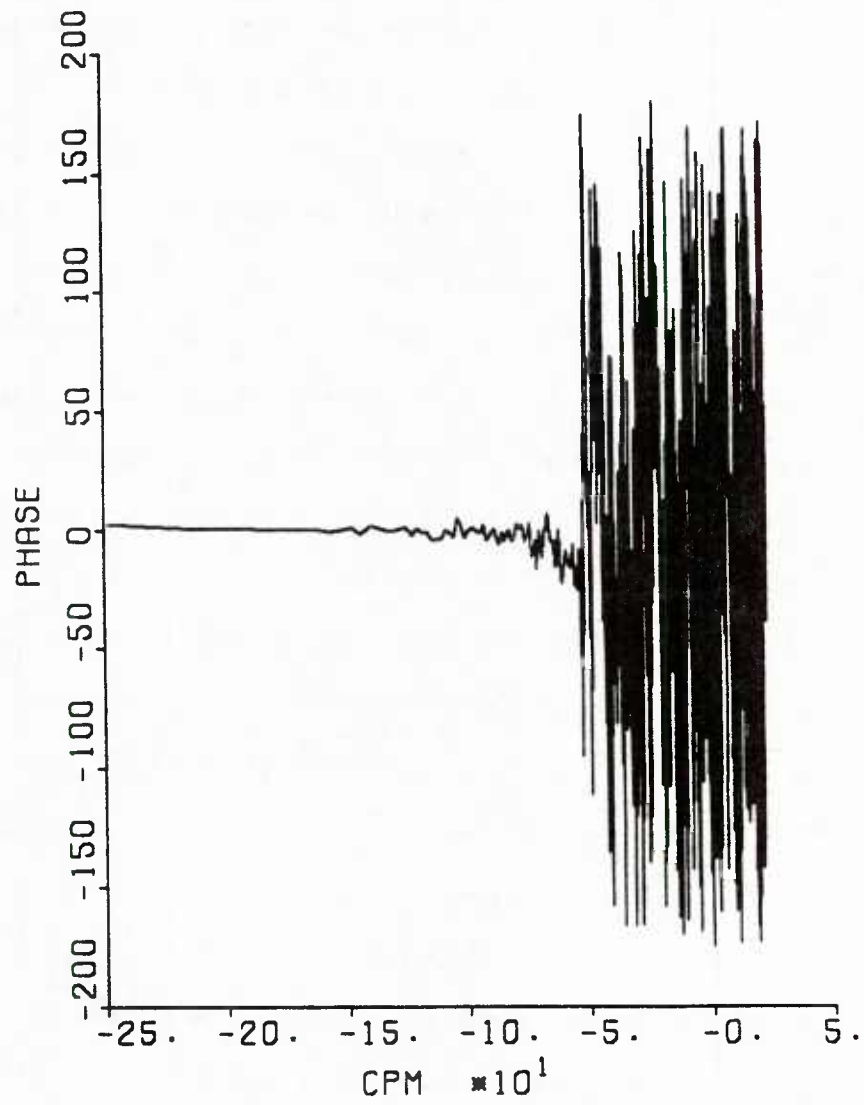


figure C-7 Average phase between downcast and upcast conductivity data after the phase corrections has been applied. The horizontal scale is logarithmic.

tivity profiles after the corrections were applied.

The next step was to calculate the phase and amplitude response corrections for the down-cast temperature profiles. The spectra of $\partial T/\partial z$ and $\partial C/\partial z$ for the first 100 down-cast profiles were calculated and averaged. Figs. C-8 and C-9 show these averaged spectra. Notice that the amplitude response of the thermister begins to roll off at a lower wavenumber than for the conductivity cell. Fig. C-10 shows the average phase between $\partial C/\partial z$ and $\partial T/\partial z$ for the first 100 down-casts and Fig. C-11 the coherence. The minimum in Fig. C-10 occurs at 1.35 cpm where the coherence drops off to approximately 0.8. Very similar plots were obtained for average spectra, phase and coherence calculated for the set of 100 profiles collected towards the end of the experiment. In the light of this information, the decision was made to attempt to correct the phase and amplitude response out to 1.35 cpm and set information associated with higher wavenumbers to zero. Fig. C-12 shows the average value of phase from 0 to 1.35 cpm and Fig. C-13 the corresponding cubic fit. Values of phase obtained from this fit were added to the values of phase of the $\partial T/\partial z$ Fourier coefficients. Fig. C-14 shows the average phase between $\partial T/\partial z$ and $\partial C/\partial z$ for the first 100 down-cast profiles after the corrections had been applied.

In order to apply an amplitude response correction, the square root of the ratio of the power of $\partial T/\partial z$ and $\partial C/\partial z$ was first calculated (Fig. C-15). The plot shows that, beginning at low wavenumbers, the amplitude response of the thermister drops off relative to the amplitude response of the conductivity cell. The reciprocals of the numbers displayed in Fig. C-15 were calculated and normalized by their minimum in the wavenumber range 0.2 to 1.35 cpm. The result is shown in Fig. C-16. A cubic was fitted to these numbers (Fig. C-17). Values of the amplitude of the spectrum of $\partial T/\partial z$ were then multiplied by correction factors calculated from this cubic in the range 0.2 to 1.35 cpm. Figs. C-18 and C-19 show the spectra of $\partial T/\partial z$ and $\partial C/\partial z$

after both the phase and amplitude response corrections had been applied.

After correcting the downcast data by the methods outlined above, it was found that the sharp cut-off at 1.35 cpm in amplitude response caused "ringing" to occur in the corrected profiles. The problem was overcome by including a transition region from 0.5 to 1.35 cpm where the amplitude response for both $\partial T/\partial z$ and $\partial C/\partial z$ was tapered linearly from 1 to 0.

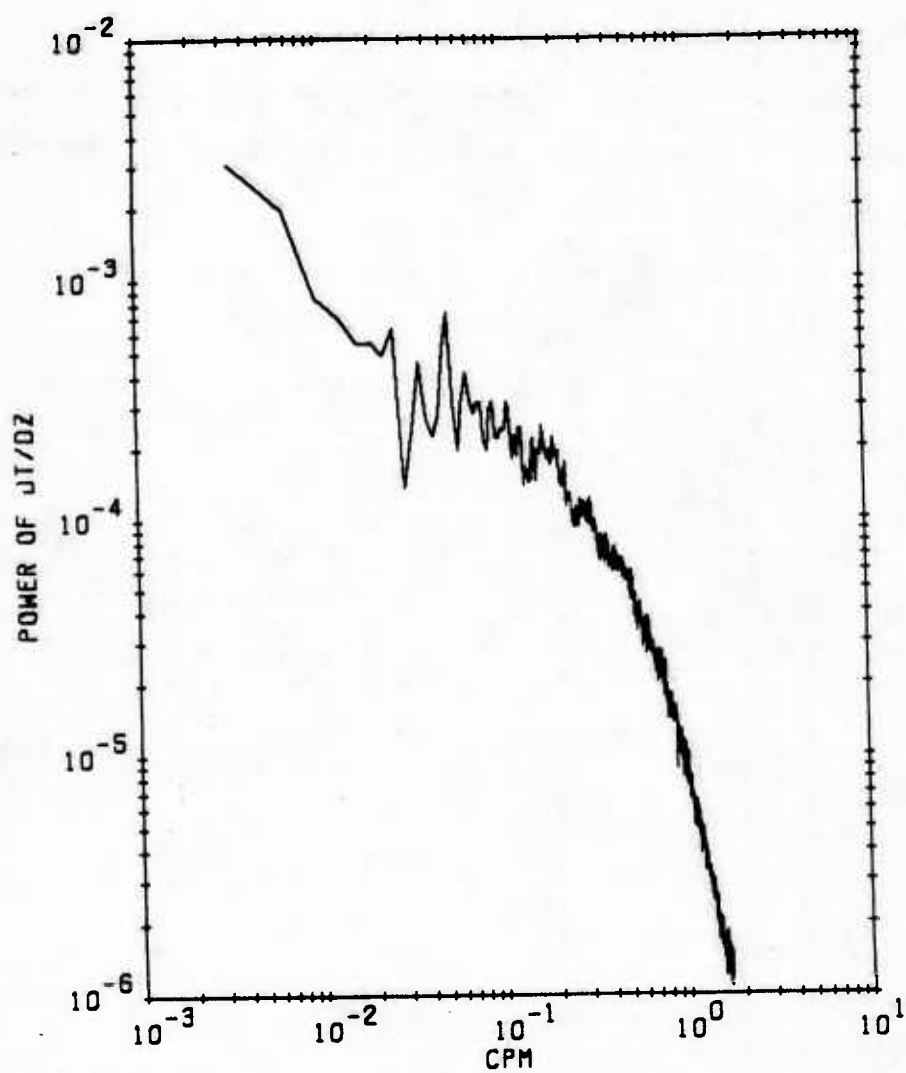


figure C-8 The spectrum of $\frac{\partial T}{\partial z}$ calculated from the first 100 downcast temperature profiles.

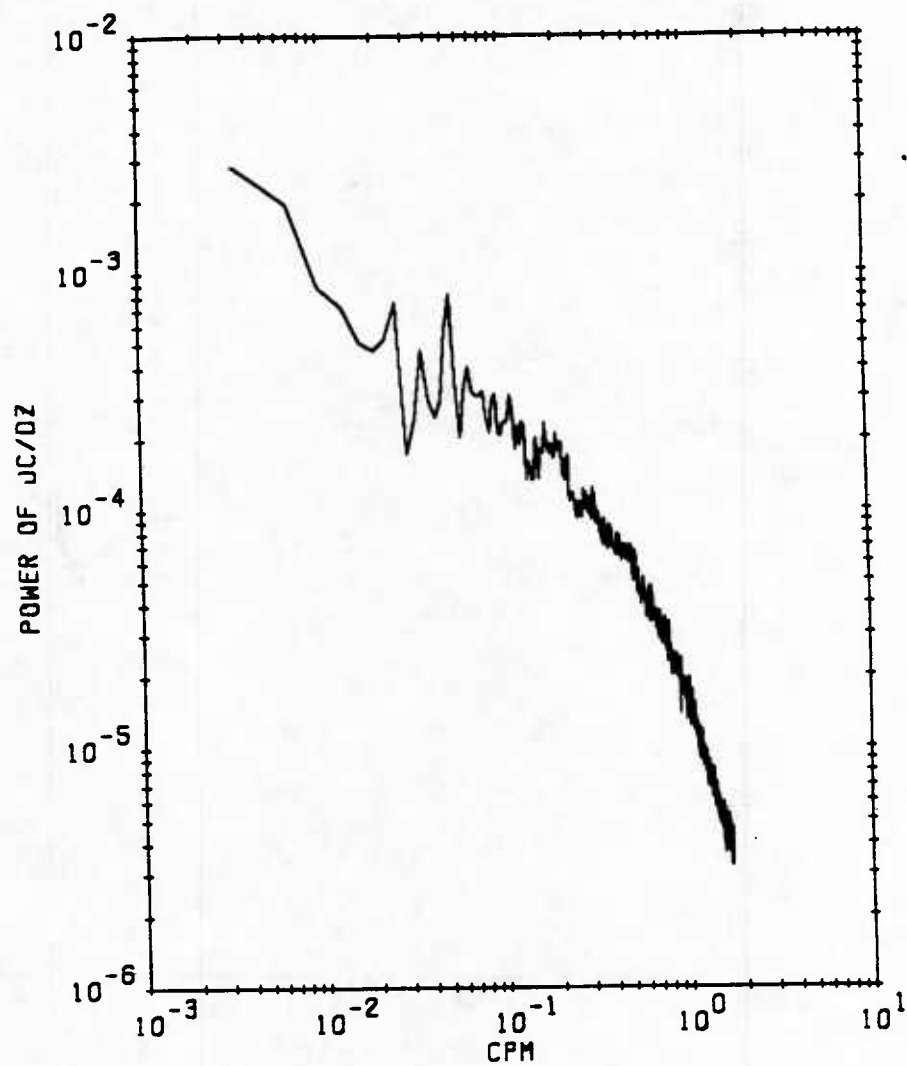


figure C-9 The spectrum of $\frac{\partial C}{\partial z}$ calculated from the first 100 downcast conductivity profiles.

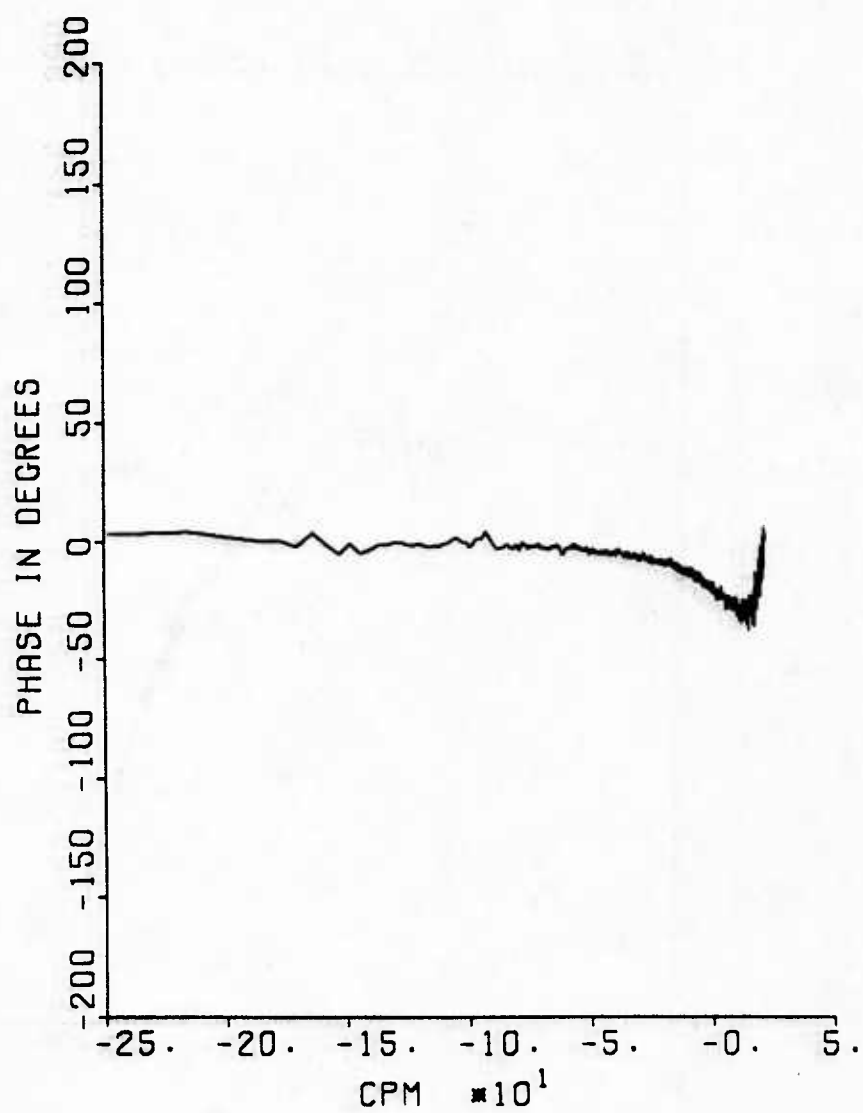


figure C-10 The phase between $\frac{\partial C}{\partial z}$ and $\frac{\partial T}{\partial z}$ calculated from the first 100 downcasts. The horizontal scale is logarithmic.

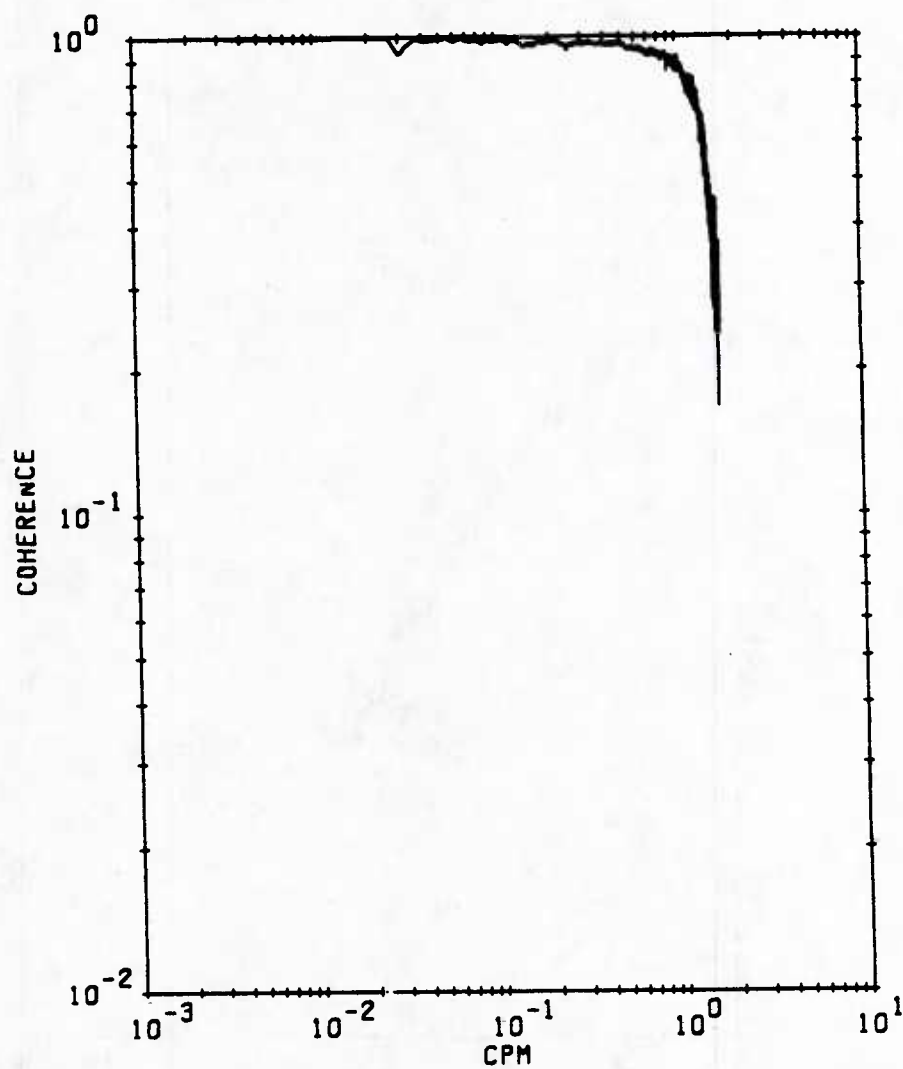


figure C-11 The coherence between $\frac{\partial C}{\partial z}$ and $\frac{\partial T}{\partial z}$ calculated from the first 100 downcasts. The horizontal scale is logarithmic.

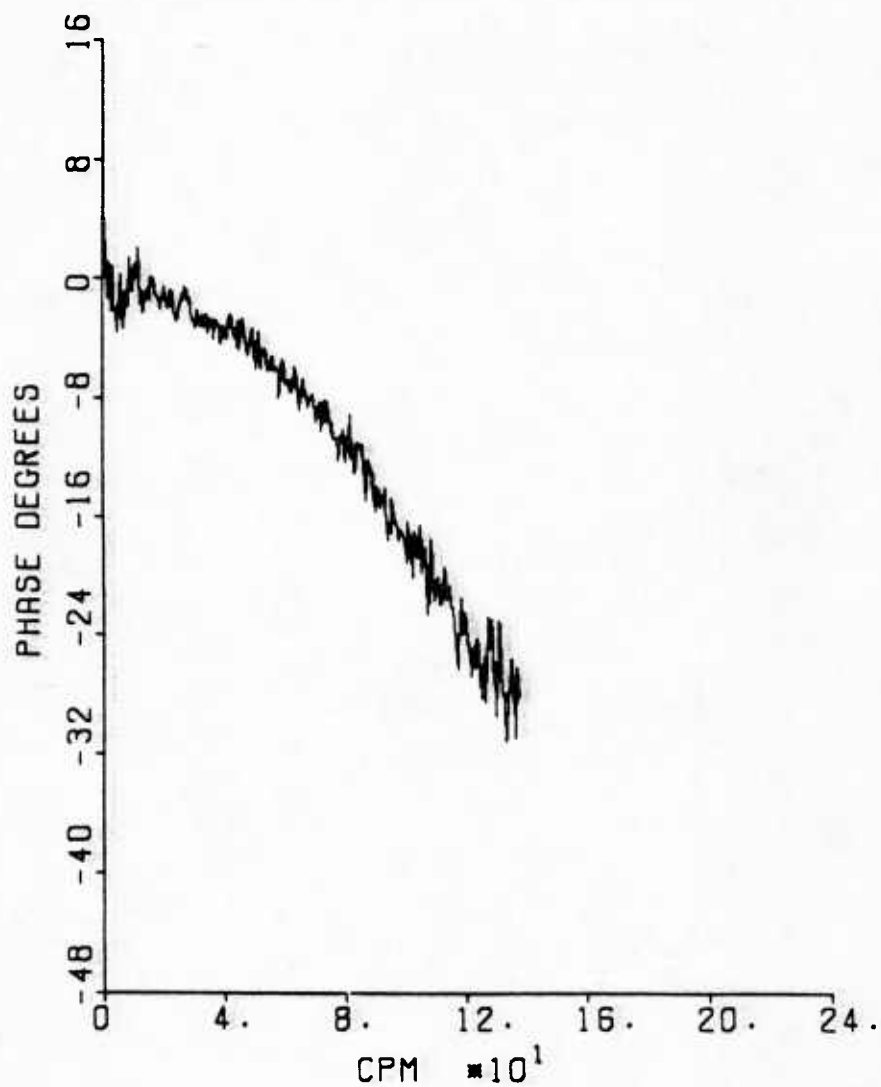


figure C-12 The phase out to 1.35 cpm between $\frac{\partial C}{\partial z}$ and $\frac{\partial T}{\partial z}$ calculated from the first 100 downcasts. The horizontal scale is logarithmic.

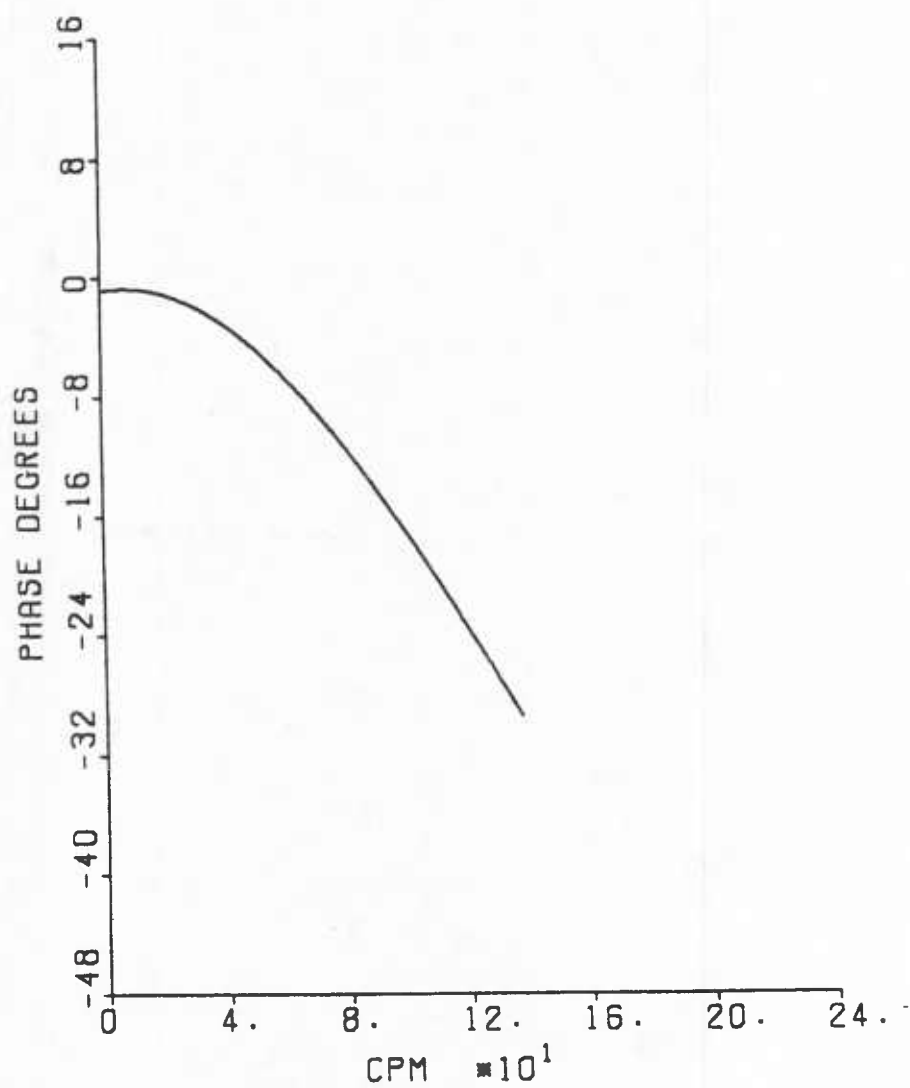


figure C-13 Cubic fit to the phase shown in figure C-12.

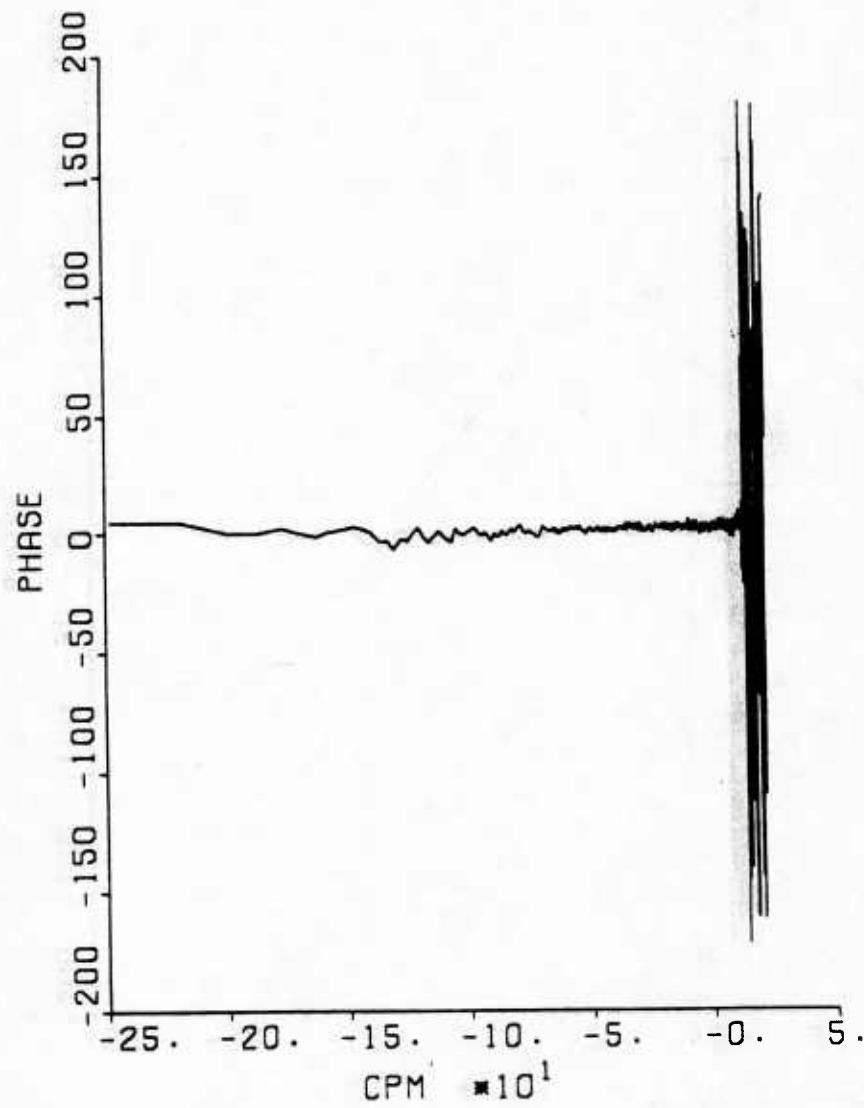


figure C-14 The phase between $\frac{\partial C}{\partial z}$ and $\frac{\partial T}{\partial z}$ calculated from the first 100 downcasts after the phase correction has been applied. The horizontal scale is logarithmic.

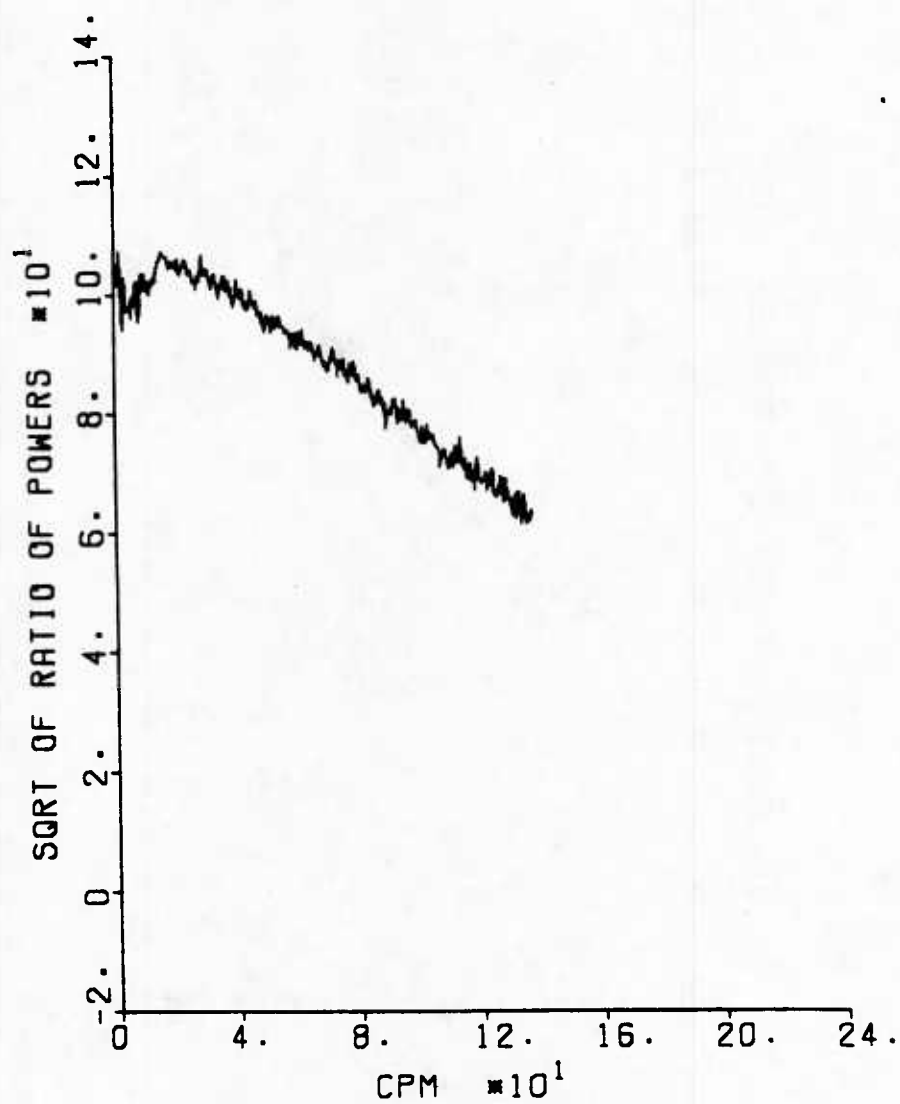


figure C-15 The ratio of the amplitude response between $\frac{\partial C}{\partial z}$ and $\frac{\partial T}{\partial z}$ out to 1.35 cpm, calculated from the first 100 downcasts.

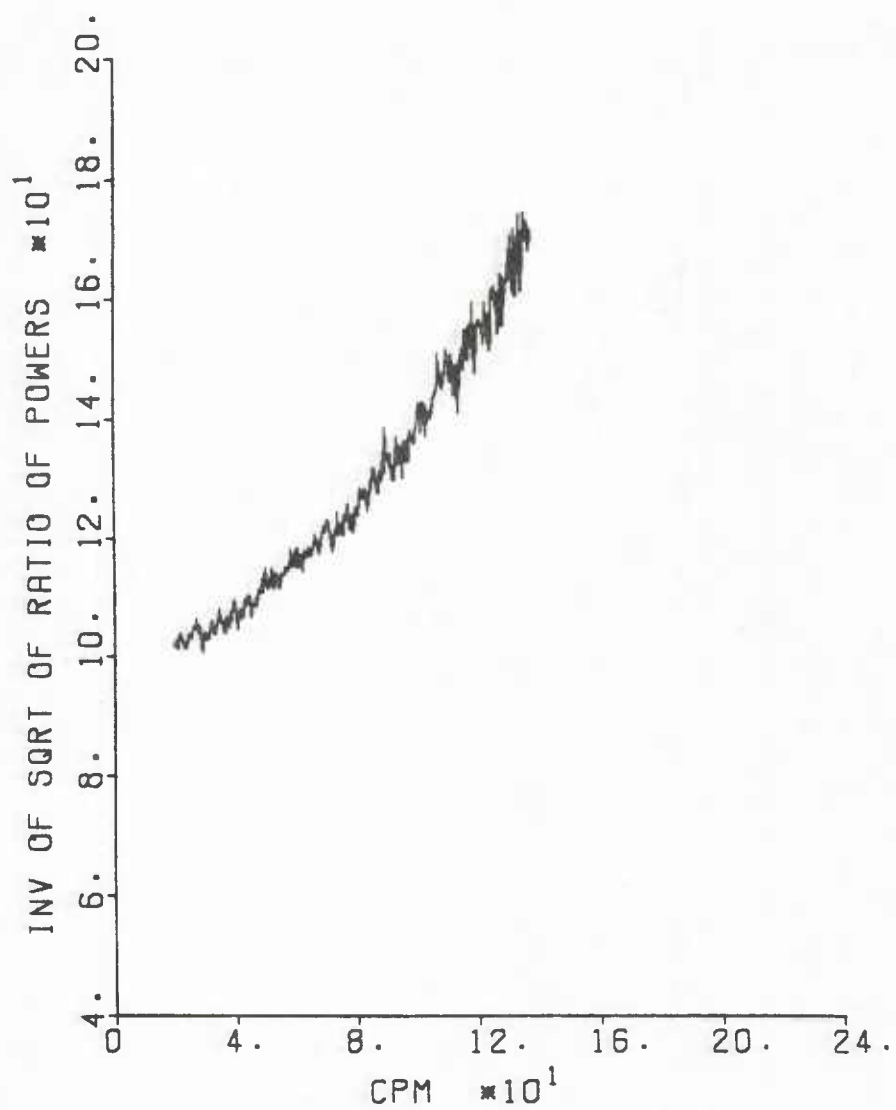


figure C-16 The reciprocals of the numbers plotted in figure C-15 normalized with their minimum.

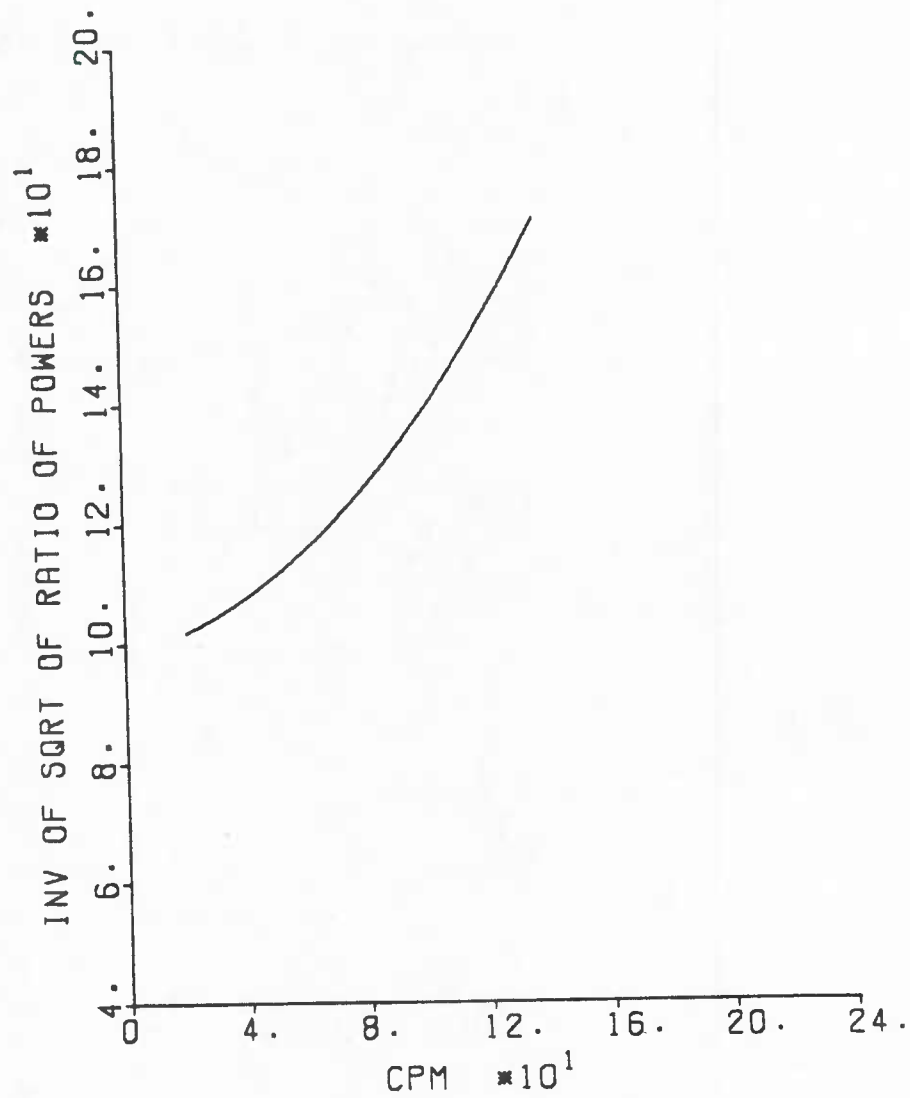


figure C-17 Cubic fit to the numbers plotted in figure C-16.

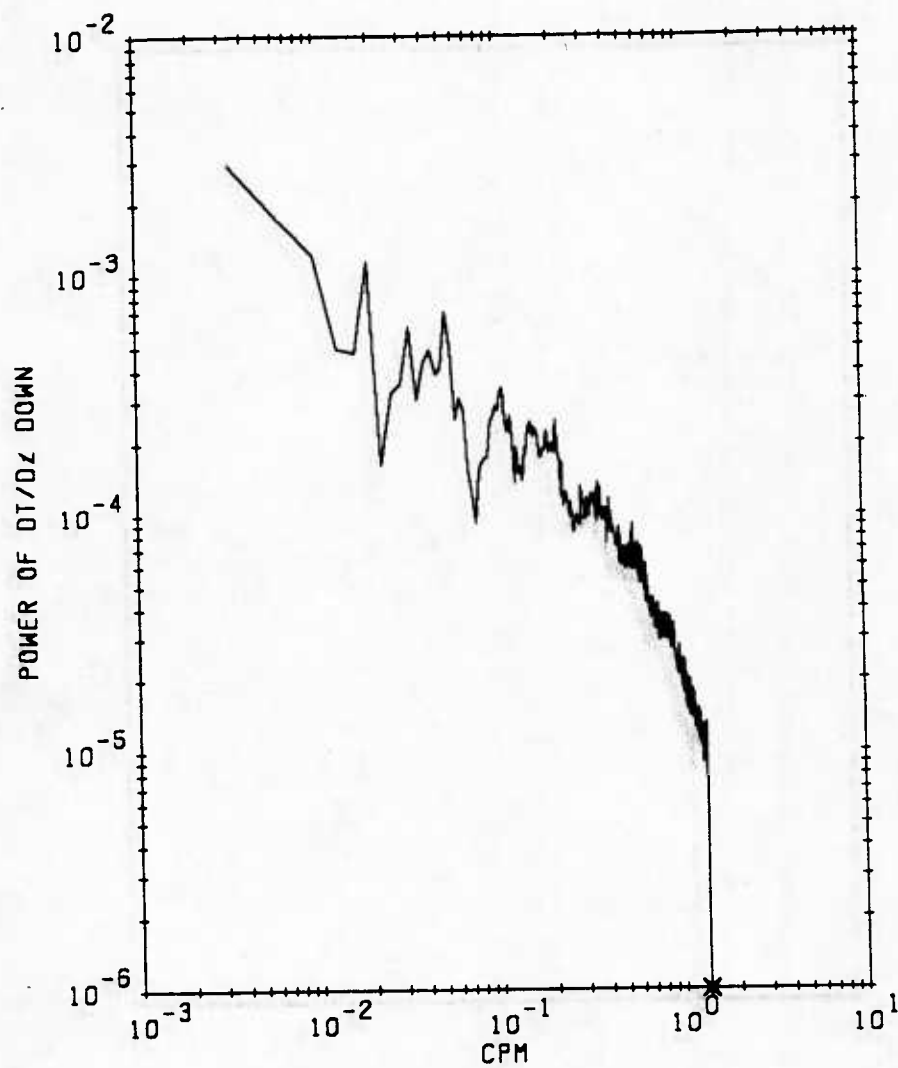


figure C-18 The spectrum of $\frac{\partial T}{\partial z}$ calculated from the first 100 downcasts after the corrections have been applied.

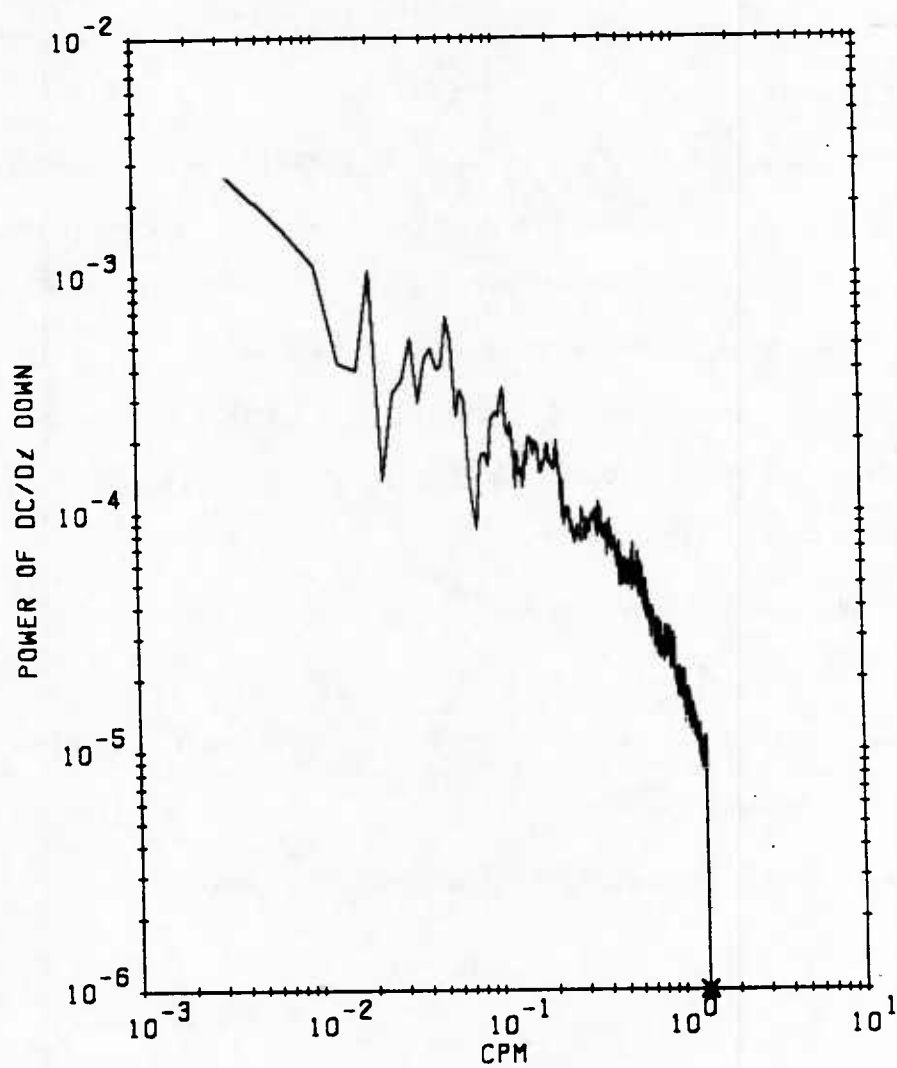


figure C-19 The spectrum of $\frac{\partial C}{\partial z}$ calculated from the first 100 downcasts after the corrections have been applied.

APPENDIX D

BISPECTRAL ANALYSIS COMPUTATIONAL PROCEDURES

This appendix describes the computational procedures used to calculate the bispectra and bicoherence spectra presented in Chapter 5.

In the section entitled "Bispectral Analysis" in Chapter 5, the symmetry conditions for bispectra are presented. The important consequence of these relations is that the bispectrum is uniquely defined over the triangular area shown in Fig. D-1, which is the region over which estimates are typically calculated.

We assume that the process $x(t)$ is band-limited and that the sampling interval Δt is sufficiently small that the Nyquist frequency $f_N = 1/(2\Delta t)$ is larger than any spectral component of interest present in $x(t)$.

The computational procedures are as follows.

- 1) Form M sets of data records of length N . $x^{(j)}(l)$, $j = 1, \dots, M$ and $l = 1, \dots, N$ where $x(l) = x(l\Delta t)$. In our case each record is an isopycnal.
- 2) Remove the trend from each record.
- 3) Compute the Fourier amplitudes using the FFT technique.

$$X_k^{(j)} = \sum_{l=1}^N x^{(j)}(l) e^{-i2\pi kl/N},$$

$$k = 1, \dots, N/2 \text{ and } j = 1, \dots, M.$$

- 4) Calculate the bispectral estimates.

$$\hat{B}(k, l) = \frac{1}{M} \sum_{j=1}^M X_k^{(j)} X_l^{(j)} X_{k+l}^{*(j)}$$

where " $\hat{}$ " denotes estimator. In our case this operation corresponds to averaging bispectra over a depth range.

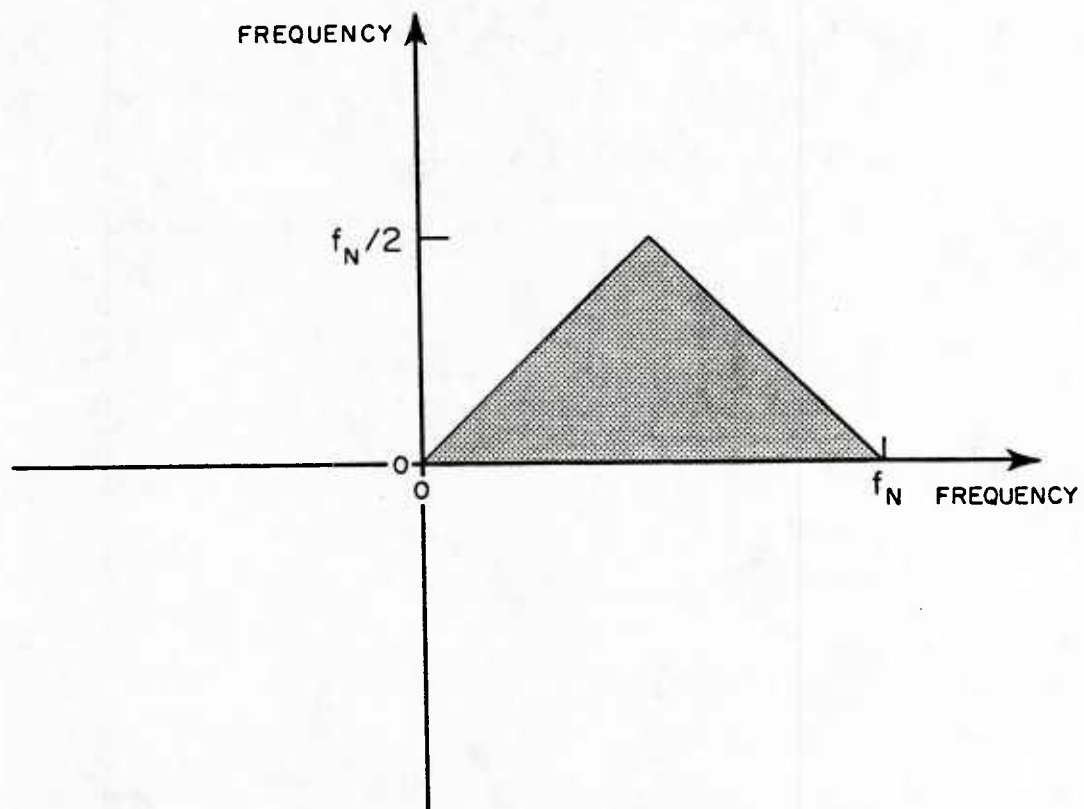


figure D-1 The triangular region over which the auto-bispectrum is completely defined. f_N denotes the Nyquist frequency.

- 5) Normalize the bispectral estimates by dividing with $(2\pi)^2 N$ as recommended by Lii and Helland (1981).
- 6) Calculate the bicoherence spectral estimates.

$$\hat{b}(k, l) = \frac{|\hat{B}(k, l)|}{\left[\frac{1}{M} \sum_{j=1}^M |X_k^{(j)} X_l^{(j)}|^2 \right]^{1/2} \left[\frac{1}{M} \sum_{j=1}^M |X_{k+l}^{(j)}|^2 \right]^{1/2}}$$

- 7) Average the bispectral estimates over a square region in the frequency-frequency domain. For the bispectra presented in Chapter 5 a square region 7×7 frequency bins in extent was chosen.
- 8) Calculate the bicoherence spectral estimates which correspond to the bispectral estimates calculated in 7) above.

APPENDIX E

FLIP'S DOPPLER SONAR SYSTEM

The intention in this appendix is to give the reader a brief description of FLIP's doppler sonar system. A more detailed account can be found in Pinkel (1980).

Figures 2-2 and 2-5 in Chapter 2 show the configuration of the sonar beams during the 1980 and 1983 experiments. During both cruises the downward looking beams were configured at right angles to each other so that orthogonal components of current velocity could be measured.

The transmitted signal is typically in the range 67-85 kHz. It is backscattered from biota in the water column returning a signal which is Doppler shifted in frequency. The amount of Doppler shifting depends upon the component of current velocity parallel to the beam. By inverting this relationship, current velocity can be calculated.

The essential features of the system hardware are shown in Fig. E-1. The transmitted and received signals for time t are modelled respectively as:

$$R_o(t) = Ae^{i\Omega_o t}$$
$$\text{and } R(t) = e^{i\Omega_o t} \sum_{V_t} a_m e^{-ik2r_m}$$

where

A = amplitude of the transmitted signal.

Ω_o = carrier frequency.

k = wavenumber corresponding to frequency Ω_o .

$2r_m$ = round trip distance to m th scatterer.

a_m = scattering amplitude of m th scatterer.

V_t = scattering volume corresponding to time t .

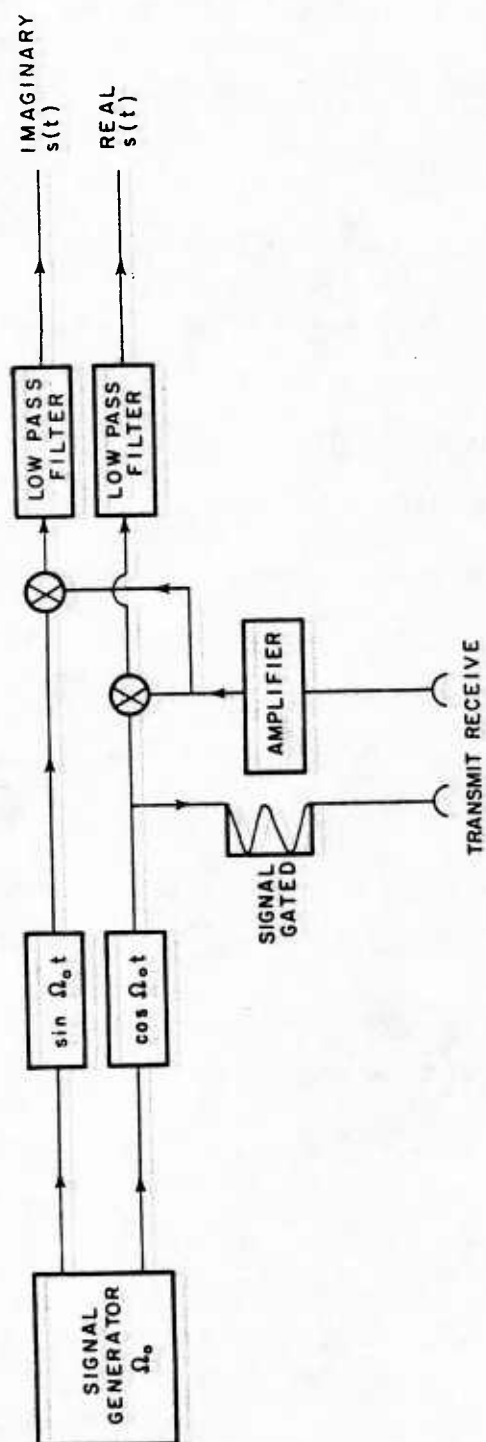


figure E-1 Schematic of FLIP's Doppler sonar system hardware.

The carrier frequency in the return echo is removed by complex base-banding to leave

$$S(t) = \sum_{V_t} a_m e^{-ik2r_m}$$

Now consider the corresponding signal for a time, τ , later

$$S(t + \tau) = \sum_{V_{t+\tau}} a_n e^{-ik(2r_n + 2v\tau)}$$

where $V_{t+\tau}$ is a slightly different, but overlapping, scattering volume due to the time delay and v is the velocity of the scatterers parallel to the sonar beam. As the range cells overlap, most of the scatterers in $V_{t+\tau}$ are the same as those in V_t . The autocovariance function is formed from

$$\begin{aligned} S(t)S^*(t + \tau) &= \sum_{V_t} \sum_{V_{t+\tau}} a_m a_n e^{-ik(2r_m - 2r_n - 2v\tau)} \\ &= e^{2ikv\tau} \sum_{V_t} \sum_{V_{t+\tau}} a_m a_n e^{-ik(2r_m - 2r_n)} \end{aligned}$$

Averaging over many realizations, the resulting contribution is from the common volume ($m = n$).

$$\langle S(t)S^*(t + \tau) \rangle = e^{2ikv\tau} \sum_{V_{common}} \langle a_m^2 \rangle$$

and the only contribution to the phase is from $e^{2ikv\tau}$. Therefore

$$\langle \phi \rangle = 2kv\tau = \tan^{-1} \left[\frac{\text{Im}\{\langle S(t)S^*(t + \tau) \rangle\}}{\text{Re}\{\langle S(t)S^*(t + \tau) \rangle\}} \right]$$

$$v = \tan^{-1} \frac{\left[\frac{\text{Im}\{\langle S(t)S^*(t + \tau) \rangle\}}{\text{Re}\{\langle S(t)S^*(t + \tau) \rangle\}} \right]}{2k\tau}$$

For the 1983 data, 3 minute average profiles with a range resolution of 11 m were recorded. Typical ranges achieved were ~ 1500 m.

APPENDIX F

PRINCIPAL AXES OF A VECTOR FIELD

Given a two dimensional zero mean vector field defined on the Cartesian co-ordinate system (u, v) (see Figure F-1), we wish to find θ such that the same vector field when defined on the new rotated co-ordinate system (u', v') given by:

$$u' = u \cos\theta + v \sin\theta$$

$$v' = -u \sin\theta + v \cos\theta$$

minimizes $\sigma_{u'}^2$, maximizes $\sigma_{v'}^2$ and minimizes $C_{u'v'}$ where

$$\sigma_{u'}^2 = \langle u'^2 \rangle = \langle u^2 \rangle \cos^2\theta + \langle v^2 \rangle \sin^2\theta + 2 \cos\theta \sin\theta \langle uv \rangle$$

$$\sigma_{v'}^2 = \langle v'^2 \rangle = \langle u^2 \rangle \sin^2\theta + \langle v^2 \rangle \cos^2\theta - 2 \cos\theta \sin\theta \langle uv \rangle$$

$$C_{u'v'} = \langle u'v' \rangle = \cos\theta \sin\theta [-\langle u^2 \rangle + \langle v^2 \rangle] + \langle uv \rangle [\cos^2\theta - \sin^2\theta]$$

In the case where the end points of the vectors form an ellipse, the major axis will lie in the direction of u' and the minor axis will lie in the direction of v' .

$$\frac{\partial \sigma_{u'}^2}{\partial \theta} = 0, \frac{\partial \sigma_{v'}^2}{\partial \theta} = 0 \text{ and } C_{u'v'} = 0 \text{ all lead to the same equation}$$

$$\tan 2\theta = \frac{2\langle uv \rangle}{\langle u^2 \rangle - \langle v^2 \rangle} \quad \text{for } \langle u^2 \rangle \neq \langle v^2 \rangle$$

$$\theta = \frac{\pi}{4}, \frac{3\pi}{4}, \dots \quad \text{for } \langle u^2 \rangle = \langle v^2 \rangle.$$

Thus the rotation θ which extremizes $\sigma_{u'}^2$ also extremizes $\sigma_{v'}^2$ and results in uncorrelated u' and v' .

We seek the value of θ which maximizes $\sigma_{u'}^2$ and minimizes $\sigma_{v'}^2$, i.e. we seek θ such that $\frac{\partial^2 \sigma_{u'}^2}{\partial \theta^2} < 0$ and $\frac{\partial^2 \sigma_{v'}^2}{\partial \theta^2} > 0$. Two cases are considered.

1. If $\langle u^2 \rangle = \langle v^2 \rangle$.

$$\frac{\partial^2 \sigma_{\Psi'}^2}{\partial \theta^2} = -8 \langle uv \rangle \cos \theta \sin \theta$$

If $\langle uv \rangle > 0$, $\theta = \frac{\pi}{4}$ results in a maximum of $\sigma_{\Psi'}^2$, which is given by:

$$\sigma_{\Psi'}^2 = \frac{1}{2} [\langle u^2 \rangle + \langle v^2 \rangle] + \langle uv \rangle$$

However, if $\langle uv \rangle < 0$, $\theta = \frac{3\pi}{4}$ results in a maximum of $\sigma_{\Psi'}^2$, which is given by:

$$\sigma_{\Psi'}^2 = \frac{1}{2} [\langle u^2 \rangle + \langle v^2 \rangle] - \langle uv \rangle$$

If $\langle uv \rangle = 0$ then any θ is equally good

In general the maximum of $\sigma_{\Psi'}^2$ is given by:

$$\frac{1}{2} [\langle u^2 \rangle + \langle v^2 \rangle] + |\langle uv \rangle|$$

Similarly the minimum of $\sigma_{\Psi'}^2$ is given by:

$$\frac{1}{2} [\langle u^2 \rangle + \langle v^2 \rangle] - |\langle uv \rangle|$$

$$\text{with } \theta = \frac{\pi}{2} - \frac{\pi}{4} \left(\text{sign } \{ \langle uv \rangle \} \right)$$

2. If $\langle u^2 \rangle \neq \langle v^2 \rangle$

$$\frac{\partial^2 \sigma_{\Psi'}^2}{\partial \theta^2} = 2[\cos^2 \theta - \sin^2 \theta] \left\{ [\langle v^2 \rangle - \langle u^2 \rangle] + \frac{4\langle uv \rangle^2}{\langle v^2 \rangle - \langle u^2 \rangle} \right\}$$

Now $\text{sign } \{ \} = \text{sign } [\langle v^2 \rangle - \langle u^2 \rangle]$. We want $\frac{\partial^2 \sigma_{\Psi'}^2}{\partial \theta^2} < 0$. Therefore

$$\text{if } \langle v^2 \rangle > \langle u^2 \rangle \text{ we pick } |\theta - \frac{\pi}{2}| < \frac{\pi}{4}$$

$$\text{if } \langle v^2 \rangle < \langle u^2 \rangle \text{ we pick } |\theta| < \frac{\pi}{4}$$

Now we know the solution for θ satisfies

$$\tan 2\theta = \frac{2\langle uv \rangle}{\langle u^2 \rangle - \langle v^2 \rangle}$$

and $\cos 2\theta = \pm \{1 + \tan^2 2\theta\}^{-1/2}$. Choose + sign if $|\theta| < \frac{\pi}{4}$ or - sign if $|\theta - \frac{\pi}{2}| < \frac{\pi}{4}$.

It can be shown that:

$$\begin{aligned}\sigma_u^2 &= \frac{1}{2}[\langle u^2 \rangle + \langle v^2 \rangle] + \frac{1}{2} \cos 2\theta [\langle u^2 \rangle - \langle v^2 \rangle] + \sin 2\theta \langle uv \rangle \\ &= \frac{1}{2}[\langle u^2 \rangle + \langle v^2 \rangle] \pm \frac{1}{2}[\langle u^2 \rangle - \langle v^2 \rangle] \left\{ 1 + \frac{4\langle uv \rangle^2}{[\langle u^2 \rangle - \langle v^2 \rangle]^2} \right\}^{1/2}\end{aligned}$$

Note that as $\langle u^2 \rangle - \langle v^2 \rangle \rightarrow 0$, $\sigma_u^2 \rightarrow \frac{1}{2}[\langle u^2 \rangle + \langle v^2 \rangle] \pm \langle uv \rangle$ which is the same result obtained above. From this we see that sign of $\langle u^2 \rangle - \langle v^2 \rangle$ determines the quadrant of θ

$$\text{If } \langle u^2 \rangle > \langle v^2 \rangle, |\theta| < \frac{\pi}{4}$$

$$\text{If } \langle u^2 \rangle < \langle v^2 \rangle, |\theta - \frac{\pi}{2}| < \frac{\pi}{4}$$

The maximum of σ_u^2 is given by

$$\sigma_u^2 = \frac{1}{2}[\langle u^2 \rangle + \langle v^2 \rangle] + \frac{1}{2}|\langle u^2 \rangle - \langle v^2 \rangle| \left\{ 1 + \frac{4\langle uv \rangle^2}{[\langle u^2 \rangle - \langle v^2 \rangle]^2} \right\}^{1/2}$$

Similarly the minimum of σ_v^2 is given by

$$\sigma_v^2 = \frac{1}{2}[\langle u^2 \rangle + \langle v^2 \rangle] - \frac{1}{2}|\langle u^2 \rangle - \langle v^2 \rangle| \left\{ 1 + \frac{4\langle uv \rangle^2}{[\langle u^2 \rangle - \langle v^2 \rangle]^2} \right\}^{1/2}$$

The following subroutine, called PRINA, calculates three parameters from the north and east components of a vector field. These are: the rms variation (RMS), the polarization index (POL) and the angle clockwise from north of the major axis (ANG). The subroutine is based on the preceding mathematical derivations. The polarization index is defined as 1-R where R is the ratio of the minor to the major axis. Thus a value of 1 is obtained for a linearly polarized field and 0 for an isotropic or unpolarized field.

```

RAT4      SUBROUTINE PRINA(U2,U2,UU,RMS,POL,ANG)
# PRINCIPAL AXIS ANALYSIS OF VECTOR QUANTITIES U AND U
# INPUTS:
#   U2 = VARIANCE OF U FIELD (EAST COMPONENT)
#   U2 = VARIANCE OF U FIELD (NORTH COMPONENT)
#   UU = COVARIANCE OF U,U
# OUTPUTS:
#   RMS = RMS VARIATION OF VECTOR MAGNITUDE
#   POL = POLARIZATION INDEX = 0 FOR ISOTROPIC
#           = 1 FOR UNIDIRECTIONAL FIELD
#
#   PIZ=2.*ATAN(1.0)      #PIZ=0.5*PI
#
# FIND THE ANGLE THETA WHICH EXTREMIZES ROTATED VARIANCES
# THETA MEASURED CCW FROM EAST
#
  IF( U2==U2 )
    [ # THIS IS A SPECIAL CASE
      THETA=0.5*PIZ #PI/4
    ]
  ELSE
    [ # MORE GENERAL CASE
      THETA = 0.5*ATAN(2.*UU/(U2-U2))  # ANGLE BETWEEN + - PI/4
    ]
# COMPUTE ROTATED VARIANCES USING THIS THETA
  CS=COS(THETA)**2
  SN=SIN(THETA)**2
  TERM=2.*COS(THETA)*SIN(THETA)*UU
  AMAJOR=U2*CS+U2*SN+TERM
  AMINOR=U2*CS+U2*SN-TERM
# IF AMAJOR LT AMINOR THEN THIS THETA MINIMIZES ROTATED U VAR
# BUT WE WANTED TO MAXIMIZE IT, SO ADD PI/2 TO THETA TO GET
# CORRECT SENSE OF EXTREMA
  IF( AMAJOR.LT.AMINOR)
    [
      THETA=THETA+PIZ
      XX=AMAJOR
      AMAJOR=AMINOR
      AMINOR=XX  # SWAP MAJOR AND MINOR AXES
    ]
# MAKE SURE THETA BETWEEN + - PI/2
  IF( THETA.GT.PIZ) THETA=THETA-2.*PIZ
# CONVERT TO DEGREES CW FROM NORTH
  THETA=THETA*90./PIZ  # THETA IN DEGREES CCW FROM EAST
  ANG=90.-THETA
#
# POLARIZATION INDEX=1 FOR COMPLETELY POLARIZED,0 FOR ISOTROPIC
  POL=1.-AMINOR/AMAJOR
#
  RMS=SQRT(U2+U2)  # RMS VARIATION OF VECTOR MAGNITUDE
#
  RETURN
END

```

Table F-1 Subroutine PRINA

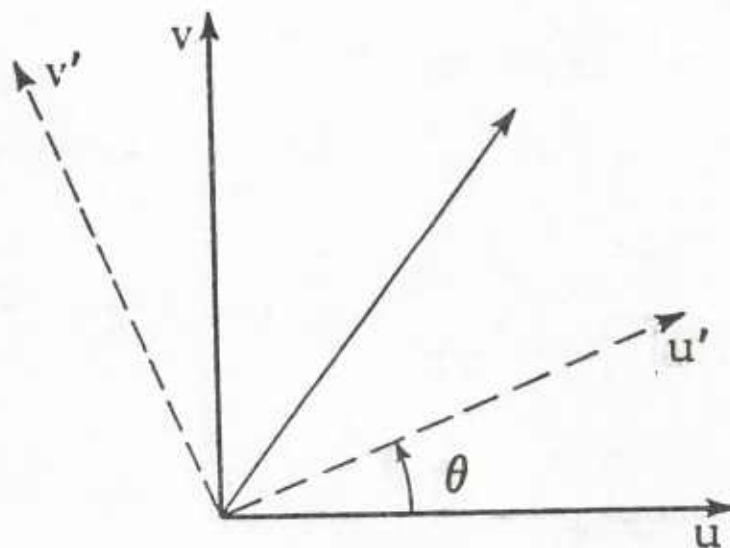


figure F-1 (u, v) are the old axes for the vector field. (u', v') are the new (principal) axes of the vector field which have a rotation of θ with respect to the old axes.

ONR/MPL GENERAL DISTRIBUTION LIST

Chief of Naval Research
Department of the Navy
Arlington, Virginia 22217
Code 12, 122(2), 102C
111, 112, 113,
1122PO, 425-AC, 460

ONRDET
NSTL Station
Bay St. Louis, Mississippi 39529
Code 112, 1121, 1122CS, 422CB,
1122PO, 1125GG

Director
Office of Naval Research
Branch Office
1030 East Green Street
Pasadena, California 91101

Commander
Naval Sea Systems Command
Washington, D. C. 20362
Code 63, 63R, 63R-23

Defense Advanced Res. Proj. Agency
TTO - Tactical Technology Office
1400 Wilson Boulevard
Arlington, Virginia 22209
Atten: CDR Kirk Evans

Commander
Naval Air Systems Command
Washington, D. C. 20361
Code 370

Commander
Naval Ship Res. & Dev. Center
Bethesda, Maryland 20084

Director
Strategic Systems Proj. Ofc. (PM-1)
Department of the Navy
Washington, D. C. 20361
Code NSP-2023

Commander
Naval Surface Combat Systems Center
White Oak
Silver Spring, Maryland 20910

Commanding Officer
Civil Engineering Laboratory
Naval Construction Battalion Center
Port Hueneme, California 93043
Code L40, L42

Director of Research
U.S. Naval Research Laboratory
Washington, D. C. 20375
Code 2620, 2627, 5000, 5100, 5800

Commanding Officer
Naval Ocean Research and
Development Activity (NORDA)
NSTL Station
Bay St. Louis, Mississippi 39529
Code 100, 110, 300, 330,
340, 350, 360, 500

Commander
U.S. Naval Oceanographic Office
NSTL Station
Bay St. Louis, Mississippi 39522
Bill Jobst

Commander
Submarine Development Group ONE
Fleet Post Office
San Diego, California 92152

Commander
Naval Warfare Systems Command
Washington, D. C. 20360
Code PME-124, 320A

Commanding Officer
U.S. Naval Air Development Center
Attention: Jim Howard
Warminster, Pennsylvania 18974

Executive Secretary, Naval Studies
Board
National Academy of Sciences
2101 Constitution Avenue, N.W.
Washington, D.C. 20418

Commander
Naval Ocean Systems Center
San Diego, California 92152
Code 00, 01, 16, 94, 531
5301, 71, 72

Commanding Officer
Naval Underwater Systems Center
Newport, Rhode Island 02844
John D'Albora

Officer in Charge
Naval Underwater Systems Center
New London Laboratory
New London, Connecticut 06320
Code 900, 905, 910, 930, 960

Assistant Secretary of the Navy
(Research Engineering & Systems)
Department of the Navy
Washington, D. C. 20350

Commanding Officer
Naval Coastal Systems Laboratory
Panama City, Florida 32401

Director
Defense Documentation Center
(TIMA), Cameron Station
5010 Duke Street
Alexandria, Virginia 22314

Institute for Defense Analyses
400 Army-Navy Drive
Arlington, Virginia 22202

Chief Scientist
Navy Underwater Sound Reference Div.
U.S. Naval Research Laboratory
P.O. Box 8337
Orlando, Florida 32806

Supreme Allied Commander
U.S. Atlantic Fleet
ASW Research Center, APO
New York, New York 09019
Via: ONR 100 M, CNO OP092D1,
Secretariat of Military,
Information Control, Committee

Director
College of Engineering
Department of Ocean Engineering
Florida Atlantic University
Boca Raton, Florida 33431

Director
Applied Research Laboratory
Pennsylvania State University
P.O. Box 30
State College, Pennsylvania 16802

Director
Lamont-Doherty Geological Observatory
Torrey Cliff
Palisades, New York 10964

Director
The Univ. of Texas at Austin
Applied Research Laboratory
P.O. Box 8029
Austin, Texas 78712

Director
Woods Hole Oceanographic Institution
Woods Hole, Massachusetts 02543

National Science Foundation
Washington, D. C. 20550

STOIA
Battelle Columbus Laboratories
505 King Avenue
Columbus, Ohio 43201

National Oceanic & Atmospheric
Administration
Ocean Engineering Office
6001 Executive Boulevard
Rockville, Maryland 20852

Superintendent
U.S. Naval Postgraduate School
Monterey, California 93940

Director
Institute of Marine Science
University of Alaska
Fairbanks, Alaska 99701

Director
Applied Physics Laboratory
Johns Hopkins University
Johns Hopkins Road
Laurel, Maryland 20810
Atten: J. R. Austin

Director
Marine Research Laboratories
c/o Marine Studies Center
University of Wisconsin
Madison, Wisconsin 53706

Director
Applied Physics Laboratory
University of Washington
1013 East 40th Street
Seattle, Washington 98105

Director
Inst. of Ocean Science Engineering
Catholic University of America
Washington, D.C. 20017

Office of Naval Research
Resident Representative
c/o Univ. of California, San Diego
La Jolla, California 92093

University of California, San Diego
Marine Physical Laboratory Branch Office
La Jolla, California 92093

December 1985

U223763